Targeting aminoacyl-tRNA synthetases for the development of novel therapeutics against leishmaniasis

Thesis submitted to the University of Hyderabad for the degree of Doctor of Philosophy (Ph.D.)

by

Fouzia Nasim
(16LTPM02)

Supervisor:
Dr. Insaf Ahmed Qureshi

Department of Biotechnology & Bioinformatics
School of Life Sciences
University of Hyderabad
Hyderabad-500 046, India

University of Hyderabad
Hyderabad-500 046, India

CERTIFICATE

This is to certify that this thesis entitled "*Targeting aminoacyl-tRNA synthetases for the development of novel therapeutics against leishmaniasis*" is submitted by Fouzia Nasim bearing registration number 16LTPM02 in partial fulfillment of the requirements for award of Doctor of Philosophy in the Department of Biotechnology & Bioinformatics, School of Life Sciences, is a bonafide work carried out by her under my supervision and guidance.

The thesis is free from plagiarism and has not been submitted previously in part or in full to this or any other University or Institution for award of any degree or diploma.

Parts of her work have been:

A. Published in the following research/review articles:

1) **Nasim F**, Kumar MS, Alvala M, Qureshi IA. Unraveling the peculiarities and development of novel inhibitors of leishmanial arginyl-tRNA synthetase. FEBS J. 2024 Mar 25.
2) **Nasim F**, Qureshi IA. Aminoacyl tRNA synthetases: implications of structural biology in drug development against trypanosomatid parasites. ACS Omega. 2023 Apr 10; 8(17):14884-14899.

B. Posters presented in the following conferences:

1) The 6th International Conference on Molecular Diagnostics and Biomarker Discovery, 11th-13th October, 2022, Universiti Sains Malaysia, Malaysia (WEBEX Event).
2) International Conference on Frontier Areas of Science and Technology, 12th India-Japan Science and Technology Conclave, 9th-10th September, 2022, School of Life Sciences, University of Hyderabad, India.
3) Sudhee-2022, 23rd-24th March, Chaitanya Bharathi Institute of Technology, Hyderabad, India. (Best Oral Presentation)

Further, the student has passed the following courses towards the fulfillment of coursework requirement for Ph.D.

Course code	Name	Credits	Pass/Fail
BT801	Research methodology/Analytical techniques	4	Pass
BT802	Research ethics, biosafety, data analysis, & biostatistics	4	Pass
BT803	Research proposal and scientific writing	4	Pass

Supervisor
Dr. INSAF A. QURESHI
Associate Professor
Dept. of Biotechnology & Bioinformatics
School of Life Sciences
University of Hyderabad
Hyderabad-500 046, India.

Head of Department 29/6/24
HEAD
Dept. of Biotechnology & Bioinformatics
University of Hyderabad
Hyderabad.

Dean of School 28/6/24
संकाय अध्यक्ष / Dean
जीव विज्ञान संकाय / School of Life Sciences
हैदराबाद विश्वविद्यालय / University of Hyderabad
हैदराबाद / Hyderabad-500 046.

University of Hyderabad
Hyderabad-500 046, India

DECLARATION

I, Fouzia Nasim, hereby declare that this thesis entitled "*Targeting aminoacyl-tRNA synthetases for the development of novel therapeutics against leishmaniasis*" submitted by me under the guidance and supervision of Dr. Insaf Ahmed Qureshi, is an original and independent research work. I also declare that it has not been submitted previously in part or in full to this University or any other University or Institution for the award of any degree or diploma.

Date: 27 June, 2024

Fauzia Nasim
Signature of the student
Name: FOUZIA NASIM
Regd. No. 16LTPM02

Signature of the Supervisor
Dr. INSAF A. QURESHI
Associate Professor
Dept. of Biotechnology & Bioinformatics
School of Life Sciences
University of Hyderabad
Hyderabad-500 046, India.

ACKNOWLEDGEMENTS

As the author of this thesis, I would like to inscribe my sincere emotions for those people without whom I would have probably struggled to accomplish my degree.

The success of this Ph.D. goes to my research advisor, **Dr. Insaf Ahmed Qureshi** whom I thank for the kind of belief he has in me, be it regarding my scientific approach towards a problem statement or the way of my working, he has always supported me in every possible way he could. It was he who motivated me to keep aside my struggles and rather work hard to achieve my goals because that is the only way by which I could prove to the world what I am capable of.

I render my immense gratitude towards my doctoral committee members, **Prof. Nooruddin Khan, Dr. N. Prakash Prabhu**, and **Dr. Manjari Kiran** who have always encouraged and supported me during my Ph.D. tenure.

I am thankful to **HEADs** and **DEANs** of Department of **Biotechnology & Bioinformatics** and **School of Life Science** for providing all the necessary facilities.

I am immensely grateful to **Dr. Rahila Qureshi** for guiding me through cell culture handling and MTT assay. She has always provided me with useful suggestions and corrections in my every manuscript.

I am thankful to my collaborators, **Dr. Mallika Alvala** and **Muppidi Sravankumar**, from NIPER, Hyderabad for synthesizing the inhibitors described in this thesis.

I also thank my lab members **B. Narsimulu, J. Pranay, Janish, Jyotisha,** and all other **M.Sc., M. tech.** students for providing all sorts of professional cooperation.

My beloved friends from SLS, **Sonika, Iman, Aishwarya, Neha,** and **Ghufrana** have always provided the necessary moral support that helped me overcome any troublesome situation**.**

I thank **UGC: MANF** and **ICMR** for providing financial assistance.

My heartfelt thanks to my **family** from both sides **(best of both worlds)** for their love and to my husband, **Quadir** for his full-fledged support.

Fouzia Nasim

Dedicated to my family

CONTENTS

Abbreviations

WHO	World Health Organization
NTD	Neglected tropical disease
CL	Cutaneous leishmaniasis
DCL	Diffused cutaneous leishmaniasis
PKDL	Post-kala azar dermal leishmaniasis
TyR	Trypanothione reductase
AaRS	Aminoacyl-tRNA synthetase
CCD	Catalytic core domain
ArgRS	Arginyl-tRNA synthetase
HisRS	Histidyl-tRNA synthetase
LB	Luria-Bertini
EMSA	Electrophoretic mobility shift assay
PCR	Polymerase chain reaction
SOE-PCR	Splicing by overlapping extension-PCR
IPTG	Isopropyl β-d-1-thiogalactopyranoside
DTT	Dithiothreitol
PMSF	Phenylmethylsulfonyl fluoride
L-Arg	L-arginine
L-Can	L-canavanine
L-His	L-histidine
MTT	3-(4,5- dimethyl-2-thiazolyl)-2,5-diphenyltetrazolium bromide
RMSD	Root mean square deviation
Rg	Radius of gyration
RMSF	Root mean square fluctuation
MM/PBSA	Molecular mechanics poisson-Boltzmann surface area
FEL	Free energy landscape

List of figures:

List of tables:

1. Introduction and review of literature

Leishmaniases are a wide variety of diseases caused by protozoan parasites belonging to the genus *Leishmania*. Approximately 700,000 to 1 million new cases are reported annually which are transmitted by the bite of female phlebotomine sand flies (https://www.who.int/news-room/fact-sheets/detail/leishmaniasis). Even though it infects millions every year, cost-effective treatments are unavailable. Hence, it is necessary to include newer targets in developing antileishmanials to counter the limitations posed by these drugs.

1.1. Leishmaniases

The World Health Organization (WHO) enlists 20 diverse bacterial, parasitic, fungal, viral, and non-communicable conditions as neglected tropical diseases (NTDs) (https://www.who.int/teams/control-of-neglected-tropical-diseases/global-report-on-neglected-tropical-diseases-2023). Of them, the infections caused by trypanosomatids are of a serious concern as they are endemic to countries with poor socio-economic backgrounds and limited access to healthcare facilities. Moreover, overlapping of some of these endemic regions results in their co-infection thus further adding to the woes. The global spread of leishmaniases and trypanosomal infections has been depicted in Figure 1. Leishmaniases are caused by parasites belonging to the genus *Leishmania* of the order Trypanosomatida. Infections that are caused by the leishmanial parasites are usually associated with bad housing, migration, and weak immunity. The female sandflies of the genus *Lutzomyia* and *Phlebotomus* of subfamily Phlebotominae are primary hosts of *Leishmania* sp. The infective stage (promastigotes) of *Leishmania* sp. is injected into the secondary hosts by sandflies which are phagocytosed by macrophages and other mononuclear phagocytic cells. Later on, these promastigotes transform into amastigotes and spread infection to other mononuclear cells. As per records, about 20 species of *Leishmania* are pathogenic for humans and the severity of this disease can be rated on a scale of high to low depending on the species transmitted by sand flies. On the basis of clinical manifestations, leishmaniases can be categorized into three broad groups. The cutaneous form of leishmaniasis (CL) chiefly develops a chronic skin ulcer at the site of the sand fly bite, which often takes months to heal. The mucocutaneous leishmaniasis initially causes skin ulcers similar to that of cutaneous form that heal. However, the lesions reappear subsequently in mucous tissue of the nose and mouth leading to massive tissue damage. Lastly, visceral leishmaniasisis a rather serious condition that leads to swelling of visceral organs such as the spleen, liver, lymph nodes, bone marrow, etc.,

which if neglected is highly fatal. Of late, new forms of leishmaniases such as diffused cutaneous leishmaniasis (DCL) and post kala-azar dermal leishmaniasis (PKDL) have evolved from cutaneous and visceral leishmaniasis, respectively [1, 2]. The disease is mostly reported from Asia, Africa, and Latin America where about 98 countries are endemic for leishmaniases.

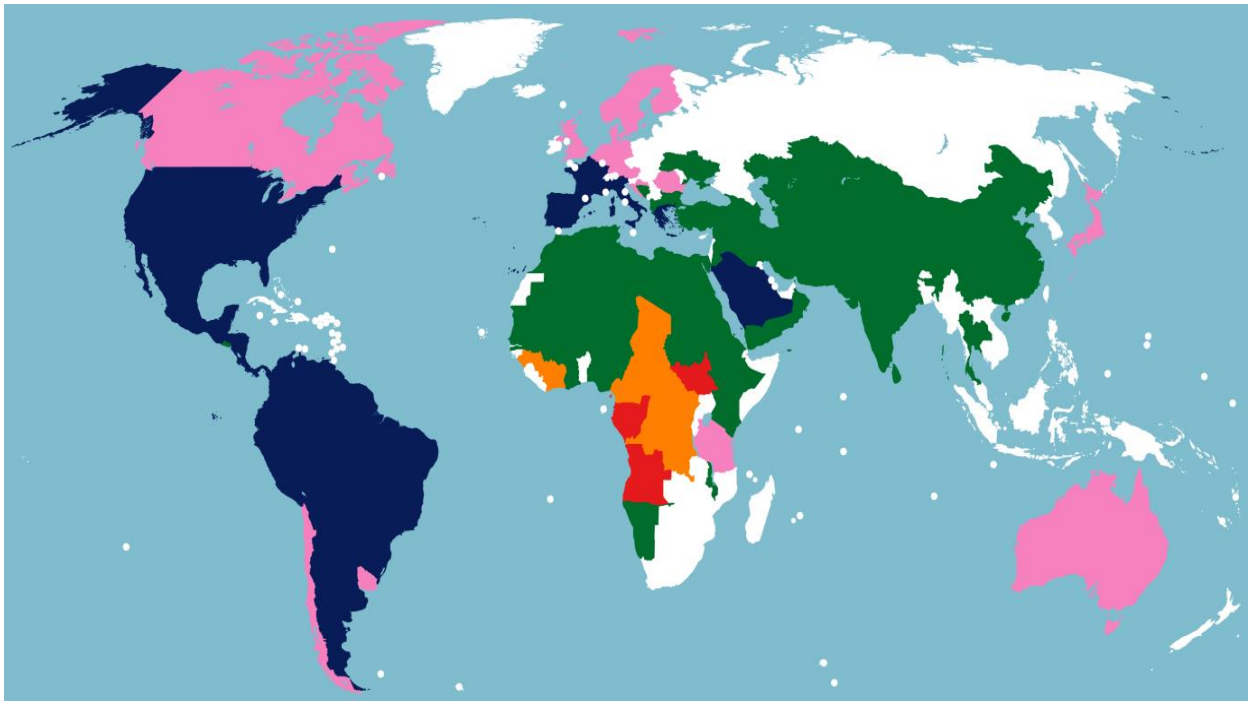

Figure 1: Global distribution of infections caused by trypanosomatids. Regions recognized for a particular trypanosomatid-related infection have been demarcated based on the technical health data published by WHO in the year 2018 for American trypanosomiasis and 2021 for leishmaniases and human African trypanosomiasis. The green, red and pink colours represent the localisation of leishmaniases, human African trypanosomiasis and American trypanosomiasis, respectively. The orange colour denotes regions where both leishmaniases and human African trypanosomiasis are prevalent, while the blue colour delineates regions where both leishmaniases and American trypanosomiasis are found. The global map was generated using MapChart online server (https://www.mapchart.net/).

1.2. Available therapeutics for leishmaniases

Despite affecting as many as half a million people worldwide annually, remarkable progress in development of drugs against leishmaniases that are cost-effective and at the same time render a complete cure is not very evident. The remedies which are currently employed for the treatment of these diseases such as arsenals and antimonials have low efficacy, high toxicity, and become

ineffective due to drug resistance among parasites. Furthermore, in some cases, the recurrence of infections has also been observed. The disadvantages of some of the current remedies have been listed in Table 1. However, these diseases are curable if a timely diagnosis complexed with a proper as well as cost-effective regimen is established. In order to combat the rapid spread of infections caused by trypanosomatids, several attempts have been made to immunize the hosts via inducing a passive immunity by injecting dead or weakened parasite. For instance, leishmanization is the inoculation of a mixture of live and dead *Leishmania major* to generate a mild cutaneous leishmaniasis that can avert future infection by the parasite. Some of the licensed vaccines such as Leishmune, CaniLeish, Leishtech, Letifend, etc. are available in a few countries to prevent canine visceral leishmaniasis.

Table 1: Available drugs against leishmaniases and their side effects

Drug	Mode of action	Disadvantage	Reference
Pentavalent antimony compounds	Pentavalent antimony Sb(V) under low pH gets converted to trivalent antimony that is reported to kill parasites through inhibition of trypanothione reductase (TryR)	Parasite resistance is being reported from many disease endemic countries, and in Indian subcontinent these compounds are not being used to treat patients	3
Paromomycin	Inhibition of protein synthesis and alteration in mitochondrial membrane potential	Poor absorption and required to be given through intramuscular injections	3
Amphotericin B	AmpB primarily targets ergosterol present in parasites cell membrane and affects cellular integrity resulting in disorganization of the membrane and formation of aqueous pores	Highly toxic and causes numerous side effects such as high fever, rigor, chills, and renal failure	3
Miltefosine	Miltefosine induces apoptosis like events in *Leishmania* species and depolarizes	Resistance of parasites is mainly due to over expression of an ABC	4

	mitochondrial membrane potential. It inhibits cytochrome-c oxidase, which might be associated with the apoptosis-related death of parasites.	transporter, P-glycoprotein, accomplished by inactivation of two proteins responsible for its uptake, the *Ld*MT and its beta subunit *Ld*Ros3	

1.3. Protein synthesizing machinery as a drug target

The "Central Dogma" of molecular biology elucidates the process by which the genetic code is carefully decoded and converted into a functional product in a living system. Two important phenomena are fundamental to Central Dogma *viz.* transcription of mRNA from DNA and mRNA translation into protein. Several macromolecules such as tRNA, aminoacyl-tRNA synthetases (aaRSs), ribosomes, auxiliary factors etc., integrate to form the protein synthesizing machinery, all of which are tightly regulated. Since regulation of gene expression at the translational level is associated with cell adhesion and migration, axes development in embryo etc., dysregulation of any of these constituents can lead to aberrant functioning or even termination of some of the most important metabolic processes happening inside a cell. A rapidly growing cell demands abundant as well as synchronized pattern of protein synthesis and protozoan parasites proliferating continuously inside their host are no exception to it. A global map describing the cross-talk between proteins and their complexes happening inside *Trypanosoma brucei* has also been documented [5]. Antibiotics such as chloramphenicol, tetracycline, erythromycin, kanamycin, etc., are all known to inhibit bacterial growth by terminating the elongation of nascent polypeptides. It has also been reported that inhibitors targeting the translation process can be used to study gene expression by ribosome profiling apart from being used in cell culture techniques [6]. Many of these inhibitors such as anisomycin, trichothecene mycotoxins, narciclasine, A201A etc., affect polypeptide elongation by binding to the A-site of ribosome thereby destabilizing aminoacyl-tRNA binding. Some of them like bactobolin A and blasticidin S bind to the P-site and promote inhibition by a similar mechanism. Another inhibitor puromycin mimics the CCA-end of tRNA and on entering the ribosome causes untimely termination of polypeptide synthesis. Likewise, with the enumeration of multifaceted roles of aaRSs, these enzymes are being considered as new drug targets on the table. Possessing at least three important sites for their proper functioning *viz.* a tRNA binding site, ATP binding domain and a site to incorporate the correct amino acid, aaRSs

have been considered as potent target for drug development [7-10]. *Leishmania* sp. has been shown to shut off translation mechanisms happening inside the macrophages of their host by using a GPI-anchored surface metalloproteinase, gp63, or leishmanolysin that cleaves mTOR (rapamycin) leading to dephosphorylation of 4E-BP1 [11]. It has been reported that not all targets/pathways perform well in the drug trial sessions, some of them being cytochromeP450 family 51 (CYP51), cytochrome b, etc. One of the key reasons is the presence of limited targets within a pathway that further scale down the scope for combinatorial therapy. On the other hand, the protein translational machinery is a broad umbrella harbouring several suitable drug targets that are crucial for the parasite's survival.

1.4. Aminoacyl tRNA synthetases

Fidelity is a prerequisite for deciphering the genetic code and this high degree of fidelity is rendered by aaRSs that are responsible for the ligation of amino acids to their cognate tRNAs. The precision in the mode of action is dependent upon several factors such as stereospecificity of aaRSs towards their respective amino acids and tRNA [12] and the presence of editing domains that remove erroneous amino acids, if incorporated [13, 14]. The formation of aminoacyl-tRNA is a two-step enzymatic mechanism [15] (Figure 2). Although the ultimate goal of aaRSs is to catalyze a reaction that leads to attachment of an amino acid with its cognate tRNA, based on the architectural differences of their catalytic sites, the known 23 aaRS can be classified into two groups. Class I enzymes possess Rossmann fold motif with HIGH (His-Ile-Gly-His) and KMSKS (Lys-Met-Ser-Lys-Ser) conserved sequences just like dehydrogenases and some kinases that have an expanded five stranded parallel β-strands connected by alpha [16]. Whereas a rare structural fold is observed in the case of class II enzymes that consists of six antiparallel β-strands and is elsewhere reported in biotin synthetase holoenzyme [17]. Transfer of aminoacyl adenylate happens on either the 2' or 3' hydroxyl group of terminal adenosine residue present in 3' terminal of tRNA molecule. The class I aaRSs prefer 2' hydroxyl group, while the class II aaRSs transfer the aminoacyl adenylate on the 3' hydroxyl group of tRNA molecule. Further classification of aaRSs can be made on the basis of site at which reaction is taking place i.e., cytosolic or mitochondrial.

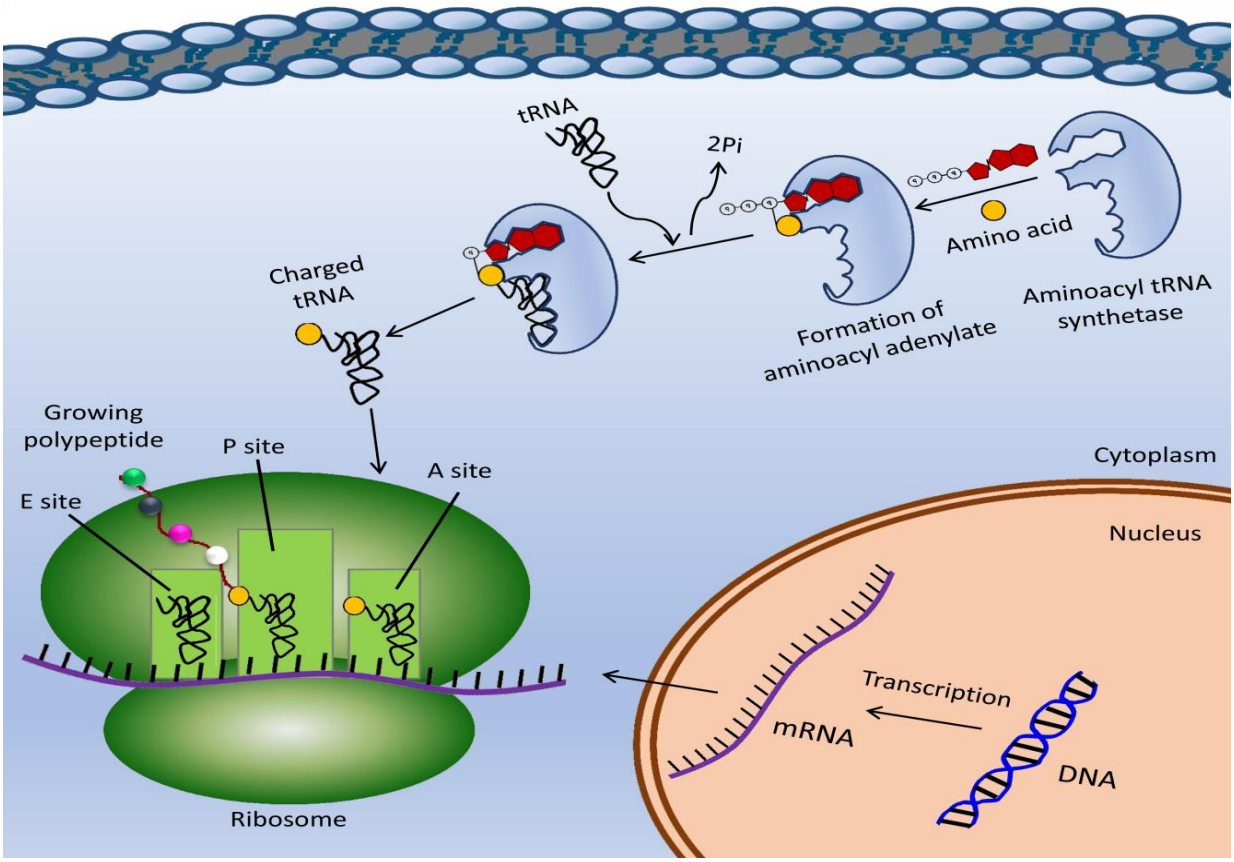

Figure 2: Schematic representation of a cell showing the process of aminoacylation. In the initial steps of aminoacylation, the tRNA synthetase is bound by ATP and its cognate amino acid that results in the formation of aminoacyl adenylate intermediate upon release of a pyrophosphate molecule. In the sequential steps, the cognate tRNA binds to this tRNA synthetase via its anticodon domain and the amino acid is transferred to its CCA arm resulting in the formation of adenylated tRNA (charged tRNA). On the release of charged tRNA as well as AMP, the tRNA synthetase is now ready for another cycle of aminoacylation.

The general nomenclature of aaRSs begins with the uppercase alphabet representing the amino acid followed by 'RS'. Also, a numerical '2' is appended to the mitochondrial version of the synthetase, for example in the case of aspartyl tRNA synthetase, the cytosolic form is abbreviated as DRS1 and the mitochondrial form as DRS2. It is noteworthy that unlike other eukaryotes that possess at least two genes for most of the cytosolic and mitochondrial aaRSs, the trypanosomatids encode only one gene except for a few, such as AspRS, TrpRS, and LysRS [18, 19]. In trypanosomatids, 26 aaRSs have been recognized [20]. In reference to *Trypanosoma*, a study revealed that alternate trans-splicing of an immature RNA results in formation of isoforms, the one with mitochondria targeting sequence (MTS) is directed towards mitochondria while the one

devoid of MTS is retained within cytosol [21]. Novel antibiotics having aaRSs as their target have drawn a great deal of interest, some of which are REP8839 and AN2690 that have successfully stepped forward for clinical trials. In fact, mupirocin marketed as Bactroban by GSK is a well-known drug approved by the FDA. It is isolated from *Pseudomonas fluorescens* and targets the active site of isoleucine tRNA synthetase of *E. coli* [22]. Consecutively, methods that enable high throughput screening of inhibitor libraries have been developed exclusively for trypanosomatid based drug targets. Although, the resazurin assay has been used to measure the cytotoxicity of inhibitors towards parasites, there exists several limitations such as false negatives, long incubation period etc. which hindered the process of drug discovery [23]. Moreover, a SYBR Green based semi-automated assay has been developed that could possibly replace the resazurin test to check the cytotoxicity posed by the potent inhibitors to parasites. This test might be used by the researchers in the times to come and is cost-effective with minimal background noise [24]. Lately, the quest for the development of novel anti-trypanosomal drugs has brought researchers closer towards targeting aaRSs based on which inhibitors were designed that subsequently showed a post-treatment decrease in parasite growth (Figure 3).

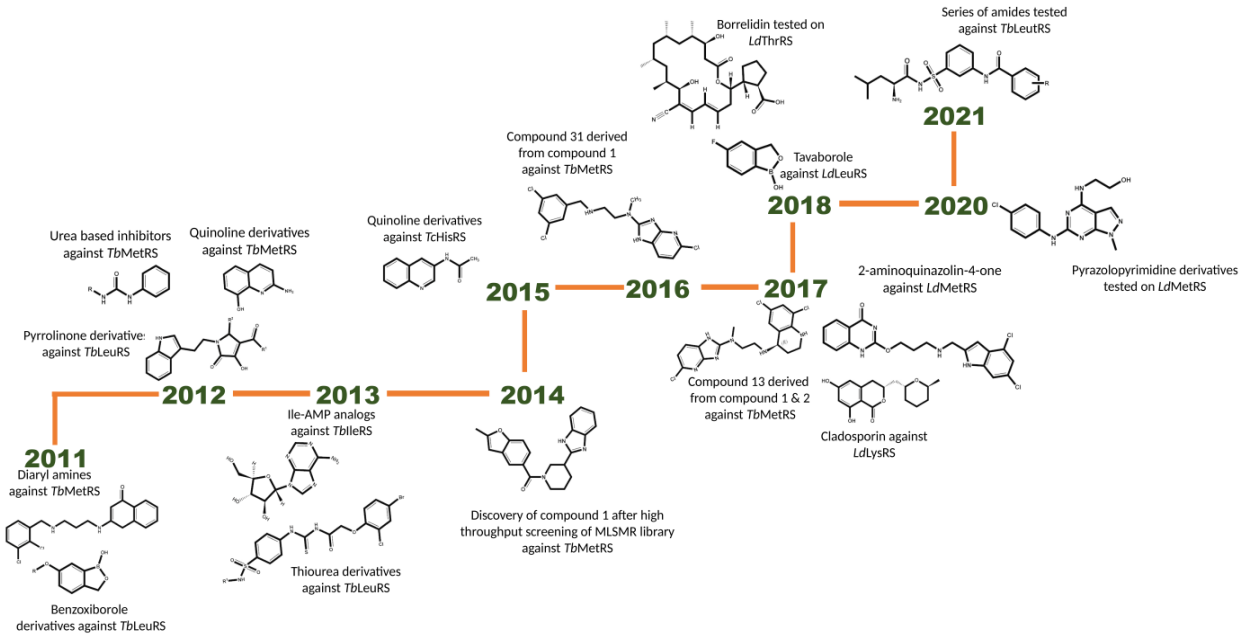

Figure 3: Evolution of drugs against trypanosomatid aaRSs in recent years. Target-specific inhibitor designing in order to attain enriched potency in the case of trypanosomatid aaRSs has been mostly done for LeuRS, MetRS and HisRS. Also, drugs like borrelidin and cladosporin which are well-known inhibitors of ThrRS and LysRS have shown promising results in the reduction of parasitic growth.

1.5. Leishmanial aaRSs

Several studies have reported the essentiality of aaRSs as suitable drug targets for curbing leishmaniases. For example, the replacement of LeuRS gene resulted in reduction of parasitemia in mouse macrophages infected with *L. donovani* and the compound 5-fluoro-1,3- dihydro-1-hydroxy-benziborole (AN2690) could inhibit *L. donovani* growth both in amastigote and promastigote stages *in vitro* as well as *in vivo* (BALB/c mice) while rendering low toxicity to mammalian cells [25]. Post AN2690 treatment, the aminoacylation activity was reduced by 2.8-fold, suggesting that AN2690 inhibits parasite growth by targeting LeuRS [25]. A recent study also demonstrated that CP1 domain of *Ld*LeuRS plays a pivotal role in aminoacylation activities and with the help of isothermal titration calorimetry, the high binding affinity of AN2690 for CP1 domain could be noticed [26]. It has been reported that *L. major* lack a C-terminal dimerization region in MetRS [27] and substantial differences were observed near the ATP and substrate binding regions of *Lm*MetRS to that of human mitochondrial and cytosolic forms which results in selective inhibition of parasite MetRS [27]. Researchers also identified DDD806905 (MetRS01) based on a high-throughput compatible biochemical assay that was shown to compete for methionine and high levels of potency was demonstrated in various *Leishmania* cell-based viability assays and *in vitro* translational assays [28]. However, this inhibitor failed to prove its efficacy in the *in vivo* studies pertaining to its dibasic nature. *L. donovani* tyrosyl tRNA synthetase (*Ld*TyrRS), like other TyrRSs was found to be a dimer and involved in chemokine signaling [29]. It was observed that *Ld*TyrRS on migrating to the extracellular environment acts as a neutrophil chemoattractant wherein the binding of the ELR peptide motif with the CXCR2 receptor of host macrophages mediate secretion of proinflammatory cytokines such as TNF-α and IL-6 in *Leishmania* infections, thus highlighting its immune-modulating roles. The study further documented slower growth kinetics and virulence for heterozygous mutants of *L. donovani*. Moreover, TyrRS appeared to be an essential enzyme for the parasite as the chromosomal null mutant did not survive [29]. Structural analysis of *Ld*TyrRS in complex with tyrosyl adenylate analog (TyrSA) have shown the two pseudo-monomers, each with two domains, and the presence of an extra pocket (EP) near to the adenine binding pocket which is absent in *Hs*TyrRS [30]. Some of the previously proclaimed antiparasitic plant derivatives such as polyphenolic compounds and alkaloids have been shown to specifically target the active pocket of leishmanial TyrRS with the

help of molecular docking analysis [31, 32]. A study also validated the importance of tRNA-aaRS interactions for the development of antitrypanosomal drugs via computational approaches whrein the screening of marine natural products (MNP) library led to identification of extracts possessing tremendous inhibitory potential toward *L. major* ThrRS. Furthermore, of the several inhibitors screened, they were successful in identifying three major inhibitors of *Lm*AlaRS [33]. Similarly, the leishmanial AspRS has been characterized at various dimensions as well. On the basis of the gel-filtration chromatogram, the cytosolic *Ld*AspRS was found to be a homodimer [34]. For LysRS, there is an extreme conservation seen in the ATP binding pocket of *Leishmania* species and other eukaryotes except two residues (Q308 and S324) which forms the basis of selective inhibition by cladosporin and its isoform and could retard parasite growth [35].

1.6. Arginyl- and histidyl-tRNA synthetases

ArgRS is a class-Ic tRNA synthetase that undergoes ATP-PPi exchange with the help of its cognate tRNA [36], like GlnRS [37], and GluRS [38, 39]. In *Trypanosoma brucei*, it showed a good druggability score, and its knockdown led to rapid cell death [40]. In *Plasmodium falciparum*, chloroquine-mediated disruption of heme detoxification allowed the cytosolic hemin to dimerize ArgRS, thus rendering it inactive and causing cell death [41]. Additionally, the catalytic core domain (CCD) of leishmanial ArgRS was observed to be unique than other ArgRSs as a large insertion was found in it whose role is also unknown.

The histidyl-tRNA synthetase (HisRS) is grouped with other class IIa aaRSs (viz., ProRS, ThrRS, AlaRS, SerRS, and GlyRS) that possess similar anticodon binding domains [42, 43]. As observed in HisRSs of eukaryotes, the trypanosomatid HisRSs contain a lysine-rich N-terminal domain that has been earlier linked to the binding of tRNA [44]. Co-crystallized structures of HisRSs with L-His, ATP, and quinolone inhibitors have provided relevant insights into the interactions between HisRS and its cognate ligands [45-47]. Furthermore, using RNAi, HisRS has been reported to be indispensable for the propagation of *T. brucei* [45]. The differences between human and trypanosomatid HisRS pave the way for genesis of drugs with high specificity and less cytotoxicity [44, 45]. Despite their significance as good drug targets in other organisms, ArgRS and HisRS have not been characterized enzymatically and structurally from leishmanial parasites.

1.7. Objectives:

- To clone and purify arginyl- and histidyl-tRNA synthetases of *Leishmania donovani*
- To characterize the purified proteins biochemically and perform inhibition studies
- To assess the structure of leishmanial proteins with or without ligands

2. Materials & Methods

2.1. Materials

2.1.1. Plasmids, bacterial strains, and kits

The pET28a(+) expression vector used for cloning was procured from Novagen, USA. *Pfu*, *Taq* polymerases, and dNTPs were purchased from G-Biosciences, USA, while the endonucleases (*Nde*I, *Eco*RI, *Dpn*I), Phusion polymerase, T4 DNA ligase, GeneJET Gel Extraction, Plasmid MiniPrep, and Electrophoretic Mobility-Shift Assay (EMSA) kits were bought from Thermo Fisher Scientific, USA. *E. coli* strains such as XL1-Blue and BL21 (DE3) were procured from Stratagene, USA, and Novagen, USA, respectively. The primers used for amplification were acquired from GCC Biotech Pvt. Ltd., India.

2.1.2. Culture media and cell lines

Luria Bertani (LB) media used for growing *E. coli* cells was prepared by dissolving 10 g Tryptone, 10 g NaCl, and 5 g yeast extract in 900 ml of distilled water and the volume was adjusted to 1000 ml. For induction of recombinant proteins, 1 M IPTG was prepared by mixing 238 mg in sterile Mili-Q water. All of these chemicals were obtained from HiMedia Laboratories (India). Murine macrophages RAW 264.7 were the kind gift from Dr. Nooruddin Khan and were grown in DMEM media. The cell culture reagents were purchased from HiMedia Laboratories (India) and DMSO was bought from Sigma-Aldrich, USA.

2.1.3. Antibiotic stocks

Kanamycin (50 mg/ml) and tetracycline (12.5 mg/ml), purchased from HiMedia Laboratories (India), were prepared in sterile Mili-Q water and 70% ethanol, respectively, and stored at -20°C until required.

2.1.4. Beads and columns used for protein purification

To purify recombinant proteins by affinity chromatography, Ni-NTA agarose beads were procured from G-Biosciences, USA. For subsequent purification of the proteins by size-exclusion chromatography, HiLoad 16/600 Superdex 200 pg column was purchased from GE Healthcare, USA.

2.1.5. Components of aminoacylation assay

The constituents of aminoacylation assay such as HEPES buffer, DTT, divalent, and monovalent salts were purchased from HiMedia Laboratories (India). The components of developing solution like malachite green, ammonium molybdate, and polyvinyl alcohol were also obtained from HiMedia Laboratories (India). Cofactor, substrate, pseudosubstrate, and PPiase were procured from Sigma-Aldrich, USA.

2.2. Methods

2.2.1. Sequence analysis and phylogenetic tree

The CCDs of ArgRSs and protein sequences of HisRSs from organisms belonging to different strata of evolution (viz., archaea, bacteria, and eukaryotes) were retrieved from the KEGG database (https://www.genome.jp/kegg/) and used to construct the rooted phylogenetic trees. Protein sequences were aligned using MUSCLE [48], and the phylogenetic tree was constructed applying MEGA-X [49] with 1000 bootstrap steps by Neighbor-Joining method [50]. Furthermore, global sequence alignments of ArgRSs or HisRSs from *L. donovani*, *Trypanosoma* as well as *H. sapiens* were performed by Clustal Omega (https://www.ebi.ac.uk/Tools/msa/clustalo/) and submitted to ESPript 3.0 (https://espript.ibcp.fr/ESPript/cgi-bin/ESPript.cgi). The domain arrangements of *Ld*ArgRS and *Ld*HisRS was predicted by Pfam (http://pfam.xfam.org/) and their physicochemical parameters such as molecular weight and pI, were computed with the help of Expasy ProtParam tool (https://web.expasy.org/protparam/).

2.2.2. Cloning of ORFs in pET28a(+) vector

The full-length nucleotide sequences of *Ld*ArgRS and *Ld*HisRS were retrieved from the KEGG database with the corresponding accession numbers LDBPK_271230 and LDBPK_300650. The ORFs were amplified from the genomic DNA of *L. donovani* (Strain: MHOM/IN/80/*DD8*) by *Pfu* DNA polymerase with gene-specific primers containing *Nde*I and *Eco*RI restriction sites in the forward and reverse primers, respectively. A similar strategy was employed to amplify *Hs*ArgRS and *Hs*HisRS from human myeloid fibroblast cDNA (Table 2). Initially, a gradient PCR with varying annealing temperatures was performed to optimize T_m which was thereafter used for the next set of ORFs amplifications. A total of six PCR were designed to obtain ΔIns-*Ld*ArgRS through splicing by overlapping extension (SOE)-PCR employing the set of primers given in Table

2. The first two PCR amplified ORF portions preceding and succeeding the insertion segment, i.e., the first half and second half ORF of *Ld*ArgRS. The third and fourth PCR were meant for the incorporation of flanking ends into the previously obtained PCR products. The primers were made such that the trailing end of the first half and initial end of the second half of ORF are complementary to each other. No primers were used in the fifth PCR reaction as the flanking sequences incorporated in the previous two sets of reactions acted as primers and created a nascent ORF corresponding to 1.7 kb. The final PCR was set up with the original forward and reverse primers (also used for the amplification of full-length *Ld*ArgRS) to amplify the nascent ORF. All the above PCR products were loaded onto 1% agarose (w/v) gels, followed by their extraction and purification by GeneJET Gel Extraction kit. Utilizing *Nde*I and *Eco*RI, the amplicons as well as pET28a(+) vector were digested, ligated together with T4 DNA ligase for 2 hours at 22°C, and subsequently transformed into *E. coli* XL1 Blue cells. For site-directed mutagenesis of *Ld*HisRS, catalytic pocket residues viz., Glu157 and Arg164 to alanine was executed by employing primers with specific mutations (Table 2). The inverse PCR of the constructs was done with Phusion polymerase and subsequently treated with *Dpn*I for 1 hr at 37°C to cleave the methylated parental DNA. To confirm the clones, the plasmids were isolated with GeneJET Plasmid Miniprep Kit and proceeded for double digestion followed by DNA sequencing.

Table 2: Primers used for cloning and site-directed mutagenesis

		Primers used
*Ld*ArgRS		FP: 5'ATTCATATGTGCGCCGCTGCCGCTACC 3' RP: 5' ATCGAATTCCTAAATGCGCTCGGCCGTCTCGATGTT 3'
*Hs*ArgRS		FP: 5' ATACATATGGACGTACTGGTGTCTGAGTGC 3' RP: 5' GAATTCTTACATCCTTTGGACAGGTTTTATTCC 3'
ΔIns-*Ld*ArgRS	First PCR	FP: 5'ATTCATATGTGCGCCGCTGCCGCTACC 3' RP: 5' CTTGCTGACGATGAGCTTCGCGCCGT 3'
	Second PCR	FP: 5' CGTTTCTCCTTCCCGCTGATGGTGGTGAAAAGT 3' RP: 5' ATCGAATTCCTAAATGCGCTCGGCCGTCTCGATGTT 3'
	Third PCR	FP: 5'ATTCATATGTGCGCCGCTGCCGCTACC 3' RP: 5' GAAGCTCATCGTCAGCAAG 3'
	Fourth PCR	FP: 5' TCGTCAGCAAGCGTTTCTCCTCCCGCT 3' RP: 5' ATCGAATTCCTAAATGCGCTCGGCCGTCTCGATGTT 3'
	Fifth PCR	No primers used
	Sixth PCR	FP: 5' ATTCATATGTGCGCCGCTGCCGCTACC 3' RP: 5' ATCGAATTCCTAAATGCGCTCGGCCGTCTCGATGTT 3'
*Ld*HisRS		FP: 5' AAATGTCATATGTCCTCGACGGCCTCGCCCAAT 3' RP: 5' ATCGAATTCCTACAAGTCTTCGAAGGGCACAGGGTC 3'
*Ld*HisRS-E157A		FP: 5' CGGGAGATGGCCGCGTAGCGCCAGC 3' RP: 5' GCTGGCGCTACGCGGCCATCTCCCG 3'
*Ld*HisRS-R164A		FP: 5' GTAATGCTCACGGGCACGACCGCGGGAGATG 3' RP: 5' CATCTCCCGCGGTCGTGCCCGTGAGCATTA 3'
*Hs*HisRS		FP: 5' ATACATATGGCAGAGCGTGCGGCGCTG 3' RP: 5' ATAGTCGACTCAGCAGATGCAGAGGGGCTG 3'

2.2.3. Expression and purification of recombinant proteins

Upon confirmation of clones, the constructs were transformed into *E. coli* BL21 (DE3) cells for expression of the recombinant proteins. Cells were grown at 37°C for 16 hrs in LB (Luria Bertani) media containing 50 µg/ml kanamycin as primary culture, followed by their inoculation at a 1:100

ratio as secondary culture until OD_{600} reached 0.4–0.6 before proceeding for protein induction at 0.5 mM IPTG (Isopropyl β-d-1-thiogalactopyranoside). The induced cells were pelleted at 3438 g for 10 minutes at 4°C. Cells were resuspended in a lysis buffer comprising 20 mM (*Ld*ArgRS) or 50 mM (*Ld*HisRS) phosphate buffer pH 8, 400 mM NaCl, 30 mM imidazole, 2.5% glycerol, 1 mM DTT (Dithiothreitol), 1 mM PMSF (Phenylmethylsulfonyl fluoride), 0.5% Triton X-100, and 0.25 mg/ml lysozyme, and then subjected to sonication at a 10/20 sec ON/OFF cycle with 35% amplitude. Following the pelleting of cell debris at 13,751 g for 30 minutes at 4°C. For purification of *Ld*ArgRS, the supernatant was kept for binding with pre-equilibrated Ni-NTA agarose beads and then washed rigorously with buffers containing 30, 40, and, 50 mM imidazole. The proteins were eluted at gradient imidazole concentrations (100, 250, and 400 mM), and the highest form of purity was observed from 250 mM imidazole onwards. Similarly, for *Ld*HisRS, the cell lysate was then allowed to bind with the pre-calibrated Ni-NTA agarose beads for about 1 hour at 4°C. Two washes of 25 mM and 30 mM imidazole were given before eluting the pure proteins starting from 100 mM to 500 mM imidazole. The purified fractions of recombinant proteins were clubbed together, concentrated to 5–10 mg/ml, and proceeded for size-exclusion chromatography (HiLoad 16/600 Superdex 200 pg column, GE Healthcare, USA) with a buffer consisting of 30 mM HEPES pH 7 and 150 mM NaCl. Molecular weights of the purified proteins were deduced by comparing their elution volume with that of standard proteins used for calibration of the column. The concentration of purified proteins was estimated through Nanodrop 2000c (Thermo Fisher Scientific, USA) with the help of molecular weight as well as molar extinction coefficient viz., *Ld*ArgRS (62, 800 M^{-1} cm^{-1}; 80 kDa) and *Ld*HisRS (39, 880 M^{-1} cm^{-1}; 55 kDa).

2.2.4. Aminoacylation assays

The aminoacylation reaction was performed similarly to that of *Ld*SerRS [51] with some modified parameters. For aminoacylation of ArgRS, the reaction consisted of 5 mM L-arginine (L-Arg, substrate) or L-canavanine (L-Can, pseudo-substrate), 100 µM ATP, 0.25-2 µM purified protein, 1 mM DTT, 10 mM $MgCl_2$, 4 µg/µl with or without ytRNA (Sigma-Aldrich, USA), and 2 U/ml inorganic pyrophosphatase (Sigma-Aldrich, USA) dissolved in an aminoacylation buffer containing 30 mM HEPES pH 7 and 150 mM NaCl. While the final concentration of divalent metals was kept at 10 mM, the monovalent metals were used at 15 mM. For the determination of kinetic parameters, the concentrations of substrate/pseudo-substrate, ATP, and tRNA were varied

from 0.1–5 mM, 10-100 µM, and 1–10 µM, respectively. Similarly,10 nM recombinant protein along with 1.25 mM DTT, 2 mM ATP, 15 mM $MgCl_2$, 15 mM KCl, and 2 U/ml inorganic pyrophosphatase were dissolved in aminoacylation buffer made up of 50 mM HEPES pH 7, 150 mM NaCl. The kinetics of mutant proteins (*Ld*HisRS-E157A and *Ld*HisRS-R164A) was also performed with similar strategy.

The stability of the recombinant proteins was studied and compared at varying temperatures (10–80°C) and pH (4–10). Moreover, the effect of divalent (Mg^{2+}, Mn^{2+}, Ca^{2+}, Cd^{2+}, Zn^{2+}, and Fe^{2+}) and monovalent (Li^{+}, Na^{+}, K^{+}, and Cs^{+}) metal ions on the aminoacylation of purified proteins was checked. After adding the components, each reaction was incubated at 37°C for 30 minutes then terminated with a malachite green solution and the readings were taken at 620 nm using the Infinite M PLEX multimode reader. All of the aminoacylation reactions were conducted in duplicates with their respective blanks.

2.2.5. Inhibition by benzothiazolo-coumarin derivatives

The benzothiazolo-coumarin derivatives synthesized by our collaborators from NIPER, Hyderabad were dissolved in DMSO (Dimethyl sulfoxide) to obtain the final concentration as 5 mM. To calculate their IC_{50} (half-maximal inhibitory concentration) against aminoacylation activity of recombinant proteins, the synthesized compounds were added in the range of 0–15 µM. IC_{50} values were computed by keeping X-axis as the log of inhibitor concentration and the normalized percentage activity was placed on the Y-axis. For determining their mode of inhibition, Lineweaver-Burk plots with different inhibitor concentrations. All the reactions were conducted in duplicates alongside their respective blanks, while the readings were taken exactly at the same time intervals, and graphs were plotted employing GraphPad Prism version 8.0 (https://www.graphpad.com/scientific-software/prism/). The ADME properties of hit compounds were computed using the SwissADME online server (http://www.swissadme.ch/).

2.2.6. Cytotoxicity assay of hit compounds

The murine macrophage (RAW 264.7) cell line, a kind gift from Dr. Nooruddin Khan (University of Hyderabad, Hyderabad, India), was taken to evaluate the cell viability in the presence of inhibitors as described earlier [52]. It is a regularly used cell line and was ascertained based on typyical morphological characteristics and adherence. Briefly, the cells were grown in Dulbecco's

Modified Eagle Medium (DMEM) supplemented with 10% Fetal Bovine Serum (FBS) and 1% penicillin–streptomycin at 37 °C with 5% CO2. Approximately $0.1x10^{-6}$ cells were seeded into each well of a 96-well plate, and the cells were then incubated overnight at 37 °C for proper adhering. The following day, lead compounds were added from 1 to 200 µM, and its effect was checked post 24 h by adding MTT [3-(4,5- dimethyl-2-thiazolyl)-2,5-diphenyltetrazolium bromide] at a final concentration 0.5 mg/mL followed by incubation for 4 h at 37 °C in the dark. The supernatant was carefully removed, and the formazan crystals were dissolved in 100 µl DMSO prior to absorbance at 570 nm with 630 nm as a reference. The experiment was carried out in a mycoplasma-free macrophage cell line.

2.2.7. EMSA of *Ld*ArgRS and its deletion mutant

RNA EMSA was executed through the Electrophoretic Mobility Shift Assay kit (Invitrogen). The concentrations of *Ld*ArgRS and ΔIns-*Ld*ArgRS were varied from 0 to 4 µM, while 70 ng of total ytRNA was used for the study. The protein-ytRNA mixture was dissolved in 1X binding buffer comprising 10 mM Tris pH 7.4, 150 mM KCl, 0.1 mM EDTA (Ethylenediaminetetraacetic Acid), and 0.1 mM DTT, and incubated at 25°C for 30 minutes. The samples were then mixed in 6X loading dye, loaded onto 6% non-denaturing polyacrylamide gel, and run for 45 minutes at 140 V and 4°C in 0.5X TBE (Tris-Borate-Acetic acid) buffer. The SYBR Green EMSA stain was prepared by adding 5 µl of component A to 50 ml 1X TBE. The gel was carefully removed, stained with 1X SYBR Green EMSA staining solution for 20 minutes, and visualized by 590/110 UV transilluminator filter.

2.2.8. MST analyses of *Ld*ArgRS and its deletion mutant

The lysine residues of *Ld*ArgRS and ΔIns-*Ld*ArgRS were covalently labeled with the help of Protein Labelling kit RED-NHS 2nd Generation (NanoTemper Technologies, GmbH, USA). The proteins were initially prepared as 10 µM samples and the dye was added in three times excess followed by incubation in the dark for 30-45 mins after which the unlabelled dye was removed with the help of a B-column. Subsequently, 20 nM of labeled protein was taken as the final concentration, supplemented with 0.1% pluronic acid and serial dilutions of ytRNA were prepared (150 µM to 4.5 nM). The samples were briefly incubated for 5-10 minutes on ice from which 10

µl of each sample was loaded into capillaries, and shift in emission spectra was measured using Monolith X instrument.

2.2.9. Fluorescence spectroscopy

For fluorescence measurements, 1 µM of protein was added in the buffer containing 30 mM (*Ld*ArgRS) or 50 mM (*Ld*HisRS) HEPES pH 7 and 150 mM NaCl at 25°C. The intrinsic fluorescence of aromatic residues was utilized and the changes in conformation were recorded (Excitation at 280 nm and Emission from 300 to 400 nm) using Spectrophotometer FP-8500 (Jasco, Japan) at a scan rate of 100 nm/sec while every experiment was performed in duplicates. The effect of pH (4–10) on the intrinsic fluorescence of recombinant proteins was studied in buffers containing 30 or 50 mM each of sodium acetate/ citrate, Tris, and CAPS with 150 mM NaCl by incubating the protein for 30 minutes on ice in the corresponding pH buffers, after which the readings were taken. Likewise, the localization of aromatic residues was determined by adding fluorescence quenching reagents such as acrylamide and KI to recombinant proteins, followed by incubation on ice for half an hour before fluorescence measurements. The relative fluorescence intensities acquired were converted to a modified Stern-Volmer equation, and the graphs were plotted with Log(F_0-F_1/F_1) on the Y-axis against Log(quencher) on the X-axis, where F_0 and F_1 are the corresponding fluorescence intensities of control and observed. A similar strategy was used to calculate the binding affinity values for the inhibitor towards the proteins, wherein the inhibitor concentration was varied from 0 to 15 µM. The extrinsic fluorophore, ANS was added at a 5 µM concentration and excited at 380 nm to study the change in the hydrophobic environment in the presence or absence of inhibitor.

2.2.10. CD measurements

In order to structurally characterize the recombinant proteins**,** the Far-UV CD spectrum was recorded for 1 µM of the protein dissolved in 10 mM HEPES pH 7 using quartz cell of 0.2 cm path length on J-1500 CD Spectrophotometer (Jasco, Japan) with a scan speed of 50 nm/sec in duplicates. The effect of pH over a range of 4 to 10 on structural conformations was also checked in buffers containing 10 mM each of sodium acetate/citrate (pH 4-6), Tris (pH 7-9), and CAPS (pH 10). The stability of the proteins was validated in the presence of denaturants like urea and guanidine hydrochloride (GdHCl) at a range of 0–6 M. Likewise, the thermal stability of the

proteins in the absence or presence of their ligands was verified by increasing temperature from 20 to 70°C, and the ellipticity change was monitored at 222 nm with 1°C/min scan speed. The spectra were examined through the DichroWeb online server (http://dichroweb.cryst.bbk.ac.uk/html/home.shtml), and the normalized values were plotted employing GraphPad Prism.

2.2.11. Structure prediction and docking studies

The *Ld*ArgRS and *Ld*HisRS structures were taken from the AlphaFold Protein Structure Database (https://alphafold.com), and their stereo-chemical properties were validated through PROCHECK (https://saves.mbi.ucla.edu). The structures were further refined by employing ModLoop (https://modbase.compbio.ucsf.edu/), and visualized with PyMOL software (https://pymol.org/2/). A total of eight leishmanial $tRNA^{Arg}$ isoforms were found in the gtRNAdb database (http://gtrnadb.ucsc.edu/GtRNAdb2/), and one of the tRNA sequence (Gene: tRNA-Arg-ACG-1-1) was retrieved. Subsequently, the structure of $tRNA^{Arg}$ was generated using the RNA composer online tool (https://rnacomposer.cs.put.poznan.pl). The generated tRNA structure was used to dock with *Ld*ArgRS structure through the HDOCK server (http://hdock.phys.hust.edu.cn). The coordinates of ATP and L-Arg, were retrieved from the PubChem database (https://pubchem.ncbi.nlm.nih.gov), and PDB ID: 4Q2T (https://www.rcsb.org/), respectively. Similarly, for *Ld*HisRS, the coordinates of ATP and L-His were taken from the corresponding PDB IDs 3HRK and 3LC0. The chemical structure of inhibitors was drawn using ChemDraw Pro 8.0 [53] and converted into PDB format with the help of OPENBABEL online tool (http://www.cheminfo.org/). The docking of ligands with *Ld*HisRS and *Ld*ArgRS was done through AutoDock Vina 1.1.2 [54] and the interactions between them were visualized in LigPlot [55].

2.2.12. Molecular dynamic simulations

The apo proteins (*Ld*ArgRS and *Ld*HisRS) and their complexes were subjected to MDS studies in the GROMACS software [56]. The topologies of proteins were generated by executing CHARMM36 force field, while the topologies of $tRNA^{Arg}$ and other ligands were created with CHARMM GUI online software (https://charmm-gui.org/). The complexes were put at the center of a cubic box, and the water model used for the study was SPC/E [57]. The systems were then

neutralized, and indexing of the protein-ligand complexes was performed separately to positionally restrain the ligands, following which the parameters were added to their respective topology files. The energy minimization of all the systems was executed by employing the steepest descent algorithm. Subsequently, two steps of equilibration, *viz.*, NVT and NPT, were performed for each run of 1 ns, and then the production of MD was achieved at 300 K for a span of 100 ns, followed by plotting the RMSD, Rg, and RMSF graphs as described previously [58]. The binding energy of the ligands with *Ld*HisRS was also computed with the help of Molecular Mechanics Poisson-Boltzmann Surface Area (MM/PBSA). The thermodynamic stability of *Ld*HisRS and its mutants at 328 K was understood with 2D free energy landscape (FEL) diagrams that were generated utilizing principal components, PC1 and PC2. By employing MD simulations as the sampling technique, free energy conformations were obtained from the last 60 ns.

Chapter-I

3. To clone and purify arginyl- and histidyl-tRNA synthetases of *Leishmania donovani*

3.1. Result

3.1.1. Leishmanial ArgRS possesses insertion specific to trypanosomatids

The evolutionary linkage was deduced among the ArgRSs belonging to different domains of life, i.e., archaea, bacteria, and eukaryotes (Figure 4). In total, five major clades were observed, in which the clade consisting of mammalian ArgRSs segregated as the earliest formed enzymes that were paraphyletic to the clades containing ArgRSs from nematodes and arthropods. On the other hand, the clades possessing ArgRSs from trypanosomatids and most of the apicomplexans were paraphyletic to each other, while *P. falciparum* formed a separate clade. Succeeding the lineage of trypanosomatids and apicomplexans, the clade containing bacterial ArgRSs was present, followed by fungi. *Ld*ArgRS comprises 692 aa (amino acids) that corresponds to 78.2 kDa protein with 5.8 as its isoelectric point (pI). Comparative sequence analysis of ArgRSs indicates the presence of a long insertion (110 aa) within the CCD of trypanosomatids that is absent in human ArgRS (Figure 5). Further analysis of *Ld*ArgRS sequence using BLASTp tool (data not shown) suggests the existence of this insertion only in trypanosomatids, making it a peculiar feature of their ArgRSs. Previously, the CCD of *Thermus thermophilus* AspRS was reported to possess an insertion of 120 aa resembling the GAD (GatB-AaRs-for-Asp) domain of GatB (the B-subunit of archaeal Glu-$tRNA^{Gln}$ amidotransferases) [59, 60]. This GAD domain is accountable for stabilizing tRNA binding with aaRSs. Moreover, a consensus sequence similar to xSKxxLKKxxK is also present in the trypanosomatid-specific insertion that has been previously identified as an anticodon binding motif in the class-IIb eukaryotic aminoacyl-tRNA synthetases [61]. In *Ld*ArgRS, this motif was present between Leu355 and Lys365, which contained residues in the order of $L_{355}S_{356}K_{357}K_{358}E_{359}V_{360}K_{361}P_{362}W_{363}N_{364}K_{365}$. The active site motif was present on either side of the trypanosomatid-specific insertion, and considerable differences were observed between human and leishmanial active site motifs. For example, the residues Ser200, Val238, Val407, Val408, and Leu445 in *Hs*ArgRS have been replaced by Ala132, Ile170, Cys449, Thr450, and Thr485 in *Ld*ArgRS, respectively. The HIGH motif consisted of H140-V141-G142-H143 and the KMSKS residues were found replaced by KKIKT (K490-K491-I492-K493-T494). Furthermore, the last residue methionine has been replaced by isoleucine for trypanosomatids, however, in most of the cases, the methionine residue exerts conformational changes that help in proper anticodon binding [62].

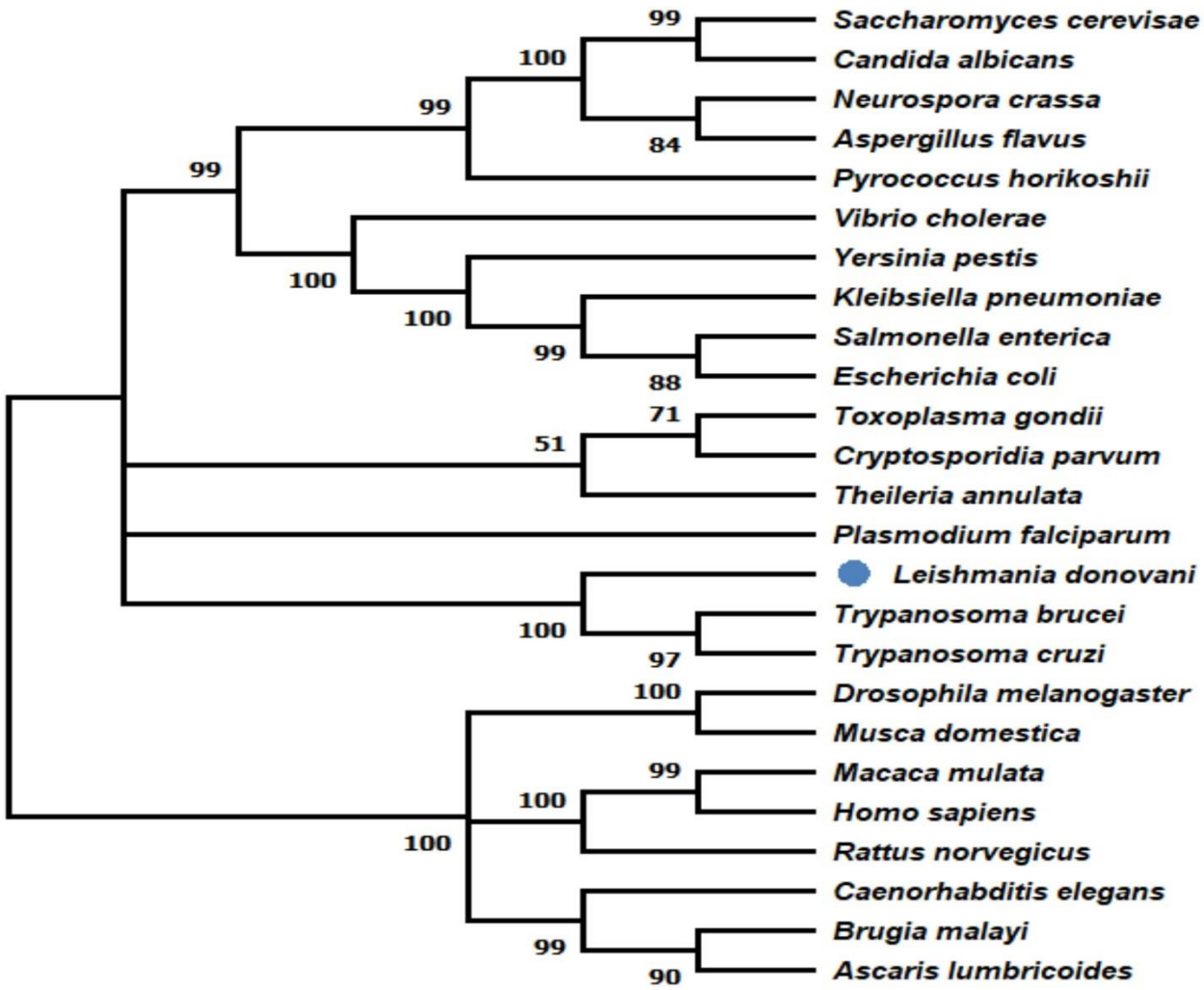

Figure 4: Comparison of arginyl-tRNA synthetase (ArgRS) sequences. Evolutionary analysis of arginyl tRNA synthetases from different organisms. The rooted phylogenetic tree was constructed using the Neighbor-Joining method with 1000 bootstrap repeats and the percentage of replicate trees with which each of the taxa clustered together is mentioned on the branches**.**

Figure 5: Global sequence alignment of ArgRSs from trypanosomatids and *H. sapiens.* Corresponding UniProt IDs of *Ld*ArgRS, *Tb*ArgRS, *Tc*ArgRS, and *Hs*ArgRS are A0A3Q8IED7, Q386W0, Q4E397, and P54136 and were obtained from the UniProt database (https://www.uniprot.org). Blue stars and green circles represent ATP and L-Arg binding motifs, respectively. The consensus tRNA binding motif has been indicated with a black box. The blue boxes represent sequence similarity or identity.

3.1.2. Comparison of HisRS sequences

The phylogenetic tree divided HisRSs into clades according to the taxa of organisms from where they have been retrieved (Figure 6). It was noticed that *Plasmodium falciparum* HisRS is closer to HisRSs from trypanosomatids, while other apicomplexa HisRSs constituted a different clade. The trypanosomatid HisRSs were also observed to be distantly related to human HisRS and to further analyze their sequences, a global sequence alignment was executed (Figure 7). The Pfam server was used to predict the arrangement of *Ld*HisRS domains and the active site residues were reckoned from the *T. cruzi* HisRS-histidyl-adenylate structure (PDB ID: 3HRK). *Leishmania donovani* HisRS (*Ld*HisRS) harbors NTD (N-terminal domain, Met1-Lys40), CCD (Catalytic core domain, Lys41-Ser378), and CTD (C-terminal domain, Leu379-Leu473). The WHEP domain is also found towards NTD which is reported in other eukaryotes [60], whereas an ID (insertion domain, Ser210-Leu286) connects motif 2 and 3 of CCD. The ID plays an important role during histidine adenylation when the tRNA is absent [63] and the conservation of amino acid sequence at this region is high within eukaryotes, while it is very low among the prokaryotic HisRSs [45]. The interacting residues with L-His and ATP were observed to be identical in trypanosomatids excluding Ile335 in *Leishmania* that is exchanged by Leu336 in *Trypanosoma* HisRSs, while in *Hs*HisRS some of these residues were different. The active site residues in the leishmanial enzyme viz., Glu125, Glu157, Arg164, Ala334, and Leu335, have been substituted by Asp130, Pro161, Tyr168, Ser356, and Val357, respectively in its human counterpart. These differences between *Ld*HisRS and *Hs*HisRS are intriguing, particularly at the Glu157 and Arg164 positions as the residues are electrochemically dissimilar in *Hs*HisRS. *Ld*HisRS is made up of 473 amino acids, out of which four are tryptophan residues and the theoretical pI of the protein is 5.81.

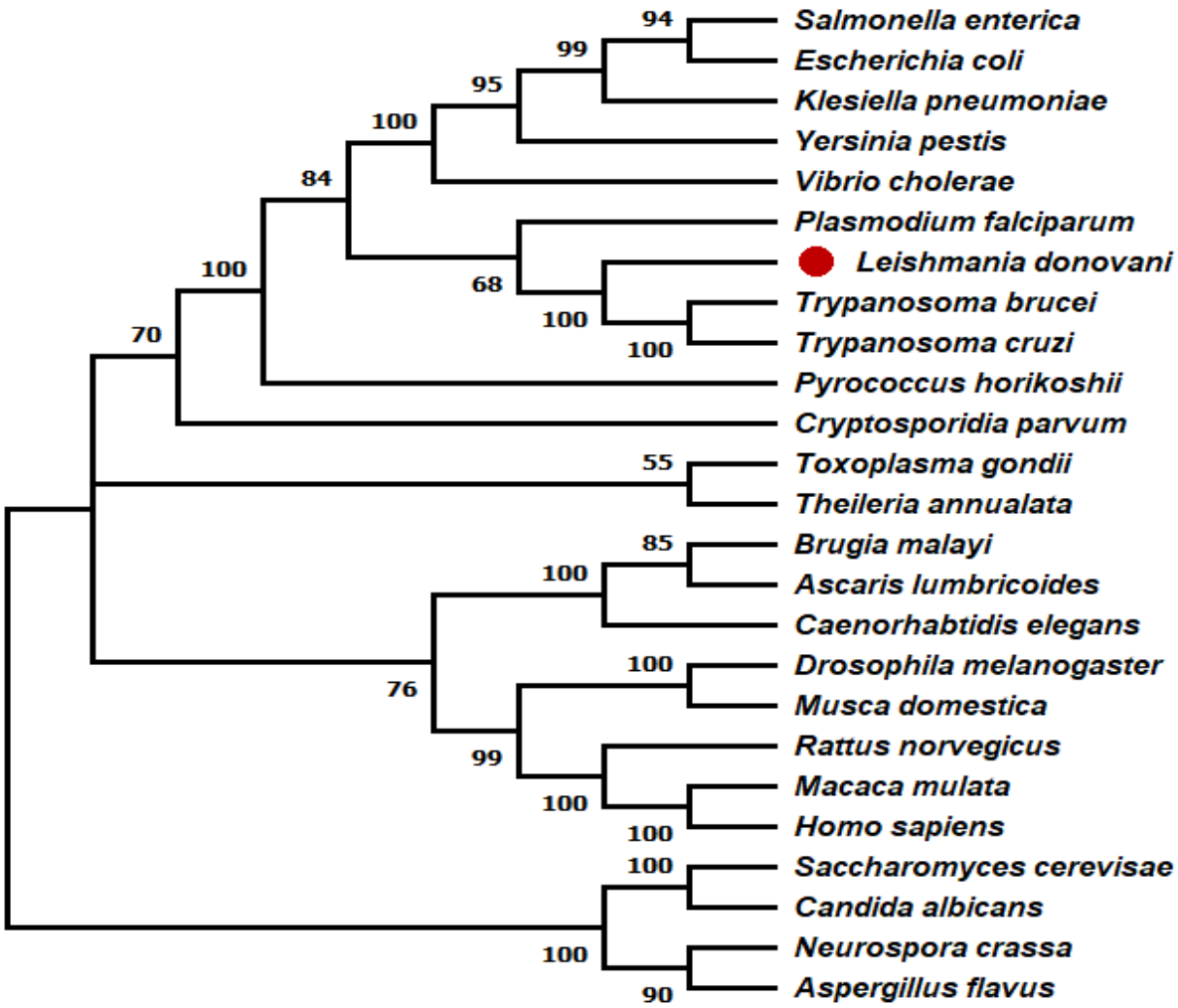

Figure 6: Evolutionary analysis of HisRS from different organisms. The rooted tree was achieved after 1000 bootstrap repeats by using the Neighbor-Joining method. For every segregating branch, the percentage of divergence is indicated.

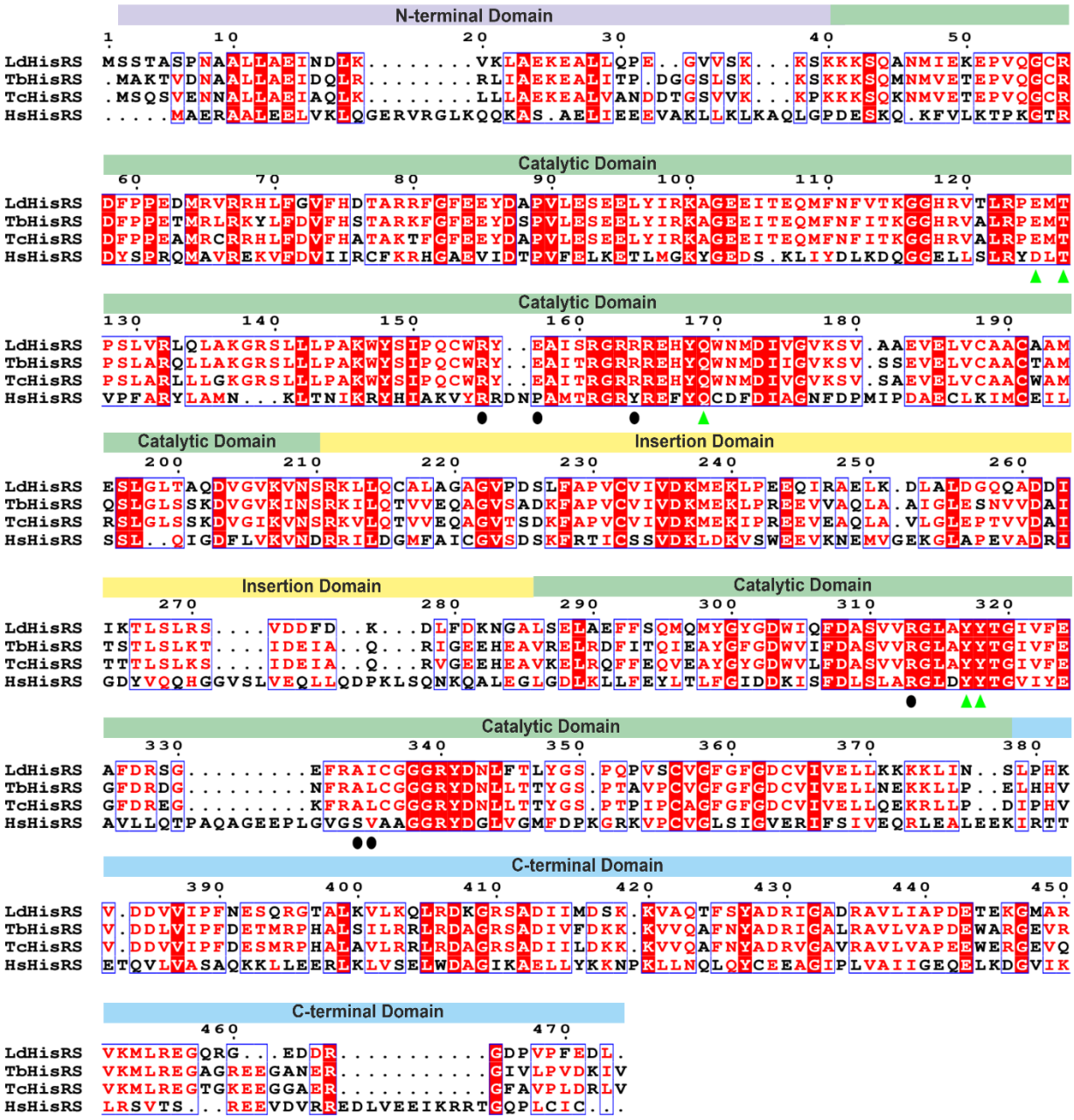

Figure 7: Comparison of HisRSs from various organisms. Multiple sequence alignment of *Ld*HisRS, *Tc*HisRS, *Tb*HisRS, and *Hs*HisRS. The black circles and green triangles correspondingly indicate ATP and L-His interacting residues. The NTD (N-terminal domain), CCD (Catalytic core domain), ID (Insertion domain), and CTD (C- terminal domain) are shown as purple, green, yellow, and blue boxes, respectively.

3.1.3. Cloning of arginyl- and histidyl-tRNA synthetases

In the course of evolution, trypanosomatids have integrated a unique and large insertion within the CCD of ArgRS. Thus, in order to investigate its possible role, *Ld*ArgRS, ΔIns-*Ld*ArgRS, and *Hs*ArgRS were cloned into the pET28a(+) expression vector. The amplified ORFs of *Ld*ArgRS and *Hs*ArgRS could be seen as 2.1 and 1.9 kb approximately (Figure 8A & B). The full-length *Ld*ArgRS was used for the derivation of its deletion mutant by SOE-PCR technique. The amplified bands of the first half of the gene, i.e., prior to the novel insertion (897 bp), and second half of the gene (852 bp), were used for the next set of PCR reactions wherein the flanking sequences could be added (Figure 8C). The fifth PCR used the flanking sequences as primers and the entire stretch of 1.7 kb nascent ORF was amplified (Figure 8D). All of these clones were subsequently confirmed through double digestion (Figures 8E-G).

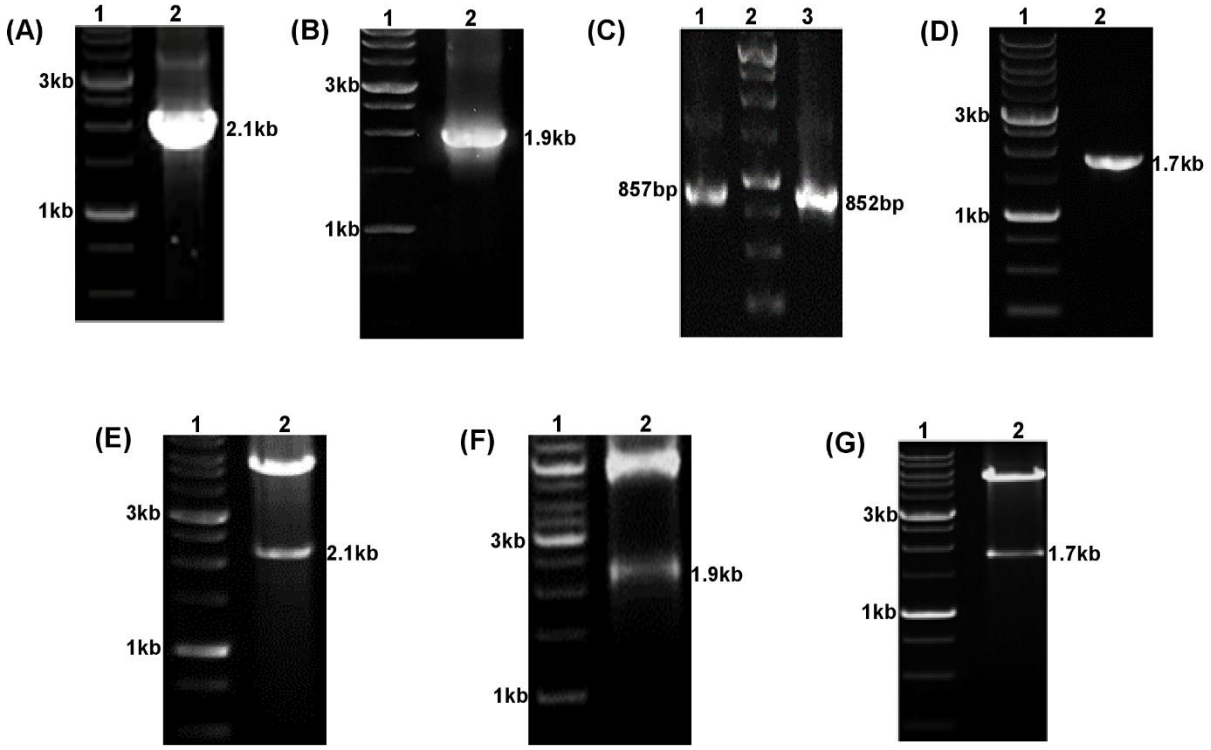

Figure 8: Cloning of ArgRSs in pET28a(+) expression vector. (A & B) Amplification of ArgRSs from *Leishmania donovani* genomic DNA and cDNA of human myeloid fibroblast cells, respectively; (C) Amplification of the first half of *Ld*ArgRS (lane 1), 1 kb DNA ladder (lane 2), and the second half (lane 3) of *Ld*ArgRS; (D) Amplification of ΔIns-*Ld*ArgRS; Double digestion of *Ld*ArgRS-pET28a(+) (E), *Hs*ArgRS-pET28a(+) (F), and ΔIns-*Ld*ArgRS-pET28a(+) with *Nde*I and *Eco*RI (G).

Similarly, the same expression vector was employed for the cloning of *Ld*HisRS and its human counterpart while the mutants were generated through primers with specific mutations. The full-length ORF of *Ld*HisRS (1.42 kb, Figure 9A) and *Hs*HisRS (1.53 kb, Figure 9B) were amplified from *Leishmania donovani* genomic DNA and human myeloid fibroblast cDNA, respectively by implementing gene-specific primers. The constructs were confirmed by double digestion and further validated by DNA sequencing (Figure 9C-D).

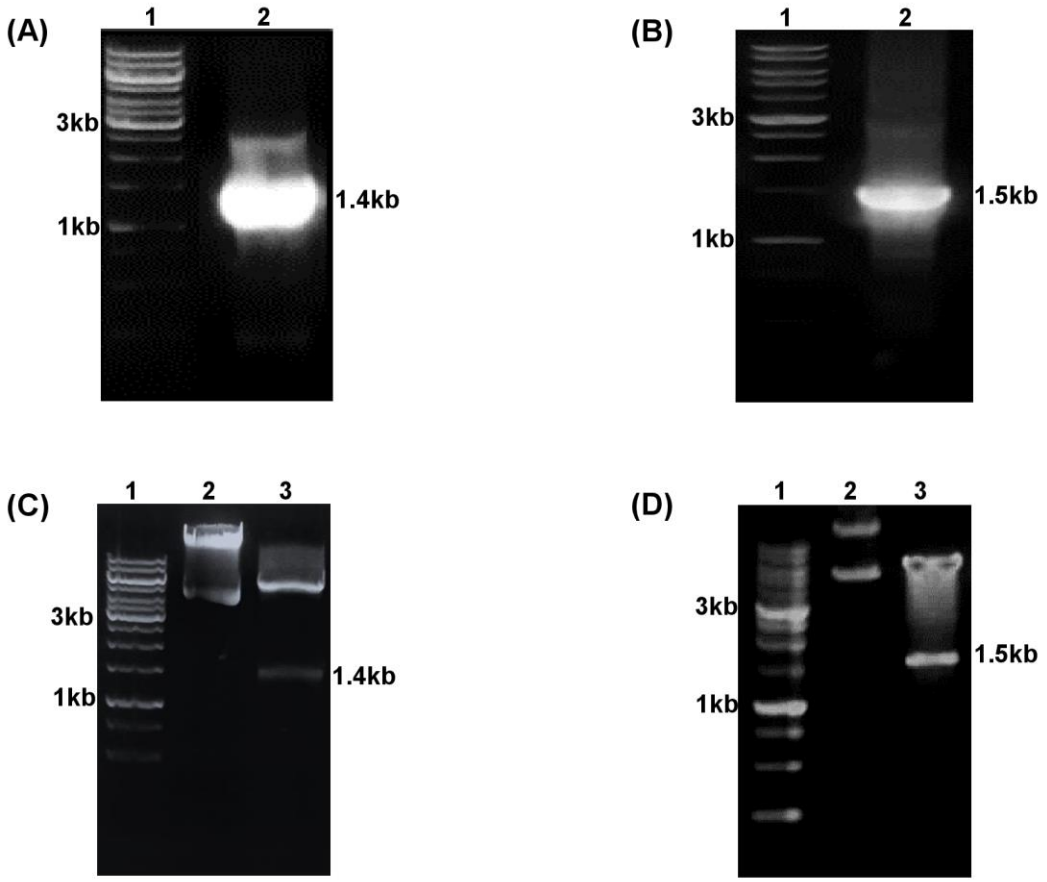

Figure 9: Molecular cloning of HisRSs. Amplification of HisRSs from (A) *Leishmania donovani* genomic DNA and (B) cDNA of human myeloid fibroblast cells, wherein lanes 1 and 2 of each gel correspondingly represent 1 kb DNA ladder and amplified ORFs; Confirmations of (C) *Ld*HisRS-pET28a(+) and (D) *Hs*HisRS-pET28(+) wherein lanes 1, 2, and 3 represent 1kb DNA ladder, undigested construct, and double digested construct with *Nde*I and *Eco*RI.

3.1.4. Purification of tRNA synthetases to homogeneity

After confirmation by double digestion and DNA sequencing all of the plasmids containing native and mutanted genes were transformed into *E. coli* BL21(DE3) cells for expression of recombinant proteins. To determine the optimum IPTG concentration for protein induction, *Ld*ArgRS and ΔIns-*Ld*ArgRS were subjected to 0, 0.1, 0.25, and 0.5 mM IPTG. Thick bands of *Ld*ArgRS (Figure 10A) and ΔIns-*Ld*ArgRS (Figure 10B) overexpression were visible on 10% SDS-PAGE in the cells treated with IPTG, while no protein expression was noticed in the uninduced cells. The optimum IPTG concentrations was estimated as 0.5 mM for both the recombinant proteins and they could be successfully brought to homogeneity with the help of Ni-NTA, followed by size-exclusion chromatography. The purified *Ld*ArgRS, ΔIns-*Ld*ArgRS, and *Hs*ArgRS could be seen as ≈80 kDa (78.2 kDa+2 kDa His-Tag), ≈69 kDa (67 kDa+2 kDa His-Tag), 75 kDa (73 kDa+2 kDa His-Tag) recombinant proteins when run on a 10% SDS-PAGE gel (Figure 10C). The full-length *Ld*ArgRS solubility and yield were higher than its deletion mutant, i.e., 2 mg/ml (*Ld*ArgRS) versus 0.5 mg/ml (ΔIns-*Ld*ArgRS) per one-liter culture. The oligomeric state of *Ld*ArgRS was found to be dimeric, while that of ΔIns-*Ld*ArgRS as monomeric in solution (Figure 10D). Similarly, the optimal IPTG concentration for inducing these proteins was observed to be 0.5 mM for *Ld*HisRS. The induced *Ld*HisRS and its mutants (55 kDa) were visible on the next lane to the protein ladder (Figure 11A). The recombinant proteins were purified using Ni-NTA affinity and gel filtration chromatography (Figure 11B), while the 110 kDa of native *Ld*HisRS indicate its dimeric state.

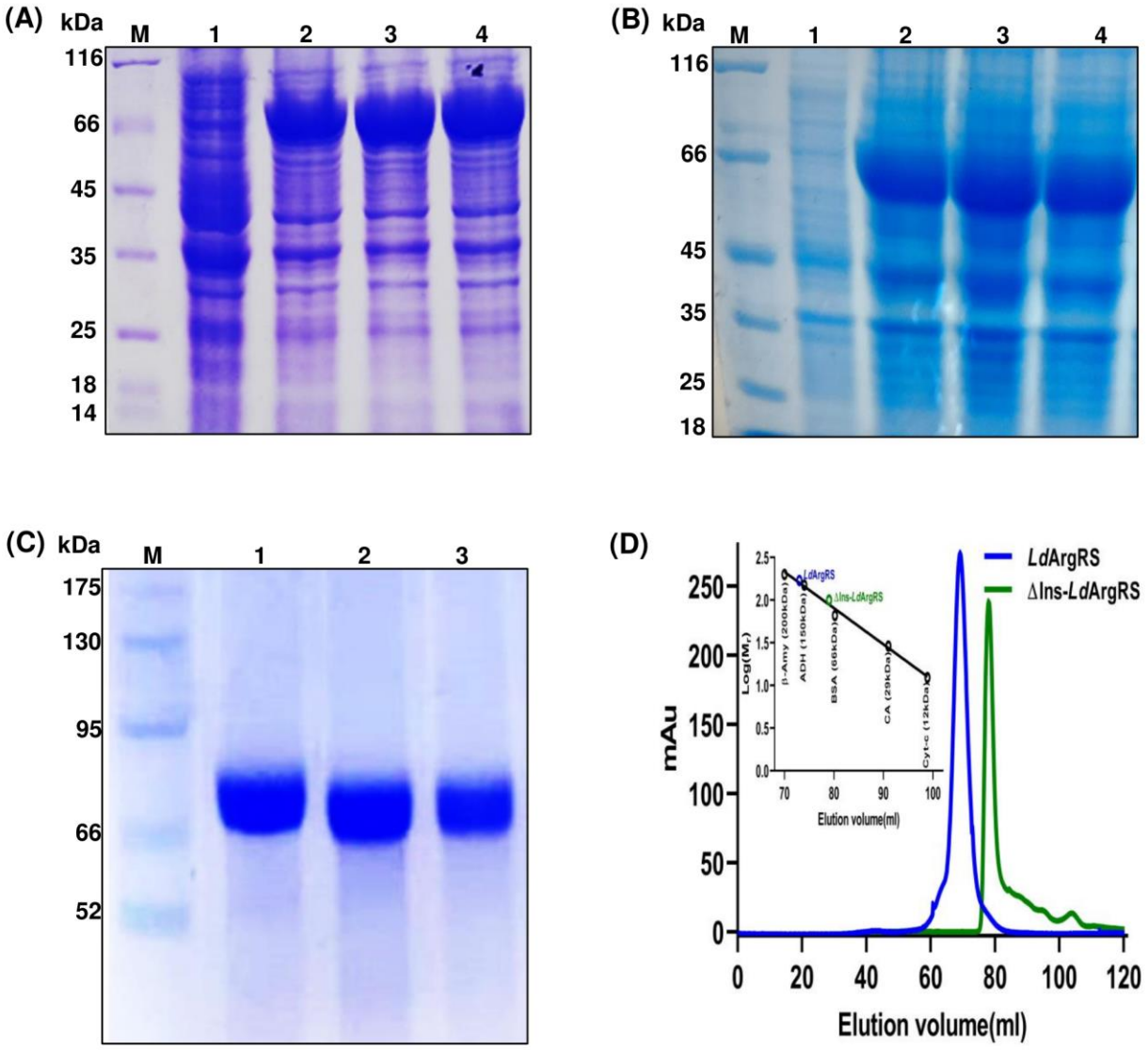

Figure 10. Purification of *Ld*ArgRS, ΔIns-*Ld*ArgRS, and *Hs*ArgRS. 10% SDS-PAGE exhibiting overexpression of proteins for (A) *Ld*ArgRS and (B) ΔIns-*Ld*ArgRS. Lane M of each gel corresponds to protein marker, lane 1, 2, 3, and 4 represent cells treated with 0, 0.1, 0.25, and 0.5 mM IPTG, respectively; (C) 10% SDS-PAGE gel of purified proteins depicting protein marker (lane M), *Ld*ArgRS: 80 kDa (lane 1), ΔIns-*Ld*ArgRS: 69 kDa (lane 2), and *Hs*ArgRS: 75 kDa (lane 3); (D) Molecular weight determination of *Ld*ArgRS and ΔIns-*Ld*ArgRS using size-exclusion chromatography, the inset displays a plot of standard proteins comprising b-Amylase (b-Amy: 200 kDa), Alcohol Dehydrogenase (ADH: 150 kDa), Bovine Serum Albumin (BSA: 66 kDa), Carbonic Anhydrase (CA: 29 kDa), and Cytochrome-c (Cyt-c: 12 kDa)

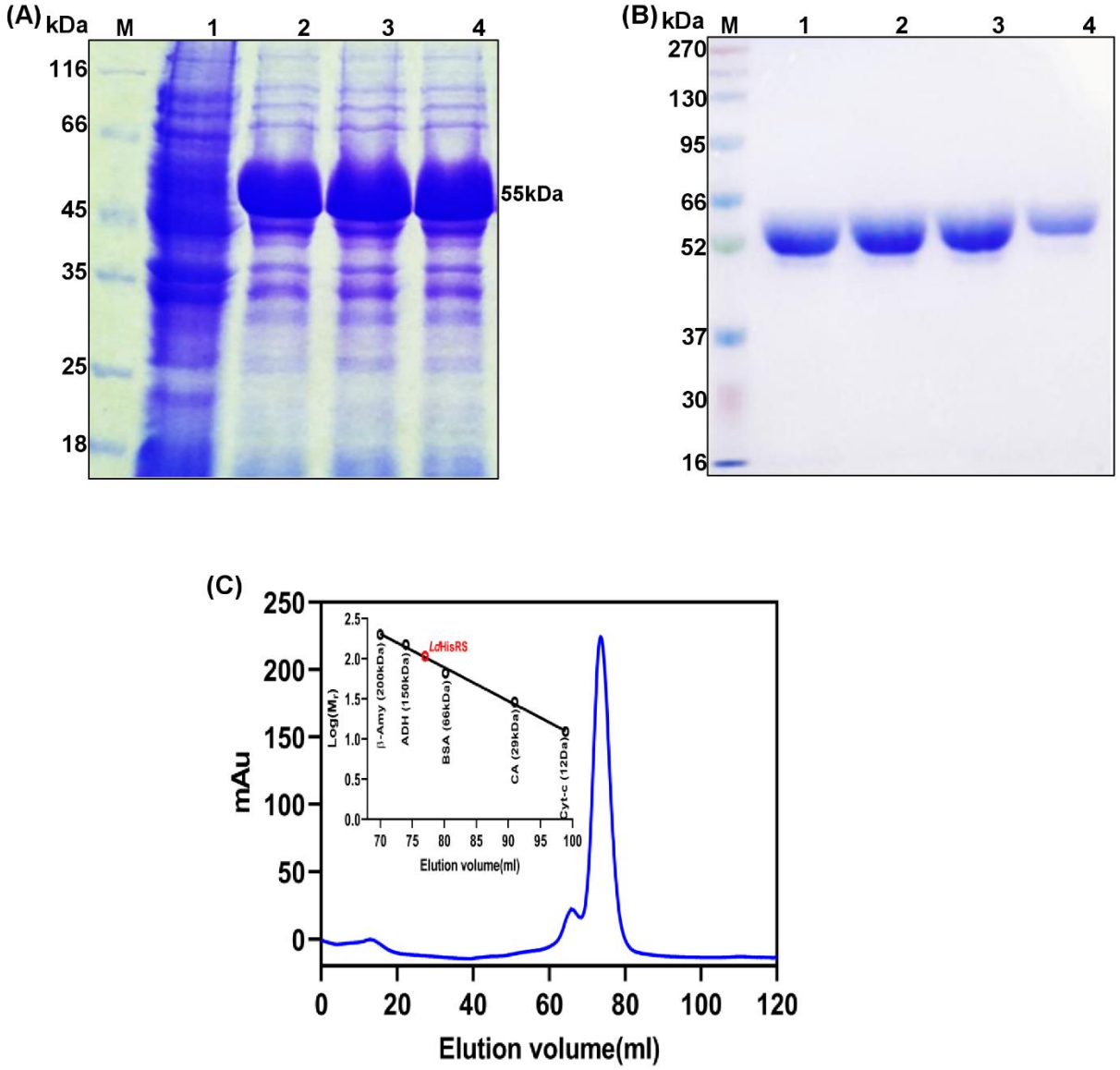

Figure 11: Purification of HisRSs. (A) Expression of leishmanial HisRS with lane M representing protein marker, lanes 1, 2, 3, and 4 showing protein induction at 0, 0.1, 0.25, and 0.5 mM IPTG concentrations, respectively; (B) Purified proteins on 10% SDS-PAGE with lane M: protein ladder, lane 1: 55 kDa *Ld*HisRS, lane 2: 55 kDa *Ld*HisRS-E157A, lane 3: *Ld*HisRS-R164A, and lane 4: 58 kDa *Hs*HisRS; (C) Dimeric state of *Ld*HisRS on size-exclusion chromatogram, the inset is a plot of protein standards as shown in Figure 10.

3.1.5. Trypanosomatid-specific insertion renders conformational changes in *Ld*ArgRS

In order to study the differences in conformation rendered by the trypanosomatid-specific insertion, *Ld*ArgRS and ΔIns-*Ld*ArgRS were subjected to fluorescence spectroscopy with varying pH. The effect of pH could be vividly observed for both proteins with red and blue shifts. At acidic pH (4 and 5), *Ld*ArgRS showed a blue shift, and when present in a buffer of pH 10, it showed a red shift (Figure 12A). However, a red shift was observed at acidic pH (4-6) for ΔIns-*Ld*ArgRS, and no shift of wavelength was found from pH 7 to 10 (Figure 12B). *Ld*ArgRS consists of 29 phenylalanine, 20 tyrosine, and 6 tryptophan residues out of which 3 phenylalanine, 2 tyrosine, and 1 tryptophan are present in the insertion region. Hence, comparative computational and quenching analyses were performed to determine their proximate location in the full-length protein as well as its deletion mutant. As per the WESA software, 10 aromatic residues, viz., 5 tyrosine (Tyr191, Tyr242, Tyr270, Tyr330, and Tyr455), 1 tryptophan (Trp470), and 4 phenylalanine (Phe395, Phe411, Phe413 and Phe633) from *Ld*ArgRS, were exposed to the solvent milieu. However, in ΔIns-*Ld*ArgRS, 7 aromatic residues were present on the surface, viz., 4 tyrosine (Tyr191, Tyr242, Tyr270, and Tyr344), and 3 phenylalanine (Phe300, Phe302, and Phe522). Hence, it can be inferred that 18.18% of *Ld*ArgRS and 14.28% of ΔIns-*Ld*ArgRS aromatic residues are present on the respective protein surfaces. The removal of insertion also led to the shifting of Trp359 to a hydrophobic environment in ΔIns-*Ld*ArgRS that was previously exposed in *Ld*ArgRS (Trp470). In order to understand the location of these residues, the quenching of their intrinsic fluorescence was studied through *in vitro* experiments, and it was observed that both the proteins could be efficiently quenched by acrylamide from 0.075 to 0.5 M (Figure 12C and E). This is in correlation with the prediction of WESA server that indicated the presence of many aromatic residues in the hydrophobic core of *Ld*ArgRS and ΔIns-*Ld*ArgRS. Based on the binding constant values observed, it can be interpreted that *Ld*ArgRS requires comparatively more acrylamide to quench its intrinsic fluorescence (K_b= 2.34±0.35 M^{-1}, Figure 12D) than ΔIns-*Ld*ArgRS (K_b=1.35±0.16 M^{-1}, Figure 12F). This might be attributed to the lesser number of aromatic residues in ΔIns-*Ld*ArgRS than its full-length form. Quenching of *Ld*ArgRS with potassium iodide (KI) was not successful as the fluorescence intensity kept on fluctuating, however, the same was not the case for ΔIns-*Ld*ArgRS. The K_b of KI towards ΔIns-*Ld*ArgRS was found to be 1.33±0.2 M^{-1} (Figure 12G and H).

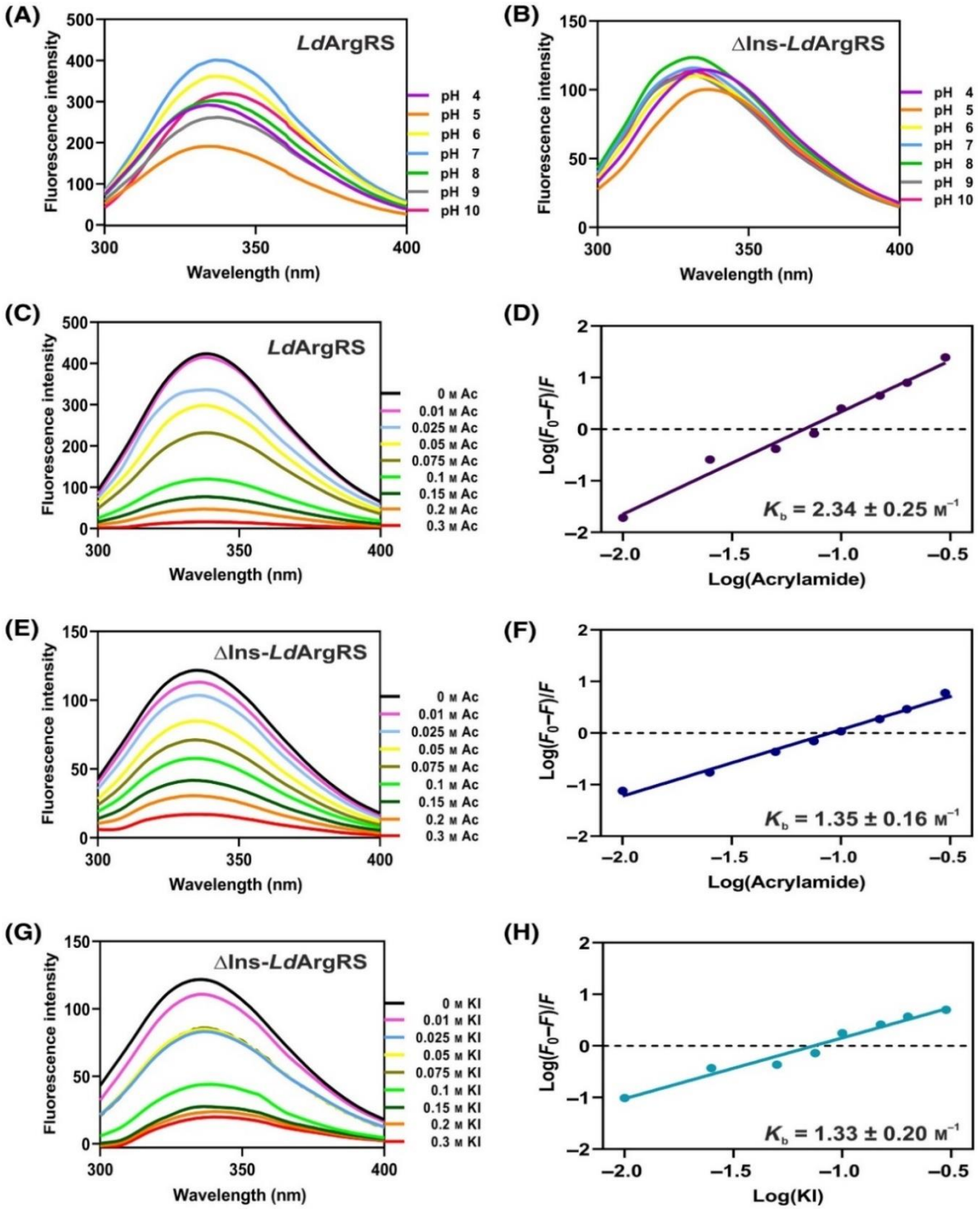

Figure 12: Intrinsic fluorescence of *Ld*ArgRS and ΔIns-*Ld*ArgRS. (A and B) Effect of pH on conformational changes of proteins; Decrease in fluorescence intensity of purified proteins in the presence of acrylamide (C and E), and potassium iodide (G) with their respective modified Stern-Volmer plots (D, F, and H); K_b values computed are mean ± SD from two different experiments with P-value <0.0001 calculated from one-way ANOVA.

3.1.6. Aromatic residues are buried in the hydrophobic core of *Ld*HisRS

In the physiological condition, λ_{max} (maximum intrinsic fluorescence) of *Ld*HisRS was recorded at 335 nm (Figure 13A). Near its isoelectric point, i.e. pH 6, the lowest intrinsic fluorescence intensity was recorded besides mild blue shift (Figure 13B), while at acidic pH (4 and 5), the highest intensities were noticed. However, no shift in the wavelengths was observed when the protein was subjected to other pH buffers, except for pH 10 where it depicted a mild red-shift. The WESA software located 1 tryptophan, 2 phenylalanine, and 2 tyrosine residues on the surface accounting for 13.1% of the total aromatic residues, thus indicating the presence of aromatic acids majorly in the hydrophobic core of *Ld*HisRS. The *in silico* analysis was validated by employing polar (potassium iodide) and non-polar (acrylamide) quenchers (Figure 13C and E). The corresponding K_{sv} (quenching constant) of acrylamide and potassium iodide were calculated to be 2.5±0.2 (Figure 13D) and 1.03±0.2 M^{-1} (Figure 13F), suggesting that the intrinsic fluorescence of *Ld*HisRS could be quenched with higher potassium iodide than acrylamide.

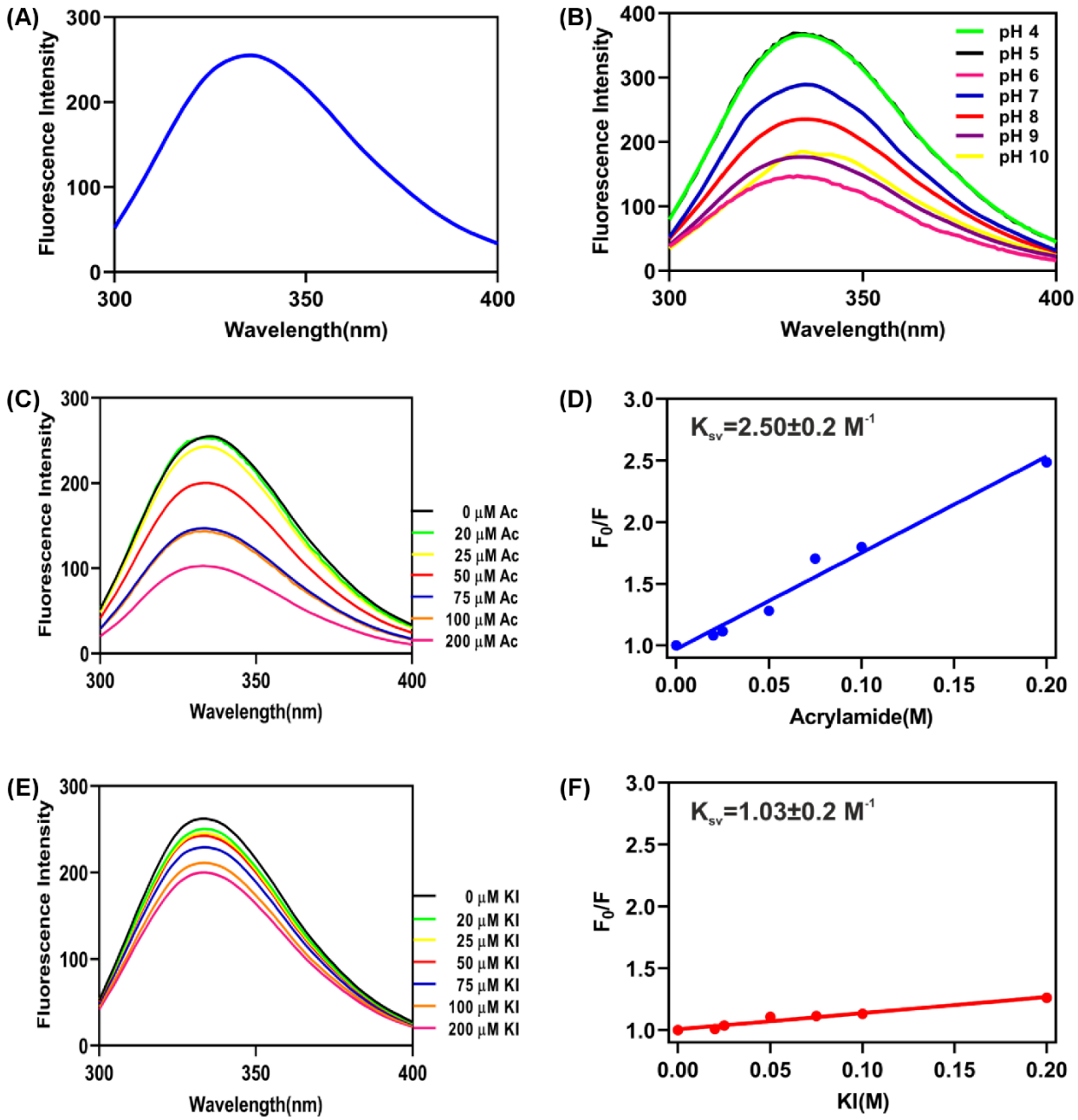

Figure 13: Intrinsic fluorescence of the leishmanial HisRS. (A) *Ld*HisRS fluorescence intensity at pH 7; (B) pH based conformational changes; Reduction in intrinsic fluorescence of purified protein in (C) acrylamide and (E) KI with their respective Stern-Volmer plots (D and F).

3.2. Discussion

Leishmaniases are the examples of evolutionary arms race wherein pathogens foster invasive strategies to defy the defense mechanism of their hosts. Due to the limitations posed by current antileishmanial remedies, it has become necessary to devise novel and effective therapeutic interventions to combat these diseases. Since the accuracy of protein translation is maintained by aaRSs, targeting these enzymes would hinder the cellular metabolism of leishmanial parasites. The distant segregation of trypanosomatid and mammalian ArgRSs in a rooted phylogenetic tree is in corroboration with a report that studied the gene organization of ArgRSs in detail [64]. Apart from evolutionary divergence, we found a 110 aa long insertion within ArgRS CCD that is idiosyncratic to trypanosomatids, and a similar case was noticed in the CCD of *T. thermophilus* AspRS [59]. Domains incorporated into CCD or ends of aaRSs have been previously associated with the enhancement of catalytic efficiency, tRNA binding, or editing mechanisms [59, 60, 65, 66, 67]. The human MetRS has also acquired a unique C-terminally appended domain that increases the protein's affinity for tRNA and is linked to the efficient capture of tRNA [68]. Moreover, the trypanosomatid-specific insertion contained a consensus sequence, which is important for RNA binding in aaRSs and RNA-recognizing proteins [69]. Removal of insertion changed the oligomeric state of *Ld*ArgRS and it is noteworthy that arginyl-tRNA synthetases have been reported in different forms of oligomerization viz., dimeric in *Homo sapiens* [70] and monomeric in *P. falciparum* [41]. A previous report has demonstrated the role of tRNA binding domain in the dimerization of class-I tRNA synthetases as it facilitates the communication between catalytic pocket of one monomer to the adjacent monomer [71]. The continuous fluctuations in fluorescence intensities of *Ld*ArgRS in the presence of ionic quencher, i.e., KI are possible only if the insertion is structurally dynamic causing constant alternation between buried and exposed states of tryptophan. At this juncture, it should be noted that of the 11 cysteine residues, none were present in the 110 aa long insertion, negating the possibility of any disulfide bond formation and thus, contributing towards its flexibility. It has previously been shown that *Tb*HisRS and *Tc*HisRS differ structurally from their human counterparts [45]. Furthermore, there were notable differences in the structure and amino acid sequence of the trypanosomal and *Hs*HisRS catalytic pockets [44]. This work further demonstrated that leishmanial HisRSs differ evolutionary from those of mammals as shown earlier [72]. Since the activation of histidine in the second monomer depends on the first monomer's aminoacylation being completed, the monomers must pair for the catalysis to occur

[73, 74]. It was observed that *Ld*HisRS's oligomeric state was dimeric, as reported in HisRSs from other organisms [45, 75, 76]. Additionally, it has also been formerly reported to be tetrameric [46, 77]. One of the most important differences between the leishmanial and human HisRS is the replacement of the ATP-interacting residues proline and tyrosine in *Hs*HisRS by glutamate and arginine in *Ld*HisRS, respectively. These residues are part of a motif that alters loop formation when attaching to the ATP adenyl group. Similar to leishmanial pyridoxal kinase, *Ld*HisRS demonstrated low fluorescence intensity near isoelectric point [78]. Moreover, the majority of the aromatic amino acid residues were located at the protein's hydrophobic core, which is comparable to *Ld*AspRS [34], *Ld*SerRS [51], *Ld*RPE [58], and *Ld*GluRS [79].

Chapter-II

4. To characterize the purified proteins biochemically and perform inhibition studies

4.1. Results

4.1.1. Trypanosomatid-specific insertion alters catalytic properties of *Ld*ArgRS

The full-length protein was capable of releasing pyrophosphate in the absence of tRNA at 0.25 µM in aminoacylation assays, and the PPi (inorganic phosphate) was detected with malachite green developing solution at 620 nm. Since ΔIns-*Ld*ArgRS mimics ArgRSs that lack such an insertion, its ability to catalyze the ATP-PPi exchange reaction was also checked in the absence of tRNA (Table 3). It was observed that ΔIns-*Ld*ArgRS lost about 90% of the enzyme activity at 0.25 µM concentration (Figure 14A). However, upon increasing the protein concentration, the protein gradually gained its activity up to 45% at 2 µM, beyond which not much increase in its enzyme activity was visible. This is in contrast to the 85% activity of *Ld*ArgRS at 2 µM. On varying pH, although the maximum activity for both proteins was observed at pH 7, their extent of aminoacylation differed at the basic pH (9-10) (Figure 14B). For *Ld*ArgRS, about 40–60% activity was seen from pH 3-6, after which a sharp increase in activity was observed till pH 7, followed by a gradual decrease to 50% in the basic pH (9 to 10). For ΔIns-*Ld*ArgRS, although the aminoacylation pattern was similar to that of the full-length protein at acidic pH, it showed a good percentage of activity even at basic pH. A similar pattern was observed for both proteins when the temperature was varied (Figure 14C), wherein the initial activity curve was comparable until both reached their highest capacities at 40°C. However, ΔIns-*Ld*ArgRS remained comparatively more active than *Ld*ArgRS even at higher temperatures (50-80°C), while the aminoacylation capability of *Ld*ArgRS decreased to almost 20%. Additionally, the effect of various metal ions on the aminoacylation by purified proteins was investigated. The reactions devoid of divalent ions showed much lesser enzymatic activity in comparison to the ones lacking monovalent ions. While manganese, magnesium, and calcium were most efficient in increasing the enzyme activity of both forms of protein, divalent metals such as cadmium, iron, zinc, and copper could not alleviate activity to a great extent (Figure 14D and E). Among monovalent metals, although the highest activity was noticed in the presence of potassium, other ions (Na^+, Li^+, Cs^+) could also activate *Ld*ArgRS to attain more than 50% of its activity (Figure 14F). The monovalent metal lithium, however, seemed to be mildly activating ΔIns-*Ld*ArgRS beyond its basal level (Figure 14G).

Table 3: Kinetic parameters of ligands for *Ld*ArgRS, ΔIns-*Ld*ArgRS, and *Hs*ArgRS

Protein	Ligand	K_m (μM)	V_{max} (μM/ min)	k_{cat} (μM^{-1})	k_{cat}/K_m ($min^{-1}\mu M^{-1}$)
0.25 μM *Ld*ArgRS	L-Arg	225.8±44	4±0.35	16	0.07
2 μM *Ld*ArgRS	L-Arg	197±20	5.6±0.3	2.8	0.01
0.25 μM ΔIns-*Ld*ArgRS	L-Arg	376.1±17	1.49±0.09	5.96	0.015
2 μM ΔIns-*Ld*ArgRS	L-Arg	249.6±31	2.9±0.3	1.45	0.005
0.25 μM *Ld*ArgRS	ATP	4.5±0.75	2.23±0.1	8.91	1.98
2 μM *Ld*ArgRS	ATP	1.09±0.2	6.29±0.09	3.14	2.88
0.25 μM ΔIns-*Ld*ArgRS	ATP	25.4±4	0.68±0.08	2.72	0.1
2 μM ΔIns-*Ld*ArgRS	ATP	18.4±3.5	3.9±0.8	1.95	0.1
0.25 μM *Ld*ArgRS	L-Can	203.4±25	13.52±0.75	54.08	0.26
0.25 μM ΔIns-*Ld*ArgRS	L-Can	408.0±48	4.078±0.2	16	0.04

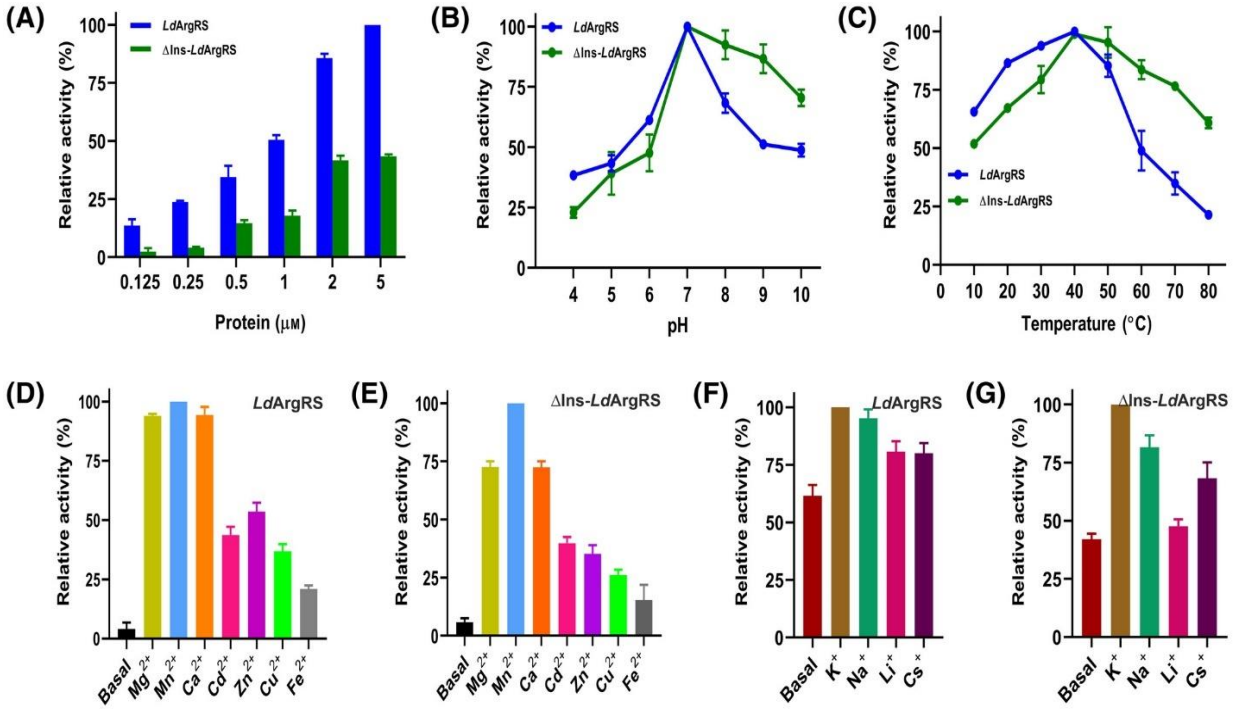

Figure 14: Aminoacylation by *Ld*ArgRS and ΔIns-*Ld*ArgRS. (A) Aminoacylation of L-Arg at different protein concentrations; Effect of (B) pH, (C) temperature, (D and E) divalent metals, (F and G) monovalent metals on the enzymatic activity of purified proteins.

Next, in order to understand the differences in their catalytic properties concerning ATP and L-Arg, we performed enzyme kinetics at different concentrations of the proteins. When the kinetics were conducted with ATP as a function at 0.25 µM protein, K_m of *Ld*ArgRS and ΔIns-*Ld*ArgRS were found to be 4.5±0.75 and 25.4±6 µM, respectively (Figure 15A). Similarly, for L-Arg, the corresponding K_m of *Ld*ArgRS and ΔIns-*Ld*ArgRS was observed to be 225.8±44 and 376.1±17 µM (Figure 15C). The K_m values decreased at 2 µM for both proteins, with an increase in their V_{max} values indicating the impact of protein concentration on various kinetic parameters. It was observed that the ligand binding propensity of *Ld*ArgRS was always greater than that of ΔIns-*Ld*ArgRS, which was reflected by their K_m and k_{cat}/K_m values (Figure 15B and D). The pseudo-substrate L-Can increased the V_{max} of *Ld*ArgRS and ΔIns-*Ld*ArgRS by almost 3.5 and 2.5 folds, respectively, while a major effect on their K_m was not observed (Figure 15E). However, the pseudo-substrate could efficiently increase the k_{cat}/K_m values for both proteins (Figure 15F).

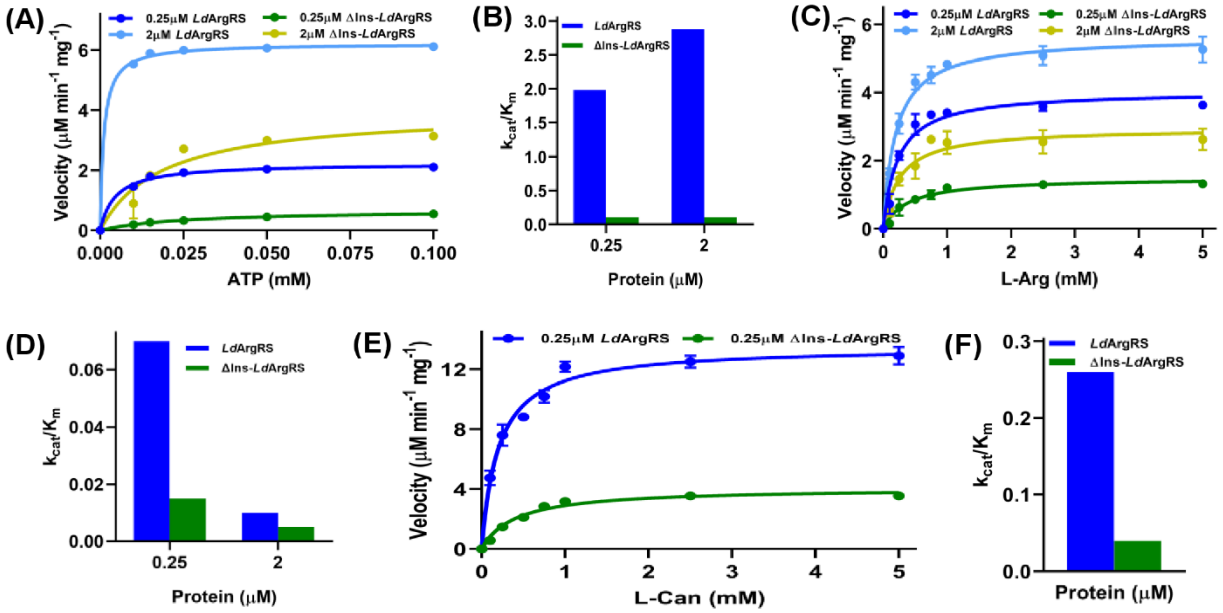

Figure 15: Catalytic efficiencies of *Ld*ArgRS and ΔIns-*Ld*ArgRS. Enzyme kinetics of purified proteins at 0.25 and 2 µM concentration for (A) ATP, (C) L-Arg, and (E) L-Can, whereas respective k_{cat}/K_m values are depicted in (B), (D), and (F).

4.1.2. Mutation of ATP-binding residues reduces catalytic efficiency of *Ld*HisRS

The aminoacylation by *Ld*HisRS was investigated under various conditions as the suitable parameters are unknown. While it showed maximal enzymatic activity at pH 7, there was a gradual

decrease in aminoacylation on either side of this pH (Figure 16A). Similarly, its lowest activity was noticed at 10°C, followed by increase till 40°C after which it decreased (Figure 16B). The aminoacylation of *Ld*HisRS was correspondingly highest and least in the presence of magnesium and iron (Figure 16C). The activity of *Ld*HisRS with calcium and zinc was similar, while copper and iron could not enhance after 23% and 18%, respectively. Likewise, the best enhancer of aminoacylation by *Ld*HisRS was perceived to be potassium, then sodium, lithium, and cesium (Figure 16E). Interestingly, *Ld*HisRS showed 23% activity when there were no monovalent metals, as compared to 5% when the reaction was devoid of divalent metals. Furthermore, the ideal magnesium and potassium concentration was found to be 15 mM (Figure 16D and F). The K_m of ATP and L-His was calculated to be 44.1±1 (Figure 16G), and 0.7±0.1 µM (Figure 16H), respectively (Table 4), suggesting the greater affinity of *Ld*HisRS towards L-His than ATP. The enzyme kinetics of mutants (E157A and R164A) in terms of ATP delineated a correspondingly increased K_m i.e., 67.9±1 and 100.4±3.5 µM depicting the relevance of E157 and R164 in ATP binding (Figure 16I). Besides the k_{cat}/K_m (catalytic efficiency) of E157A and R164A reduced by nearly 22% i.e., 1.73 and 1.72, respectively (Figure 16J).

Table 4: Enzyme kinetics of *Ld*HisRS and its mutants

Protein	Ligand	K_m (µM)	V_{max} (µM/min)	k_{cat}(s^{-1})	k_{cat}/K_m(s^{-1} μM^{-1})
*Ld*HisRS	L-His	0.7±0.1	63.5±8.3	105.8	151.14
*Ld*HisRS	ATP	44.1±1	58.6±1.5	97.6	2.2
*Ld*HisRS-E157A	ATP	67.9±1	70.7±0.2	117.8	1.73
*Ld*HisRS-R164A	ATP	100.4±3.5	103.8±0.7	173	1.72

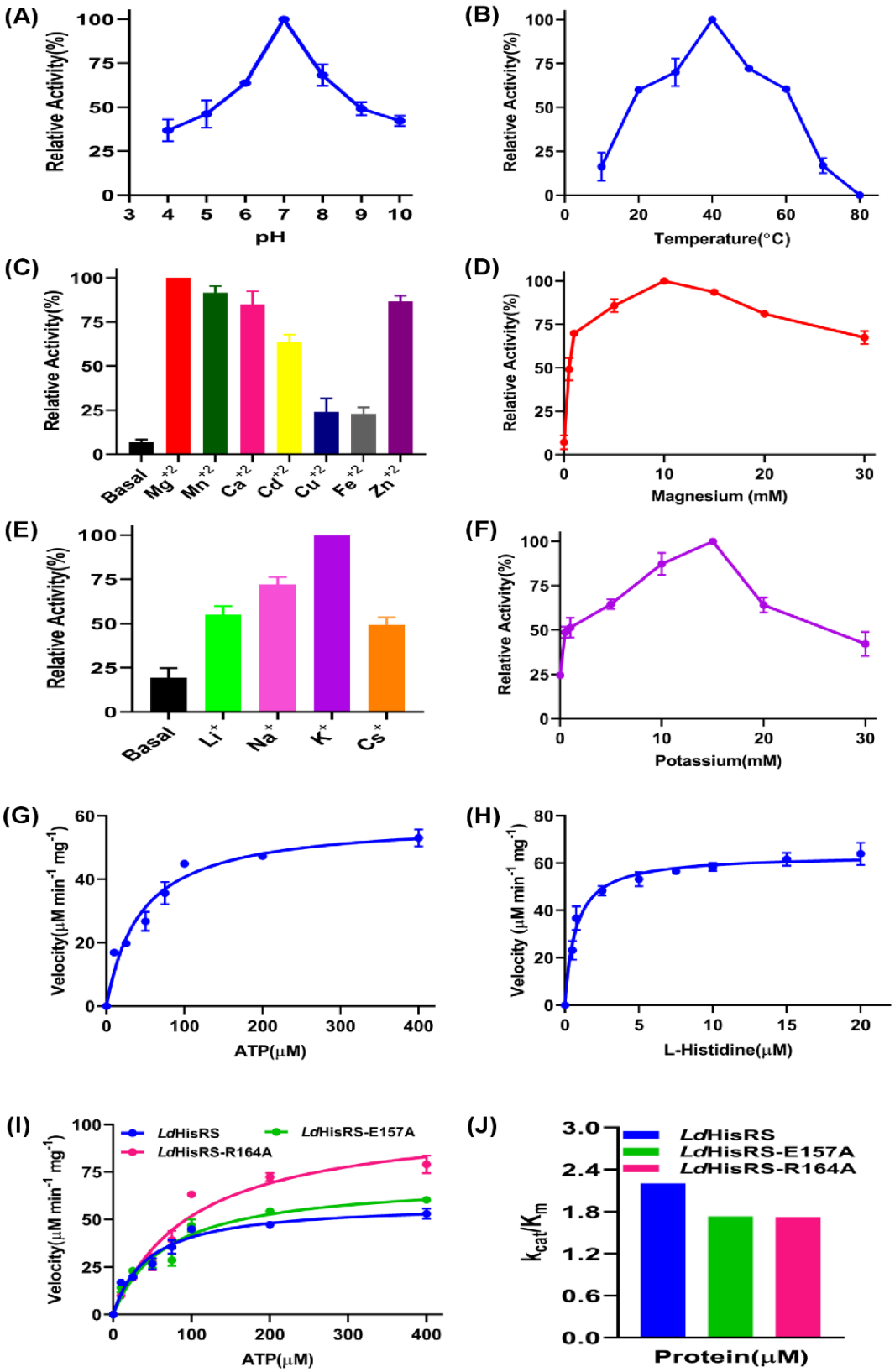

Figure 16: Enzyme kinetics of *Ld*HisRS and its mutants. Aminoacylation by *Ld*HisRS at various (A)

pH, (B) temperature, (C) divalent, and (E) monovalent metals; Optimum concentration of (D) magnesium, and (F) potassium for *Ld*HisRS; Kinetics of *Ld*HisRS with (G) ATP, (H) L-His, and (I) mutants with ATP; (J) Catalytic efficiency of purified proteins.

4.1.3. Trypanosomatid-specific insertion is a tRNA binding domain in *Ld*ArgRS

To understand the role of trypanosomatid-specific insertion in binding of tRNA, the enzyme kinetics of *Ld*ArgRS, ΔIns-*Ld*ArgRS, and *Hs*ArgRS were performed with Baker's yeast total tRNA (ytRNA) as a function. Since, ArgRSs are known to be catalytically active in the presence of $tRNA^{Arg}$, the aminoacylation reaction was supplemented with ytRNA in order to compare the tRNA dependency of *Ld*ArgRS, ΔIns-*Ld*ArgRS, and *Hs*ArgRS (Figure 17A). While the V_{max} was mostly similar for *Hs*ArgRS, *Ld*ArgRS, and ΔIns-*Ld*ArgRS, their affinity towards tRNA varied greatly. The K_m of ΔIns-*Ld*ArgRS towards tRNA increased by almost two and three times (21.4±3 µM) than that of *Ld*ArgRS (10.83±2.7 µM) and *Hs*ArgRS (7.8±0.4 µM), respectively (Table 5). Hence, it resulted in a proportional reduction of its k_{cat}/K_m value, i.e., by 2.5 and 4 folds compared to the catalytic efficiency of *Ld*ArgRS and *Hs*ArgRS, respectively. The MST (MicroScale Thermophoresis) analyses revealed that while tRNA could bind *Ld*ArgRS with a K_d of 1.2±0.2 µM (Figure 17B), no binding could be detected toward ΔIns-*Ld*ArgRS (Figure 17C). The tRNA binding capabilities of *Ld*ArgRS and ΔIns-*Ld*ArgRS were also validated through RNA-EMSA (Electrophoretic Mobility Shift Assay) (Figure 17D and E). In the case of the full-length protein, an upward shift in the protein-tRNA complex and a decrease in free tRNA were observed as the protein concentration increased. On the other hand, neither the tRNA-bound form could be detected nor a decrease in free tRNA was observed for ΔIns-*Ld*ArgRS, suggesting that the removal of insertion leads to a lowering of tRNA binding affinity in *Ld*ArgRS.

Table 5: Catalytic efficiencies of *Ld*ArgRS, ΔIns-*Ld*ArgRS, and *Hs*ArgRS with ytRNA

Protein	K_m (µM)	V_{max} (µM/ min)	k_{cat} (μM^{-1})	k_{cat}/K_m ($min^{-1}\mu M^{-1}$)
0.25 µM *Ld*ArgRS	10.83±2.7	2.73±0.16	10.92	1
0.25 µM ΔIns-*Ld*ArgRS	21.4±3	2.22±0.1	8.88	0.4
0.25 µM *Hs*ArgRS	7.8±0.4	3.4±0.7	13.6	1.74

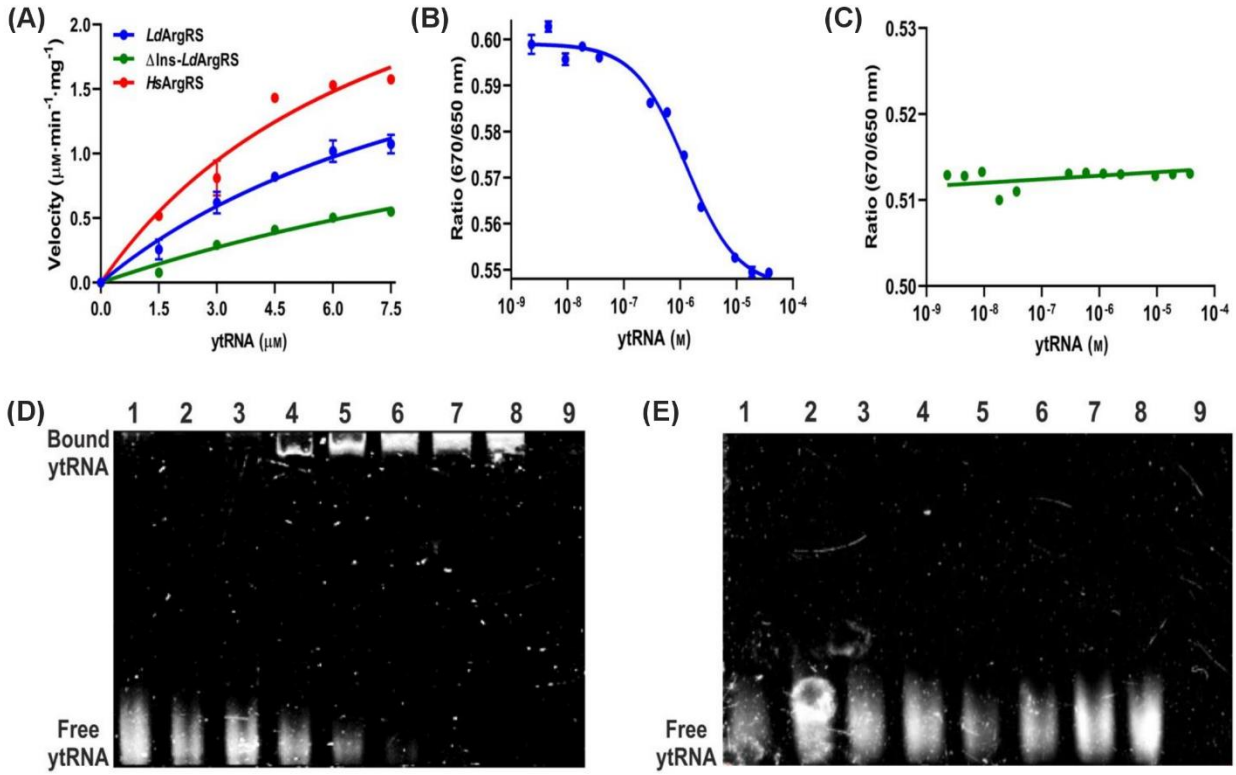

Figure 17: Kinetics of *Ld*ArgRS, ΔIns-*Ld*ArgRS, and *Hs*ArgRS with ytRNA; Data are represented as mean ± SD from duplicates of two individual experiments; (A) Kinetics of *Ld*ArgRS, ΔIns-*Ld*ArgRS, and *Hs*ArgRS with ytRNA; Spectral shift dose–response curves for ytRNA towards (B) *Ld*ArgRS, and (C) ΔIns-*Ld*ArgRS; 6% non-denaturing PAGE gel exhibiting RNA-EMSA for (D) *Ld*ArgRS, and (E) ΔIns-*Ld*ArgRS, lane 1 of gels represents only ytRNA (70 ng), lanes 2, 3, 4, 5, 6, 7, and 8 contain 70 ng ytRNA along with recombinant proteins (*Ld*ArgRS or ΔIns-*Ld*ArgRS) at 50, 100, 250, 500, 1000, 2000, and 4000 nM concentrations, respectively. Lane 9 of the gels represents results obtained with only recombinant protein present (4000 nM).

4.1.4. Benzothiazolo-coumarin derivatives are potent inhibitors of *Ld*ArgRS and *Ld*HisRS

In a quest to find novel and potent inhibitors of *Ld*ArgRS, 14 benzothiazolo-coumarin derivatives (7a to n) were synthesized by our collaborators from NIPER, Hyderabad, and screened through aminoacylation assays to evaluate their potency to inhibit leishmanial as well as human ArgRS (Figure 18). The general structure of these compounds except Comp-7h, 7l, and 7n consisted of three benzene rings, in which the first benzene ring is placed adjacent to a pentene ring such that they mimic the structure of adenine, the second benzene ring is attached to a cyclohexanone molecule, and the third benzene ring is substituted by methyl or halogen groups at various ortho,

meta, and para positions. The Comp-7h, 7l, and 7n, on the other hand, lacked the third benzene ring.

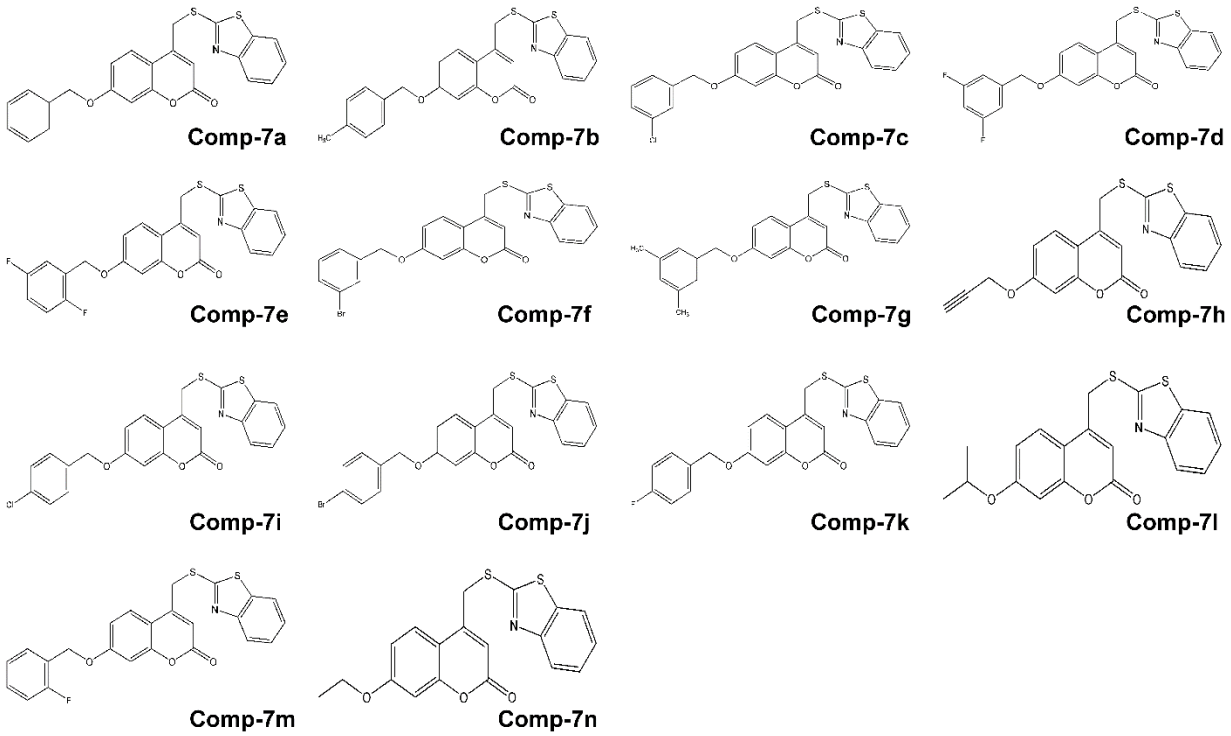

Figure 18: Chemical structure of synthesized benzothiazolo-coumarin derivatives. A series of benzothiazolo-coumarin derivatives were made from combination of aryl and alkyl halides with coumarin by substituting at the 7-hydroxy group.

From the values enlisted in Table 6, it can be deduced that substitution with a halogen group at the para position or a methyl group in the ortho and meta positions of the third benzene ring is necessary for better inhibition of *Ld*ArgRS. On the contrary, substitutions by fluorine at the ortho and meta positions of the third benzene ring were the most ineffective in enhancing the potency of inhibitors as observed for Comp-7d and 7e. Comp-7g and 7j were better at inhibiting *Ld*ArgRS when compared to other compounds in the series, as their IC_{50} values were computed to be 0.7 and 1.2 µM, respectively (Table 6, Figure 19A and B). Moreover, these two compounds showed greater selectivity towards *Ld*ArgRS than *Hs*ArgRS, as a 30 and 16 fold differences in IC_{50} was observed. The mode of inhibition was also determined for these two compounds with respect to L-Arg and ATP. The inhibitor Comp-7g inhibited *Ld*ArgRS mixed-competitively (Figure 19C) and non-competitively (Figure 19E) with respect to ATP and L-Arg, respectively, while Comp-7j was

found to be competitive for ATP (Figure 19D), and it showed a non-competitive mode of inhibition towards L-Arg similar to Comp-7g (Figure 19F). Hence, Comp-7j was considered a better inhibitor of *Ld*ArgRS than Comp-7g. When the inhibition was evaluated for Comp-7j towards ΔIns-*Ld*ArgRS, the IC_{50} increased to 9 µM (Figure 19G), and the mode of inhibition changed from competitive to mixed-competitive towards ATP (Figure 19H). These results further suggest the impact of trypanosomatid-specific insertion in altering the modality of inhibition.

Table 6: IC_{50} (µM) of benzothiazolo-coumarin derivatives towards *Ld*ArgRS and *Hs*ArgRS

Compound	*Ld*ArgRS	*Hs*ArgRS
7a	4.2±1	20.4±1.5
7b	3.4±0.6	9.9±1.2
7c	2.9±0.4	7.5±0.6
7d	9.1±0.8	10±0.5
7e	7.6±0.7	7.8±0.9
7f	4.3±0.3	7.2±0.4
7g	0.7±0.1	21.1±2
7h	3.2±0.4	19.2±2.5
7i	2.0±0.2	14.9±1.4
7j	1.2±0.1	19±1
7k	2.2±0.3	10.5±1.5
7l	3.4±0.2	7.4±0.5
7m	5.1±0.5	9.3±1
7n	6.2±0.7	8.6±0.5

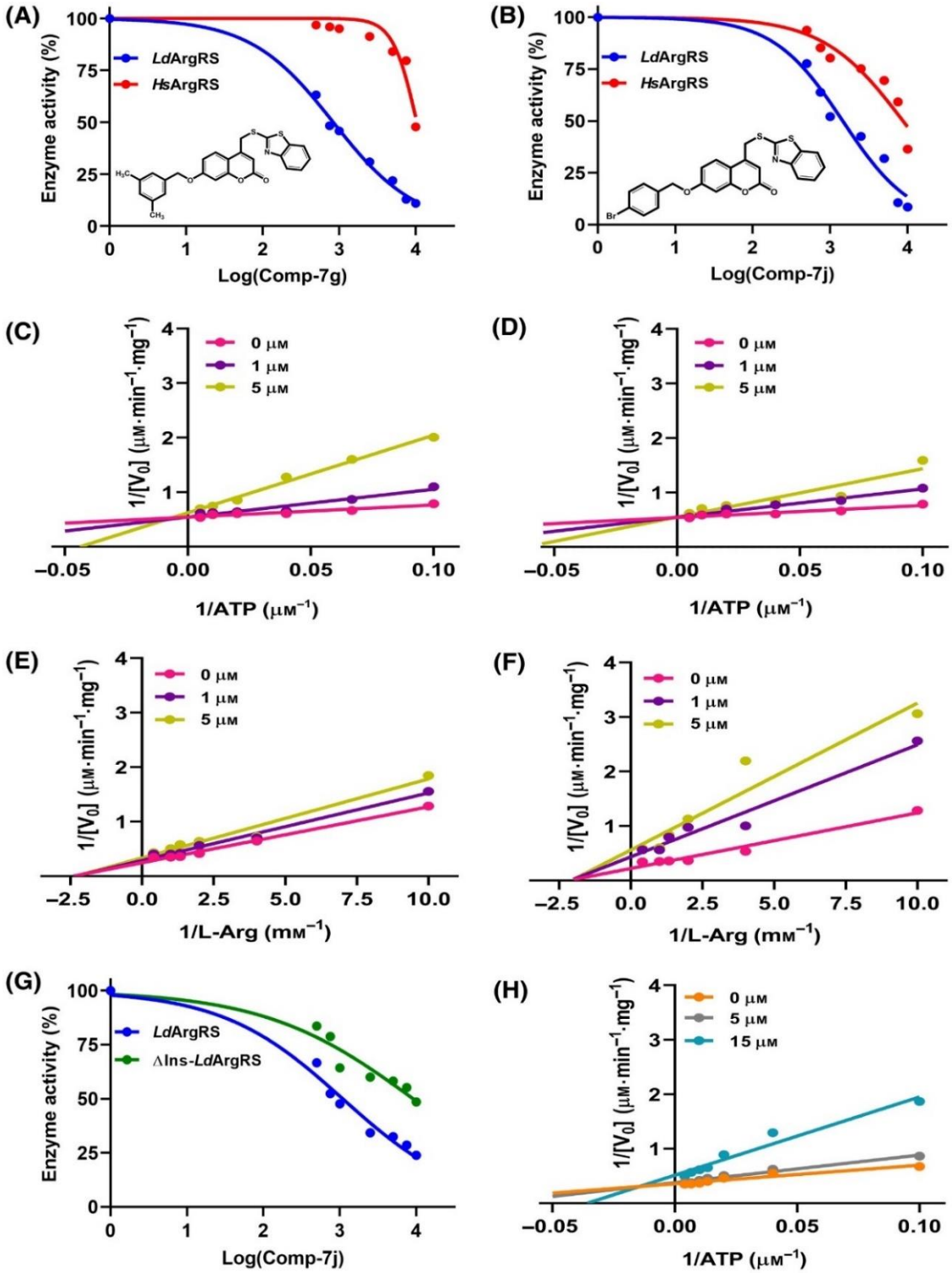

Figure 19: Inhibitory effect of Comp-7g and 7j on purified ArgRSs. Percentage reduction of *Ld*ArgRS and *Hs*ArgRS activity in the presence of (A) Comp-7g, and (B) Comp-7j; Mode of inhibition for (C) Comp-7g, and (D) 7j towards ATP; (E) Comp-7g, and (F) 7j depicting non-competitive mode of action with respect to L-Arg; (G) Comparative inhibition of purified enzymes with Comp-7j; (H) Mixed-competitive type

inhibition of ΔIns-*Ld*ArgRS by Comp-7j for ATP. Each of the experiments was performed twice and the values indicate mean ± SD.

Similarly, as indicated in Table 7, the compounds possessing methyl or halogen moiety inhibited *Ld*HisRS activity better than others. Among the 14 compounds tested, Comp-7a (IC_{50} = 1.5±0.1 µM) and 7m (IC_{50} = 1.1±0.3 µM) demonstrated better inhibition in comparison to others (Figure 20A and B). It is noteworthy that their IC_{50} values towards the human HisRS were 6.1±0.1 and 10.5±1 µM, which is considerably higher than *Ld*HisRS inhibition. The IC_{50} for lead inhibitors were determined to be 4.5±0.7 (Comp-7a) and 6.3±0.8 µM (Comp-7m) for E157A, while the respective values for R164A were 8.3±1 and 8.8±0.9 µM. The mode of inhibition was also determined towards protein along with their (K_i) slope and ($K_{i\alpha}$) intercept inhibition constants. Comp-7a was found to be uncompetitive and 7m was mixed-competitive with respect to the substrate (Figure 20D and F) and their corresponding $K_{i\alpha}$ were 2.8±0.4 and 2.2±0.3 nM (Figure 20C and E).

Table 7: Inhibition of *Ld*HisRS and *Hs*HisRS by benzothiazolo-coumarin derivatives

Compound	*Ld*HisRS	*Hs*HisRS
7a	1.5±0.1	6.1±0.1
7b	2.5±0.05	7.3±0.1
7c	3.3±0.2	3.8±0.1
7d	3.5±0.1	6.9±0.6
7e	4.4±0.1	8.6±0.1
7f	5.6±0.5	9.9±1.5
7g	10.4±1.5	16.1±0.1
7h	4.1±0.1	15.8±2.5
7i	4.8±0.1	18±0.1
7j	3.5±0.1	7.3±0.1
7k	3.5±0.4	12.7±2
7l	5.9±0.3	4.4±0.2
7m	1.1±0.3	10.5±1
7n	2.5±0.2	9±0.4

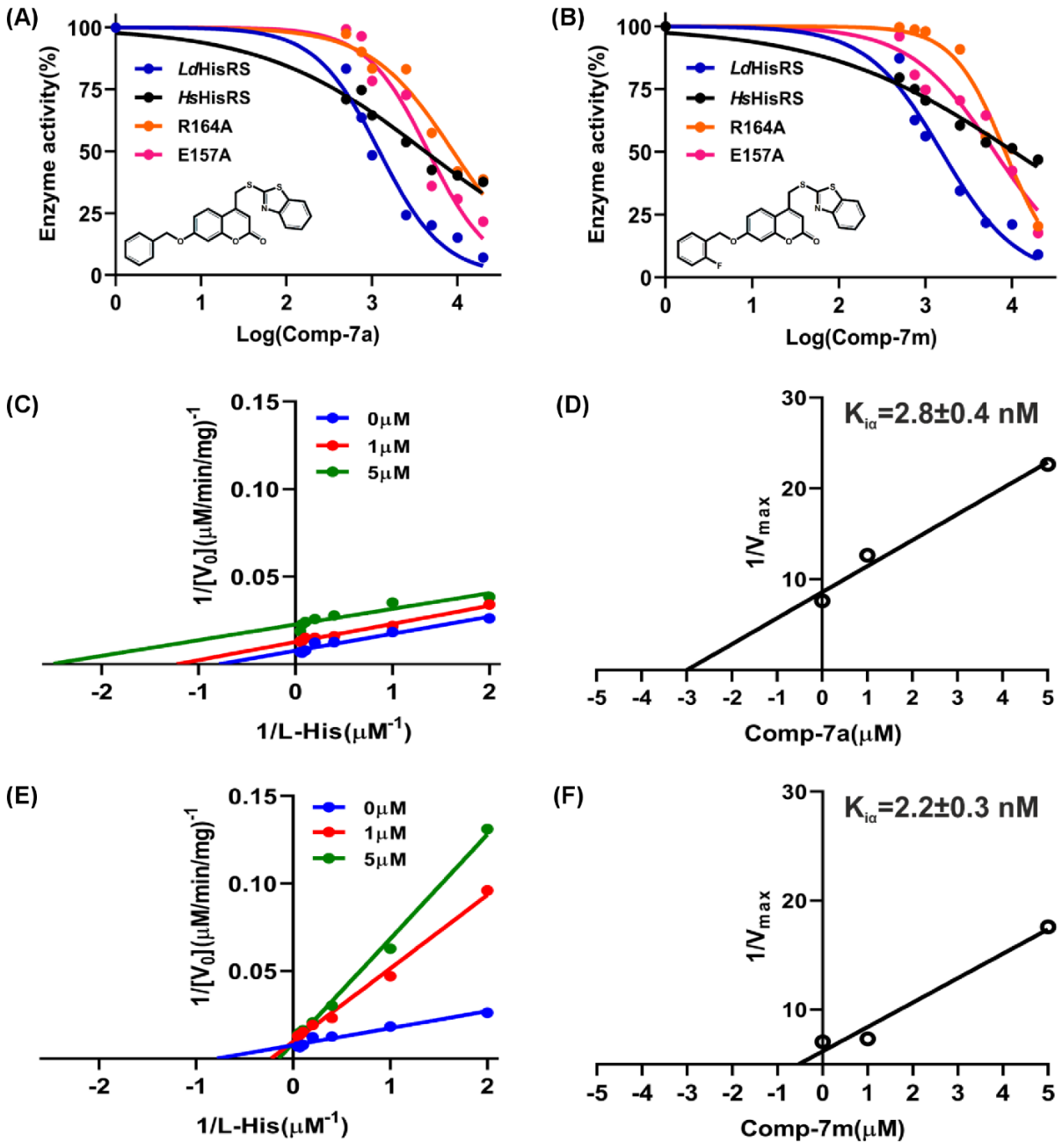

Figure 20: Inhibition of *Ld*HisRS and its mutants by Comp-7a and 7m: Reduction of *Ld*HisRS activity in the presence of (A) Comp-7a and (B) Comp-7m; Mode of inhibition with respect to L-His in presence of (C) Comp-7a, (E) Comp-7m, and their corresponding $K_{i\alpha}$ plots (D and F).

Comp-7a and 7m showed non-competitive ($K_{i\alpha}$=3.3±0.5 nM) and competitive (K_i=2.7±0.2 nM) mode of inhibition towards *Ld*HisRS with respect to ATP (Figure 21A-D). Comp-7m was considered as a better inhibitor of *Ld*HisRS than Comp-7a based on the difference in IC_{50} values

between *Ld*HisRS and *Hs*HisRS as well as mode of inhibition. With ATP as a function, Comp-7m inhibited E157A competitively (K_i=26.9±2 nM), while its mode of inhibition changed to mixed-competitive towards R164A ($K_{i\alpha}$=3.9±0.7 nM) (Figure 21E-H).

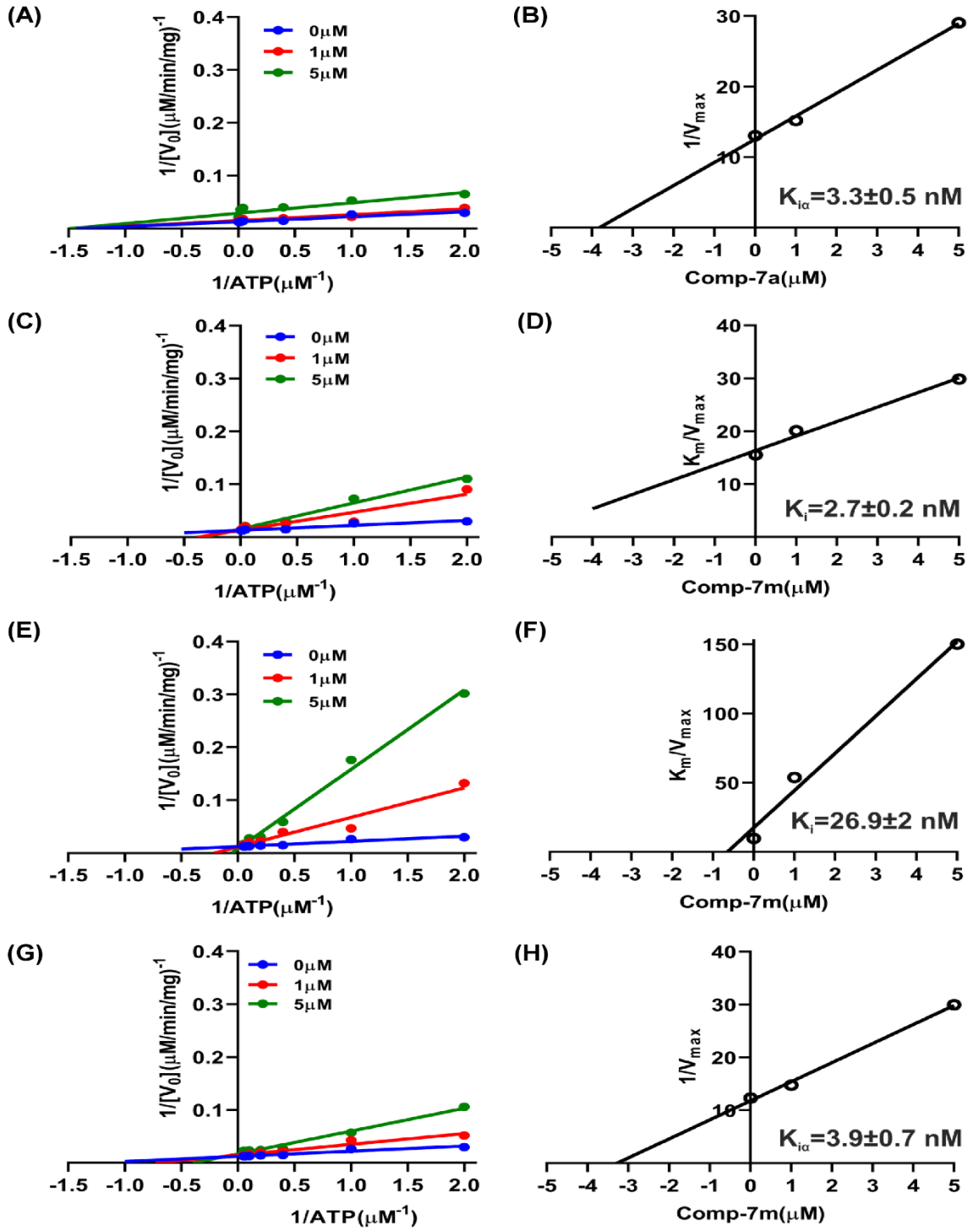

Figure 21: Inhibition mode of Comp-7m for *Ld*HisRS and its mutants towards ATP. Mode of

inhibition for *Ld*HisRS by (A) Comp-7a, (C) Comp-7m, and their respective $K_{i\alpha}$ (B) and K_i (D) plots; Inhibitory effect of Comp-7m on (E) E157A, (G) R164A with their corresponding K_i (F) and $K_{i\alpha}$ (H) plots.

4.1.5. Binding affinity of lead molecules with tRNA synthetases

The binding capacity of Comp-7j with *Ld*ArgRS, *Hs*ArgRS, and ΔIns-*Ld*ArgRS was also determined through fluorescence spectroscopy. In each case, with increasing concentrations of inhibitor, there was a decrease in the fluorescence intensities of the proteins (Figure 22A, C, and E). This decrease in intensities was exclusively due to the binding of inhibitors to proteins and not because of a change in their environments, as the λ_{max} remained same viz., λ_{max} for *Ld*ArgRS, *Hs*ArgRS, and ΔIns-*Ld*ArgRS were 337±1, 330±1, and 335±2 nm, respectively. The inhibitor was found to be more specific towards *Ld*ArgRS than *Hs*ArgRS and ΔIns-*Ld*ArgRS as their binding constant values (K_b) derived from the modified Stern-Volmer equation were found to be $9.5\pm0.3\times10^{-7}$, $6.5\pm0.4\times10^{-7}$, and $5.1\pm0.4\times10^{-7}$ M^{-1}, respectively (Figure 22B, D, and F). The effect of an extrinsic fluorophore, i.e., 8-anilinonapthalene-1-sulfonic acid (ANS), on *Ld*ArgRS was also studied by varying pH. An increase in the inhibitor concentration did not lead to protein aggregation (Figure 22G), while the protein in apo state showed minimal tendency for aggregation between pH 6 and 10 (Figure 22H).

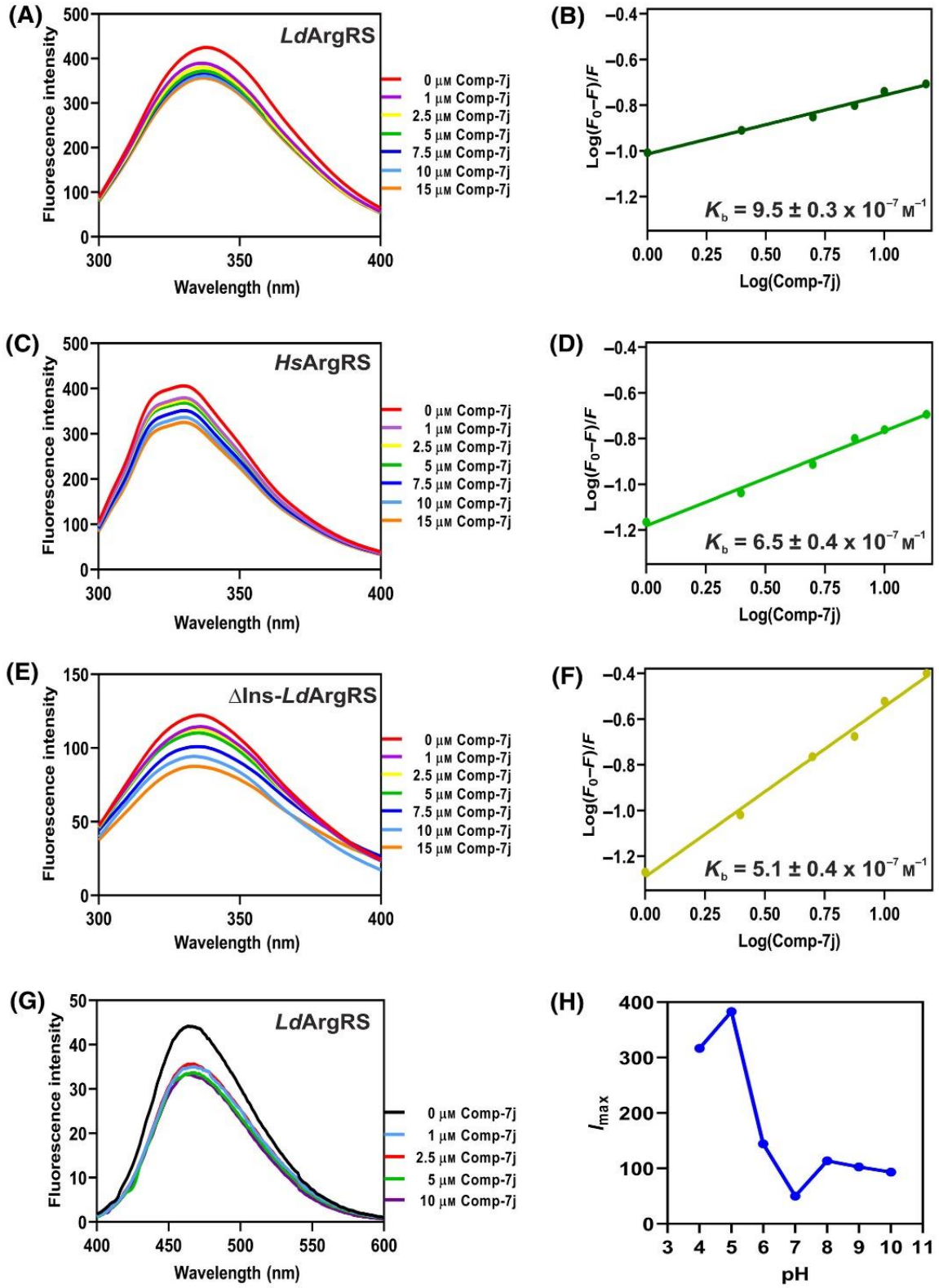

Figure 22: Fluorescence measurements of purified ArgRSs with Comp-7j. Decrease in intrinsic fluorescence intensity of (A) *Ld*ArgRS, (C) *Hs*ArgRS, and (E) ΔIns-*Ld*ArgRS with increasing

concentrations of Comp-7j; Corresponding modified Stern-Volmer plots are presented in (B), (D), and (F), respectively; (G) The binding of Comp-7j with *Ld*ArgRS in the presence of the fluorescent probe, ANS; (H) pH-dependent extrinsic fluorescence of *Ld*ArgRS. In each of the plots, values are indicative of mean ± SD with n=2. The P-value<0.0001 was calculated using one-way ANOVA.

Similarly, the binding affinity of Comp-7m towards *Ld*HisRS, its mutants, and *Hs*HisRS was also analysed. As the λ_{max} was unaltered with increase in inhibitor concentrations, the reduction of intrinsic fluorescence intensity was attributed to the binding of Comp-7m for the protein (Figure 23A, C, E, and G). Comp-7m depicted comparatively higher binding affinity towards *Ld*HisRS than its mutant forms and *Hs*HisRS. The K_b was observed to be $5.9\pm0.3\times10^{-6}$ M^{-1} for Comp-7m towards *Ld*HisRS (Figure 23B), while its corresponding K_b for E157A, R164A, and *Hs*HisRS was enumerated to be $4.3\pm0.6\times10^{-6}$, $3.3\pm0.3\times10^{-6}$, and $4.8\pm0.3\times10^{-6}$ M^{-1} (Figure 23D, F, and H).

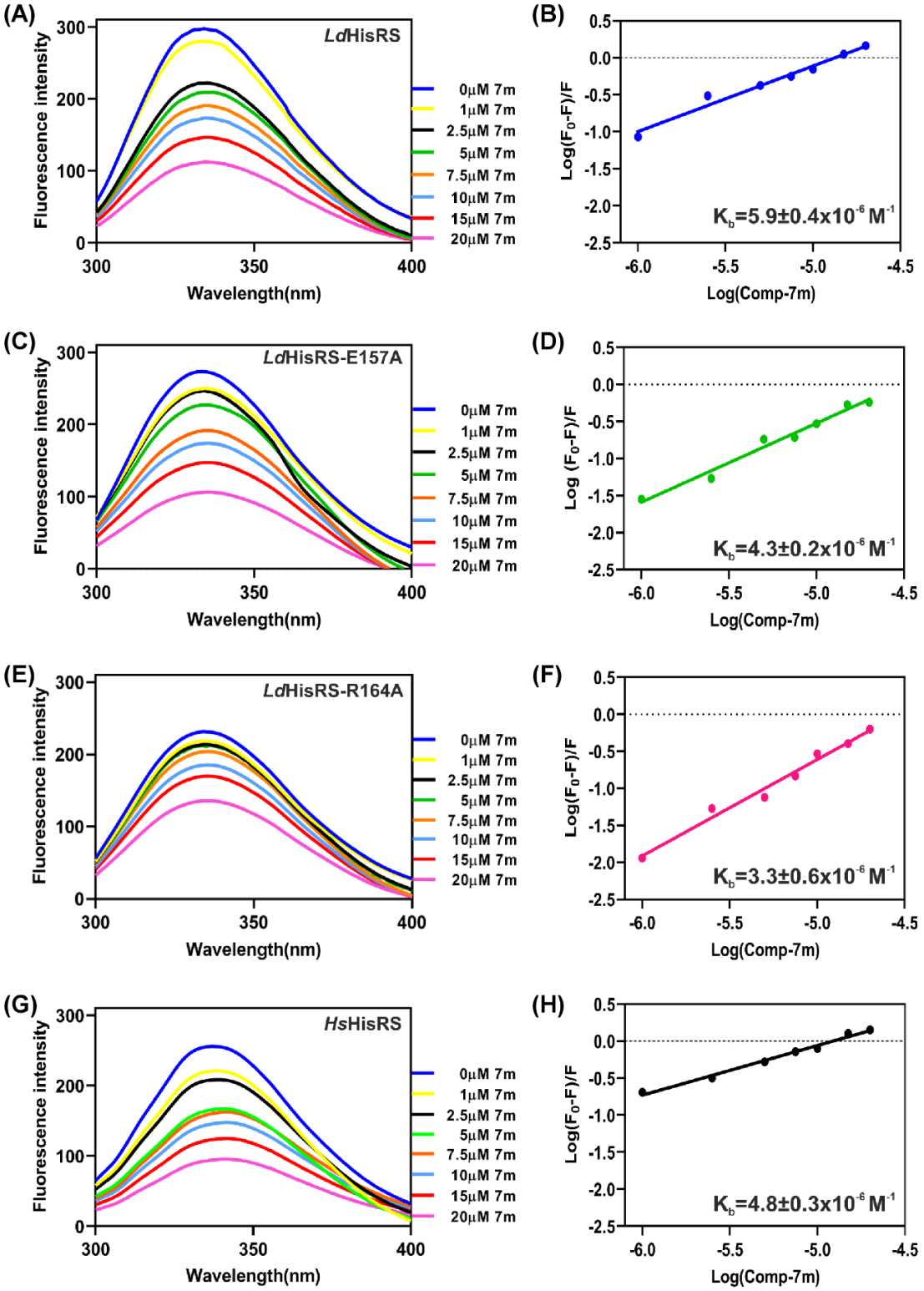

Figure 23: Binding affinity of Comp-7m towards *Ld*HisRS, its mutants, and *Hs*HisRS. Reduction in intrinsic fluorescence intensities of (A) *Ld*HisRS, (C) *Ld*HisRS-E157A, (E) *Ld*HisRS-R164A, and (G) *Hs*HisRS with their corresponding modified Stern-Volmer plots (B, D, F, and H).

4.1.6. ADME properties of lead inhibitors

The ADME properties of lead inhibitors were also computed to verify if the inhibitors comply with the acceptable range of druglikeness (Table 8). For Comp-7g and 7j, the number of H-bond acceptors and donors was below 5 as per Lipinski's rule, while the gastrointestinal absorption of Comp-7g and 7j was low and high, respectively suggesting Comp-7j has better pharmacokinetic properties than Comp-7g. Moreover, Comp-7g and 7j exhibited low cytotoxicity towards murine macrophage RAW 264.7 as their IC_{50} values were 158±10 and 210±17 µM, respectively. Likewise, the ADME characteristics for Comp-7a and Comp-7m were comparable, while their cytotoxicity was similar with Comp-7m demonstrating mildly lower IC_{50} value i.e., 180±7 µM as compared to Comp-7a with 173±5 µM.

Table 8: SwissADME properties and cytotoxicity of hit compounds

Compound	Molecular weight (g/mol)	LogP	LogS	H-bond acceptors	H-bond donors	GI absorption	Cytotoxicity (µM)
Comp-7a	431.5	3.96	-6.3	4	0	Low	173±5
Comp-7g	459.6	4.43	-6.9	4	0	Low	158±10
Comp-7j	510.4	4.55	-6.8	3	1	High	210±17
Comp-7m	449.2	4.12	-6.4	5	0	Medium	180±7

4.2. Discussion

Through RNA-EMSA, MST, and enzyme kinetics we confirmed this insertion to be an RNA binding domain. ΔIns-*Ld*ArgRS also depicted altered structural and catalytic properties compared to *Ld*ArgRS as the latter could perform aminoacylation at lower protein concentrations apart from demonstrating better catalytic efficiency. Since aminoacylation is quantified based on pyrophosphate release, it can be inferred that at lower protein concentrations, ΔIns-*Ld*ArgRS is not capable of initiating the ATP-PPi exchange reaction like other ArgRSs [80, 81]. We also synthesized ATP resembling inhibitors knowing that analogs of ATP such as cladosporin are potent inhibitors of aaRSs [82]. Of them, the ones that possessed halogen groups attached to the para position or methyl groups linked to the ortho and meta positions of the third benzene ring augmented their potency. Quinoline derivatives possessing halogen and methyl groups at the para position of their benzene rings have been evaluated as potent inhibitors of *L. donovani* methionine aminopeptidase 1 [83, 84]. Among the inhibitors, Comp-7j was found to be a competitive as well as specific inhibitor for *Ld*ArgRS. However, the removal of insertion changed its mode of inhibition adding further evidence to the insertion-based alteration of *Ld*ArgRS kinetics. Similarly, the highest activity of *Ld*HisRS was observed at pH 7 and 40°C as seen other HisRSs [34, 51, 79, 85, 86]. The protein's activity was found to decrease on either extremity of pH and temperature, while magnesium and potassium were most efficient in enhancing aminoacylation when compared to any other metal ions. The rate of aminoacylation in HisRS from *Salmonella typhimurium* was maximum at an excess of magnesium to ATP ratio [87, 88]. In *E. coli* HisRS-Mn^{+2} crystal structure, the metal binding sites were observed proximal to Arg259 [77]. It is also reported that HisRSs need only two magnesium ions for the electrophilic reaction to take place since the role of a third magnesium ion is played by an arginine residue from the active site in HisRSs [89, 90]. Minimal activity was recorded for *Ld*HisRS in the reaction devoid of divalent metals whereas there was significant enzyme activity in the absence of monovalent metals suggesting the relevance of divalent ions. This is consistent with a prior study, which found that the production of His-tRNA was only observed when the media was supplemented with magnesium [91]. It was found that the protein had a stronger affinity for L-His (substrate) than ATP (cofactor) as reported previously [87, 92, 93]. Our study also demonstrated that the catalytic effectiveness of class-II tRNA synthetases is decreased when active site residues are mutated to alanine [94]. Analogs of ATP that inhibited leishmanial ArgRS efficiently, also inhibited *Ld*HisRS [95]. The methylene group

in cladosporin is thought to be responsible for its effectiveness [96, 97], and this study found that compounds with methyl or halogen groups were more effective at inhibiting *Ld*HisRS. Alteration of the important catalytic pocket residues have provided information about how lead compounds alter the mode of *Leishmania donovani* peptidase T inhibition [98].

Chapter-III

5. To assess the structure of leishmanial proteins with or without ligands

5.1. Results

5.1.1. Removal of insertion modifies *Ld*ArgRS secondary structure

The deviations in the secondary structural content of *Ld*ArgRS and ΔIns-*Ld*ArgRS were also studied upon binding with ligands such as ATP and L-Arg. ΔIns-*Ld*ArgRS was found to contain slightly more α-helices (32%) than *Ld*ArgRS (30%) in its apo state, while the percentage of β-sheets remained the same (14%) (Figure 24A and C). The corresponding T_m for *Ld*ArgRS and ΔIns-*Ld*ArgRS were found to be 39.8±0.3 and 41.1±1°C (Figure 24B and D, Table 9). Upon ATP binding, the α-helical content increased to 33% for ΔIns-*Ld*ArgRS while for *Ld*ArgRS no change was seen in α-helices (30%) with slight increase (16%) in the β-sheets for both proteins. The increase in α-helices resulted a T_m of i.e., 42.8°C for ΔIns-*Ld*ArgRS in the presence of ATP, and the T_m of *Ld*ArgRS was found to be 41.6±0.4°C. The higher melting point as well as α-helical content suggests that binding of ATP to ΔIns-*Ld*ArgRS promotes protein folding, thereby stabilizing the protein-ATP complex. Conversely, ΔIns-*Ld*ArgRS-L-Arg complex formation led to the increase in β-sheets (43%). These changes led to an increase in T_m of ΔIns-*Ld*ArgRS by 4°C, while the same was not noticed for *Ld*ArgRS. These results indicate the influence of trypanosomatid-specific insertion in ligand binding.

Table 9: Secondary structural content of *Ld*ArgRS and ΔIns-*Ld*ArgRS with ligands

Protein	α-helices (%)	β-sheets (%)	Random coils (%)	T_m (°C)
*Ld*ArgRS	30	14	56	39.8±0.3
*Ld*ArgRS+ATP	30	16	54	41.6±0.4
*Ld*ArgRS+L-Arg	30	15	55	40.8±0.8
ΔIns-*Ld*ArgRS	32	14	54	41.1±1.0
ΔIns-*Ld*ArgRS+ATP	33	16	51	42.8±0.6
ΔIns-*Ld*ArgRS+L-Arg	3	50	47	44.5±0.3

*Ld*ArgRS maintained a higher α-helical content than β-sheets at all pH conditions, despite showing greater overall secondary structural content from pH 7 onwards (Figure 24E, Table 10). However, in ΔIns-*Ld*ArgRS, at lower pH (4 to 6), the α-helical content was lesser as compared to β-sheets which increased from pH 7 onwards with a decrement of β-sheets content (Figure 24F). Furthermore, chemical denaturation of the proteins was also studied in the presence of denaturants

such as urea (Figure 24G) and guanidine hydrochloride (GdHCl) (Figure 24H). The structural stability of both proteins was susceptible to lower concentrations of GdHCl than urea, as evident from the C_m values viz., 1.72±0.2 and 2.2±0.5 M for *Ld*ArgRS, and the respective values of 2.49±0.25 and 2.98±0.6 M for ΔIns-*Ld*ArgRS. From these values, it may be inferred that ΔIns-*Ld*ArgRS needed a higher concentration of denaturants to undergo chemical denaturation than the full-length form.

Table 10: Secondary structural elements of *Ld*ArgRS and ΔIns-*Ld*ArgRS upon pH variation

		pH 4	**pH 5**	**pH 6**	**pH 7**	**pH 8**	**pH 9**	**pH 10**
α-helices	*Ld*ArgRS	25%	27%	30%	30%	32%	28%	28%
	ΔIns-*Ld*ArgRS	9%	13%	18%	32%	31%	31%	31%
β-sheets	*Ld*ArgRS	15%	15%	13%	14%	18%	18%	19%
	ΔIns-*Ld*ArgRS	43%	39%	40%	14%	11%	15%	12%
Random coils	*Ld*ArgRS	60%	58%	57%	56%	50%	54%	53%
	ΔIns-*Ld*ArgRS	48%	48%	42%	54%	58%	54%	57%

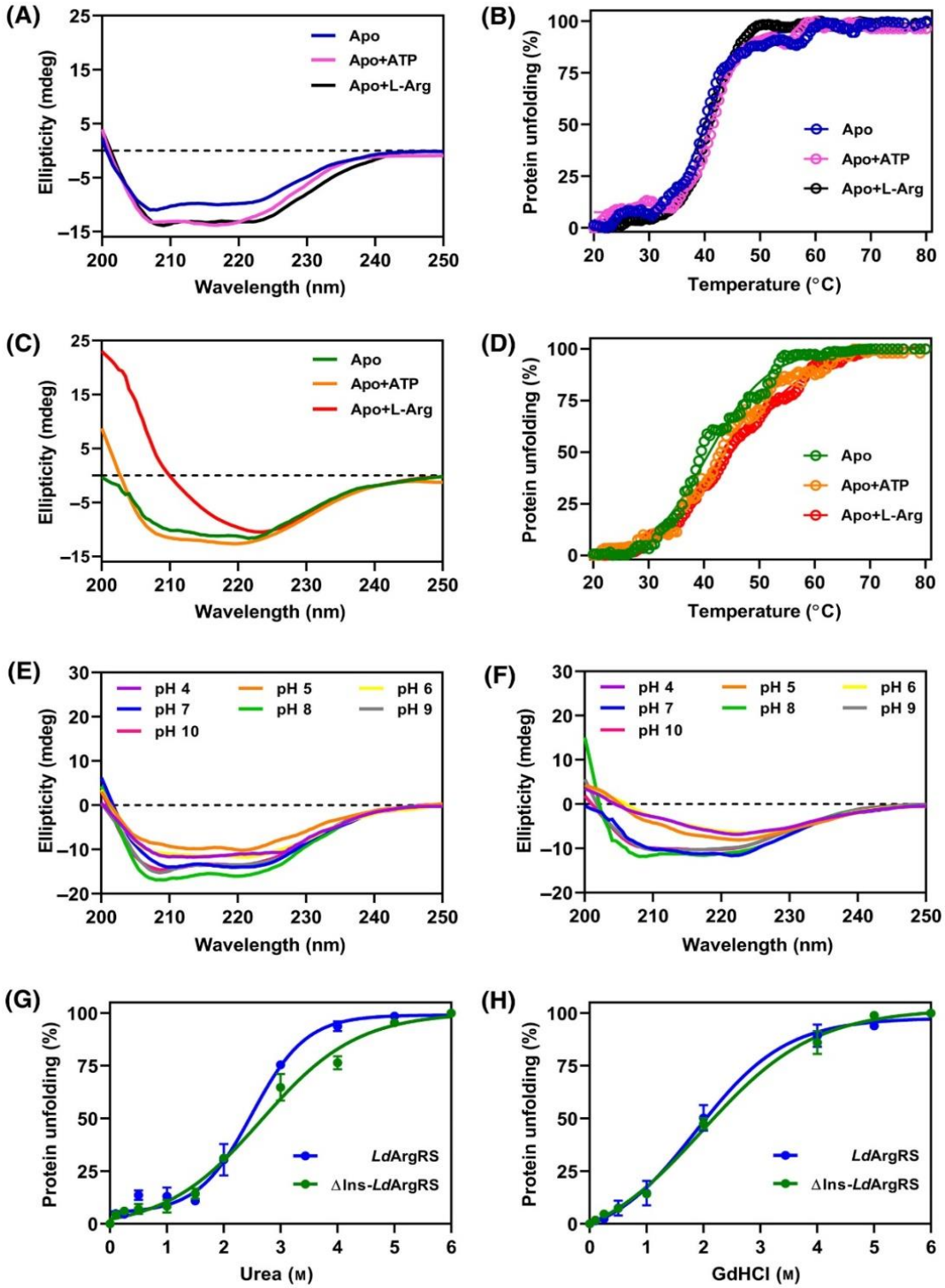

Figure 24: Secondary structural analysis of *Ld*ArgRS and ΔIns-*Ld*ArgRS. CD spectra and thermal-melt curves of (A-B) *Ld*ArgRS, and (C-D) ΔIns-*Ld*ArgRS with and without ligands; Changes in secondary structural content upon pH variation for (E) *Ld*ArgRS, and (F) ΔIns-*Ld*ArgRS; Effect of urea (G) and GdHCl (H) on structural stability of purified proteins.

5.1.2. The stability of *Ld*HisRS is enhanced upon binding of ligands

The secondary structure of *Ld*HisRS varied greatly in the absence or presence of ATP or L-His (Figure 25A). The apo form composed of 45, 10, and 45% of alpha-helices, β-sheets, and random coils, respectively (Table 11). In the case of *Ld*HisRS-ATP bound complex, an increase in the β-sheets was observed by 6% while its melting temperature enhanced (Figure 25B). Likewise, the binding of L-His augmented T_m that was found to be 53.5±0.5°C. In the presence of both ATP and L-His, a conversion of alpha-helices into β-sheets was noticed i.e., 39% alpha-helices and 38% β-sheets, indicating the equal contribution alpha-helices and β-sheets towards the binding of L-His and ATP.

Table 11: Secondary structural contents of *Ld*HisRS and its ligand-bound forms

Protein	α-helices (%)	β-sheets (%)	Random coils (%)	T_m (°C)
*Ld*HisRS	45	10	45	42.2±1
*Ld*HisRS+ATP	43	16	42	53.9±0.8
*Ld*HisRS+L-His	43	15	32	53.5±0.5
*Ld*HisRS+L-His+ATP	39	38	23	59.3±1.5

The substitution of E157 and R164 residues by alanine led to the increase of β-sheets by 13% and 17%, correspondingly (Figure 25C, Table 12). As a result, there was a subsequent enhancement of the secondary structures in mutated forms i.e., E157A (68%) and R164A (70%) in comparison to the native protein (55%). Consequently, there was a shift in the T_m by approximately 10°C and 13°C, respectively (Figure 25D). Employing guanidine hydrochloride (GdHCl) and urea, the chemical denaturation of *Ld*HisRS was investigated (Figure 25E). With lesser concentrations of GdHCl, *Ld*HisRS destabilized easily as compared to urea. The C_m was found to be 1.3±0.15 and 2.5±0.3 M for GdHCl and urea, respectively, suggesting that the protein is susceptible to early destabilization with GdHCl.

Table 12: Secondary structural features of *Ld*HisRS and its mutants

Protein	α-helices (%)	β-sheets (%)	Random coils (%)	T_m (°C)
*Ld*HisRS	45	10	45	41.9±1
*Ld*HisRS-E157A	45	23	32	51.3±2
*Ld*HisRS-R164A	43	27	30	54±1.7

Likewise, the variation in *Ld*HisRS folding was observed at different pH (Table 13), wherein at acidic pH i.e., 4 and 5, fewer secondary structural content was recorded (Figure 25F). Near the isoelectric point i.e., pH 6, the lowest percentage of alpha-helices was noticed with a gradual increase in the secondary structure with pH 7 and above.

Table 13: Secondary structural elements of *Ld*HisRS upon varying pH

pH	4	5	6	7	8	9	10
α-helices (%)	27	2	10	45	55	61	58
β-sheets (%)	15	51	41	10	10	7	10
Random coils (%)	58	47	49	45	35	32	32

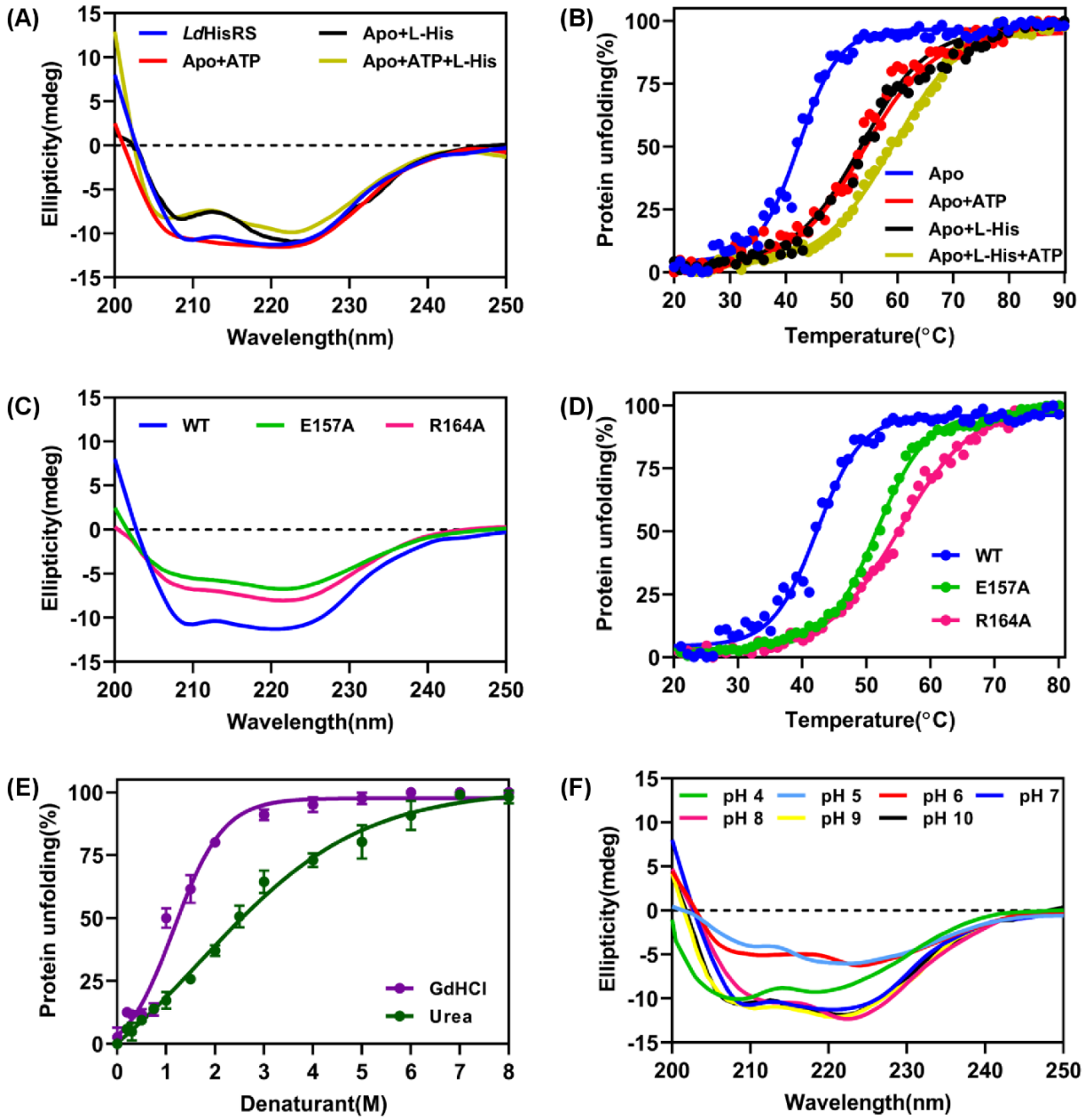

Figure 25: Secondary structural elements of *Ld*HisRS and its mutants. (A) Far-UV CD spectra of *Ld*HisRS in complex with its cognate ligands, (C) *Ld*HisRS and its mutants, and (B and D) their corresponding thermal stabilities; (E) Chemical denaturation of the purified *Ld*HisRS in the presence of urea and GdHCl; (F) Spectra of *Ld*HisRS at various pH.

5.1.3. *Ld*ArgRS contains a shorter Rossmann fold unlike other ArgRSs

The structure of *Ld*ArgRS was downloaded from the AlphaFold database and from the Ramachandran plot; it was found that 0.3% of residues were in the disallowed region. Hence, the

structure was further refined through Modloop server that brought 0% residues to disallowed region, 93.9% residues in mostly favored, 5.9% residues in additionally allowed, and 0.2% residues in generously allowed regions with an ERRAT score of 99.4. The domain arrangement was predicted by comparing the structure with that of *Pf*ArgRS (PDB ID: 5JLD). The overall structure of *Ld*ArgRS could be divided into three main domains: the N-terminal (1–119), catalytic (120–293; 406–590), and C-terminal domain (591-692). Apart from these domains, the trypanosomatid-specific insertion consisting predominantly of α-helices was positioned from 294 to 405 residues. The Rossmann fold containing L-Arg and ATP binding motifs comprised of four antiparallel β-strands instead of five, as previously observed in other ArgRS [62]. A structural comparison of *Ld*ArgRS with other arginyl-tRNA synthetase from either human (PDB ID: 4Q2T) or yeast (PDB ID: 1F7V) revealed the presence of a loop in the place of the fifth β-strand and all of these strands were shorter in length. The HVGH and KKIKT motifs are situated on either side of the insertion.

5.1.4. $tRNA^{Arg}$ induces rigidity in trypanosomatid-specific insertion

Since the trypanosomatid-specific insertion was found to help in the binding of tRNA and there is no available structure of leishmanial arginyl-tRNA synthetase in complex with $tRNA^{Arg}$, the structure of leishmanial $tRNA^{Arg}$ was generated, and then docked with the leishmanial enzyme to put forward a possible arrangement of the protein-nucleic acid complex (Figure 26A) by HDOCK server. From the 10 best complexes achieved from docking results, the second complex was found suitable as per our *in vitro* results as it placed the anticodon of $tRNA^{Arg}$ near the xSKxxLKKxxK motif and its acceptor arm towards the CCD. While the T-loop was found to be positioned towards the catalytic pocket, the D-loop faced away from the protein surface. Furthermore, the nucleotides belonging to the minor groove of $tRNA^{Arg}$ formed polar contact with residues present near the ATP binding motif of *Ld*ArgRS (Figure 26B). For instance, the nucleotides from its acceptor arms, Gua68, Gua69, Ade70, Ura71, and Ura72, interacted with Asp477, Thr475, Arg445, Gln124, and Thr122, respectively. The conserved Ade20 nucleotide present in all ArgRSs, except *Saccharomyces cerevisiae*, was also found in *L. donovani* $tRNA^{Arg}$. Some of the residues (Glu359 and Lys365) from this motif formed H-bonds with nucleotides of the $tRNA^{Arg}$ anticodon viz., Gua44 and Ura28, respectively (Figure 26C). Moreover, the residues surrounding this motif, like Arg369, Asp373, and Lys374 interacted with nucleotides near its anticodon, which are Ura26,

Gua10, and Gua44, respectively.

To achieve a better understanding of the effect of $tRNA^{Arg}$ binding on *Ld*ArgRS structure and dynamics, *Ld*ArgRS and *Ld*ArgRS-$tRNA^{Arg}$ complex were subjected to molecular dynamics simulations (MDS) that were run for a span of 100 ns. The average RMSD, RMSF, and Rg values for *Ld*ArgRS-$tRNA^{Arg}$ complex were 0.3, 0.15, and 3.2 nm, respectively in contrast to corresponding 0.38, 0.175, and 3.26 nm for *Ld*ArgRS, indicating that $tRNA^{Arg}$ could bring overall stabilization, compactness, and rigidity to the protein. The apo *Ld*ArgRS could not attain complete stability throughout the run time, and the dynamics of *Ld*ArgRS-$tRNA^{Arg}$ appeared to be similar to *Ld*ArgRS until 60 ns. However, beyond 60 ns, the stability as well as compactness of *Ld*ArgRS-$tRNA^{Arg}$ enhanced as evident through RMSD and Rg plots (Figure 26D and E). From the RMSF plot, it is apparent that most of the fluctuations are present at the insertion region, while the CCD present on either side is rigid (Figure 26F). The binding of $tRNA^{Arg}$ led to a decrease in fluctuations, which further implies that the structure of insertion is highly flexible in nature. It is also noteworthy that RMSF of tRNA binding motif (Leu355-Lys365) reduced considerably (Figure 26G). Apart from this region, higher fluctuations were observed towards the N-terminus of the protein, and binding of $tRNA^{Arg}$ did not greatly help in the reduction of these fluctuations.

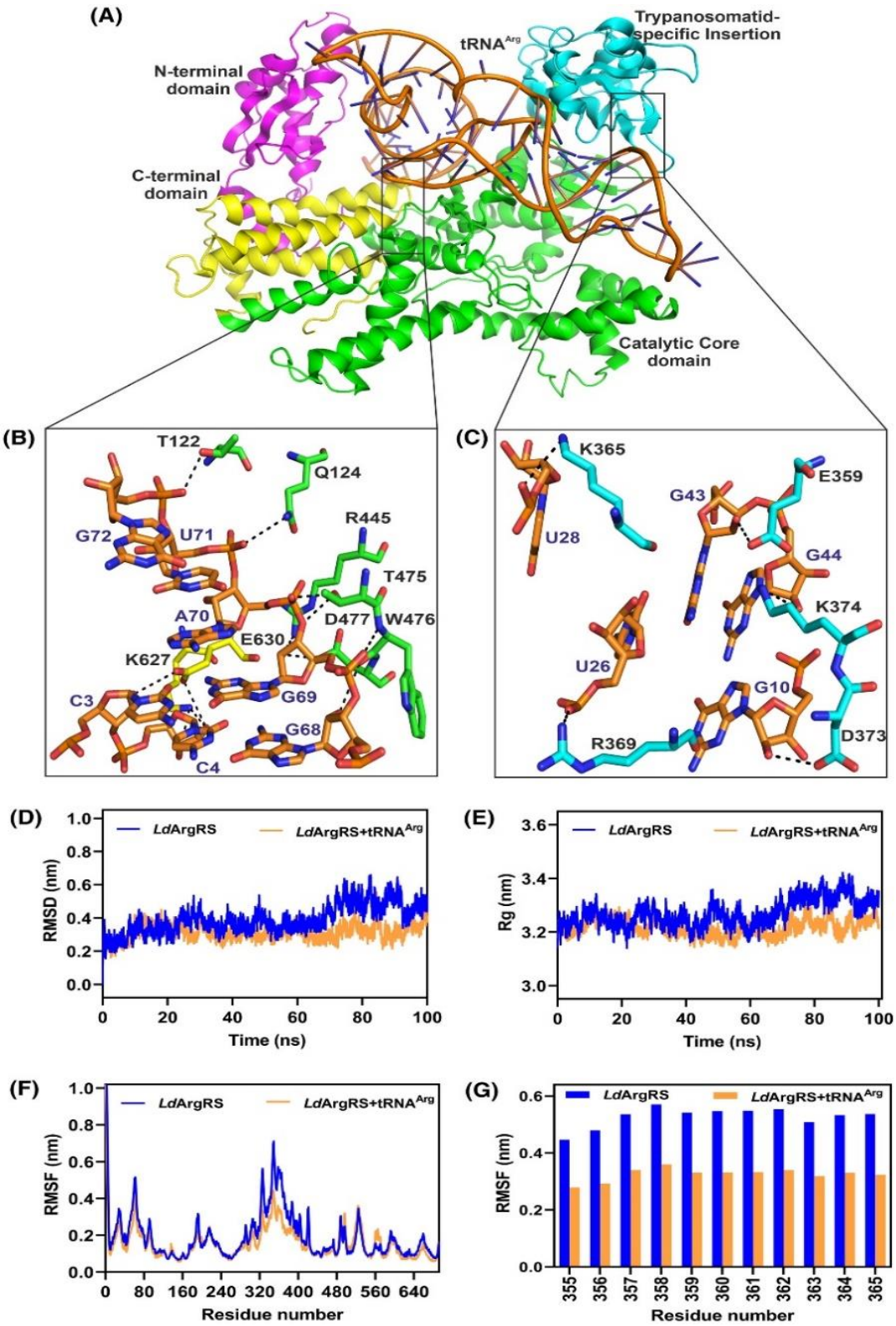

Figure 26: Docking and MD simulation (MDS) of *Ld*ArgRS with tRNA^{Arg}. (A) Docked complex showing the positioning of *L. donovani* tRNA^{Arg} on *Ld*ArgRS. The structure of protein was retrieved from the AlphaFold database; Interaction of (B) tRNA^{Arg} acceptor arm with catalytic core domain of *Ld*ArgRS,

and (C) $tRNA^{Arg}$ anticodon with the consensus tRNA binding motif of trypanosomatid-specific insertion region; (D-F) RMSD, Rg, and RMSF plots of *Ld*ArgRS and *Ld*ArgRS-$tRNA^{Arg}$ complex; (G) Decrease in RMSF values at the consensus motif upon $tRNA^{Arg}$ binding.

5.1.5. Comp-7j stabilizes *Ld*ArgRS better than L-Arg and ATP

The ligands of *Ld*ArgRS were docked at its active site in order to assess how they interact with the residues of the catalytic pocket (Figure 27A). Docking of leishmanial protein with its cognate ligands brought them close to each other with some common interacting residues. This might be possible due to the fact that the substrate and cofactor binding sites are generally in close proximity in ArgRS [99]. The binding affinity of L-Arg was the lowest when compared to the other two ligands and was found to be -5.2 kcal/mol. In total, three polar contacts and five hydrophobic interactions were seen (Figure 27B). The residues Asp129, Asn134, and Tyr426 interacted with NH2, ND2, and NE atoms of L-Arg, respectively, while there were hydrophobic interactions between the L-Arg and Ala132, His169, Thr450, Gln454, and Phe484 of *Ld*ArgRS.

With regards to ATP, the binding affinity was found to be -9 kcal/mol, and the adenine group was placed towards the third ATP binding motif, i.e., FGLVT. The N1 and O4 atoms of the adenine ring formed polar contacts with Val484 and Gln454, respectively (Figure 27C). At the triphosphate region, atoms O1, O7, and O9 of ATP interacted with His140 via H-bonds, while O11 and O12 interacted with Asn134. Moreover, there were hydrophobic interactions between Pro133 and His143 at the triphosphate region and Gly142, Phe481, Gly482, and Leu483 at the adenine region. Apart from the residues known to be present at the ATP binding motif, some other residues were observed near the motif interacting with ATP. For example, Lys137, Gln454, and Lys491 interacted with O6, O3, and N4 atoms of ATP through H-bonds. Also, Glu138 showed hydrophobic interactions near the O5 and O8 atoms. It was observed that Comp-7j superimposed on the adenine ring of ATP, and its binding affinity was computed to be -8.7 kcal/mol (Figure 27D). Interactions were majorly hydrophobic in nature, and the portion mimicking the adenine ring interacted with all residues present in the FGLVT motif except Thr485 observed in the ATP-docked complex and it interacted with His140, Gly142, His143, and Asp451. Similar to ATP, Comp-7j also formed polar contact with Gln454 that is present near the ATP binding motif and hydrophobically interacted with Thr450 of the substrate binding motif. It highlights that Thr450 is important as it is replaced with Val408 in *Hs*ArgRS.

The dynamics for docked complexes of *Ld*ArgRS with ATP, Comp-7j, and L-Arg were also studied, wherein comparable stabilities, compactness, and rigidity were observed for all the complexes. The average RMSD, RMSF, and Rg for the ATP-bound complex were found to be 0.45, 0.21, and 3.28 nm, respectively in comparison to 0.38, 0.175, and 3.26 nm for *Ld*ArgRS. Up to 75 ns, the stability and compactness of the ATP bound form were observed to be poor, after which, both of these parameters started to improve. Similarly, the corresponding average RMSD, RMSF, and Rg for L-Arg-bound complex was 0.4, 0.2, and 3.22 nm. Hence, it can be inferred that although the binding of L-Arg did not improve the stability of *Ld*ArgRS, it helped to increase the compactness of the protein as evident from the average Rg values of *Ld*ArgRS and *Ld*ArgRS-L-Arg complex. The inhibitor Comp-7j, on the other hand, enhanced stability as well as compactness starting from 30 ns as observed through RMSD and Rg plots. This is in turn reflected in their average RMSD and Rg values that were close to that of apo *Ld*ArgRS, viz., 0.39 and 3.26 nm, respectively (Figure 27E and F). The RMSF plots for all the bound forms were comparable except for the L-Arg bound complex, which destabilized the insertion region, although the catalytic pocket on either side was rigid (Figure 27G and H).

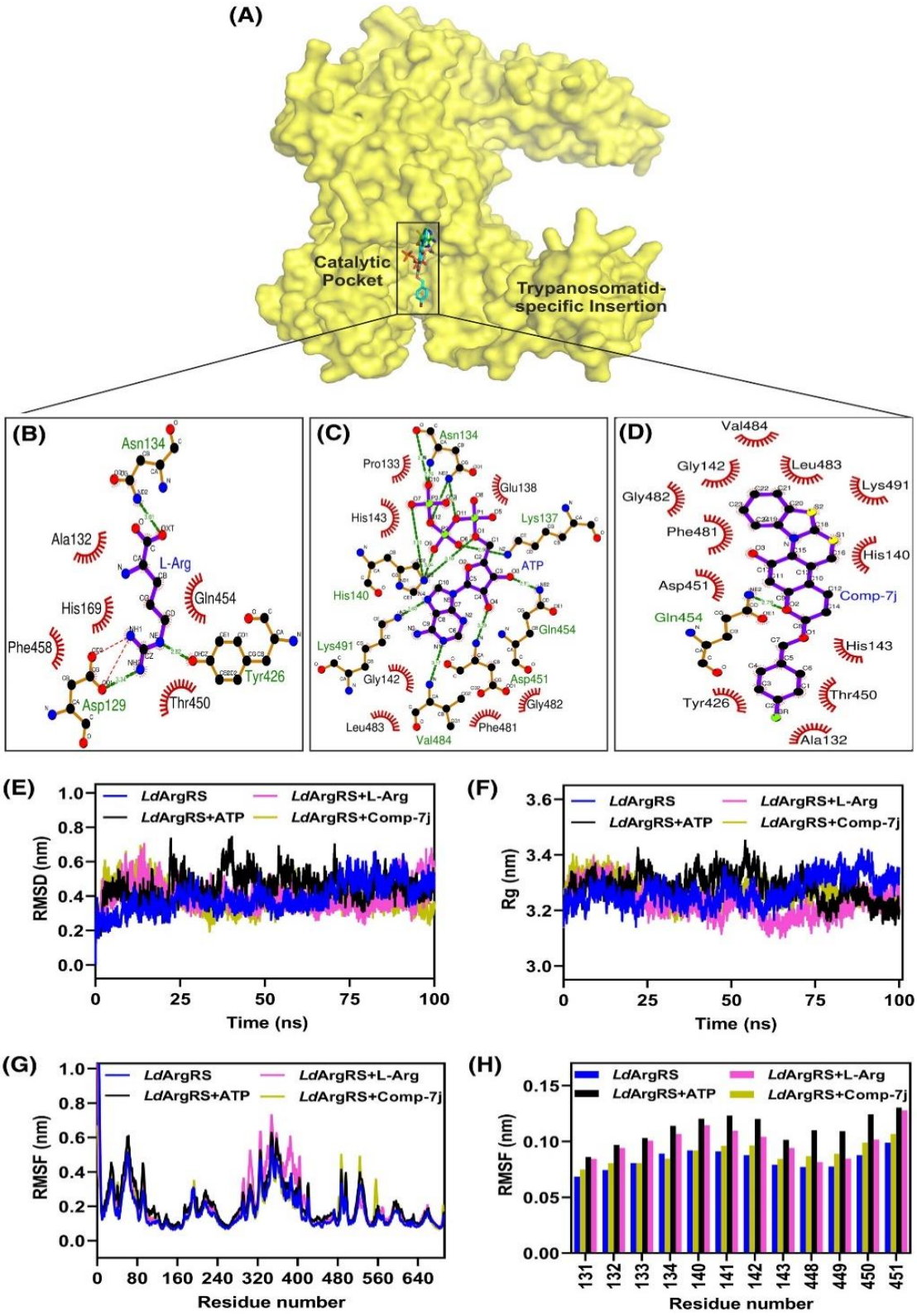

Figure 27: Interaction studies of *Ld*ArgRS with various ligands. *Ld*ArgRS displaying the catalytic pocket and trypanosomatid-specific insertion. (A) The surface model was generated using the PyMOL

software; Hydrogen and hydrophobic interactions of *Ld*ArgRS with (B) L-Arg, (C) ATP, and (D) Comp-7j; (E) RMSD, (F) Rg, and (G) RMSF plots of *Ld*ArgRS and *Ld*ArgRS-ligand complexes; (H) RMSF values at the catalytic pocket upon binding of L-Arg, ATP, and Comp-7j.

5.1.6. Structural features of *Ld*HisRS

By employing AlphaFold colab 2, the three-dimensional structure of *Ld*HisRS was obtained that contained 95.3% residues in most favoured, 4.3% residues in the additionally allowed, and 0.4% in disallowed regions. With subsequent refinement of *Ld*HisRS structure, the ERRAT score was observed to be 94.78 with 0% residues in the disallowed region. The structure of *Ld*HisRS has 3 domains i.e., N-terminal domain (NTD), catalytic core domain (CCD), and C-terminal or anticodon binding domain (CTD) (Figure 28A). The distinctive feature of class-II aaRSs was present in the CCD and the leishmanial ID depicted resemblance with that of ID from *Tc*HisRS. The M2 loop was made up of Ala158-Ile159-Ser160-Arg161-Gly162 which is important for ligand binding. The *Ld*HisRS CTD was linked to the CCD by a loop made from Lys347 to Asp359.

The ligands of *Ld*HisRS viz., ATP, L-His, and Comp-7m depicted good affinity scores when docked with the protein (Figure 28B). The ligands made polar contacts with the identical leishmanial residues that were earlier reported for the *Tc*HisRS-ligand complexes. The binding affinity of L-His towards *Ld*HisRS was computed to be -5.4 kcal/mol. Polar interactions were involved between L-His and Tyr317 as well as Tyr318, and its amino group also formed H-bonds with Glu125 and Thr127 (Figure 28C). Likewise, the L-His carboxy group interacted with Arg115 and Gln169, while there was a non-polar interaction between Tyr341 and the substrate. The ATP molecule showed an affinity of -8 kcal/mol for *Ld*HisRS (Figure 28D). The corresponding *Tc*HisRS residues in leishmanial HisRS are Arg155 and Arg313 which are necessary for interacting with ATP. Gln169 also interacting with ATP bridges oxygen atoms between the ribose group and histidine for the formation of histidyl-adenylate in *Trypanosoma* HisRS [45]. The leishmanial residues Ala334, Ile335, and G362 correspond to trypanosomal Ala 335, Leu336, and G363 residues that facilitate the positioning of ribose group via electrophilic reaction. The key ATP-binding residues Glu157 and Arg164 in trypanosomatid HisRSs interact with the N6 atom of ATP through strong H-bonds. Comp-7m, the potent inhibitor of *Ld*HisRS superimposed on the adenine ring of ATP with a binding affinity of -8.2 kcal/mol (Figure 28E), thus delineating a competitive mode of inhibition. Some of the common interactions were Arg155 and His167 which

made polar and non-polar contacts, respectively with Comp-7m. Likewise, Arg313 and Arg333 formed H-bonds with the trailing of inhibitor while Ala334 linked to Comp-7m through H-bond. Other residues that interacted with Comp-7m were Ile105, Leu315, Glu324, and Cys336.

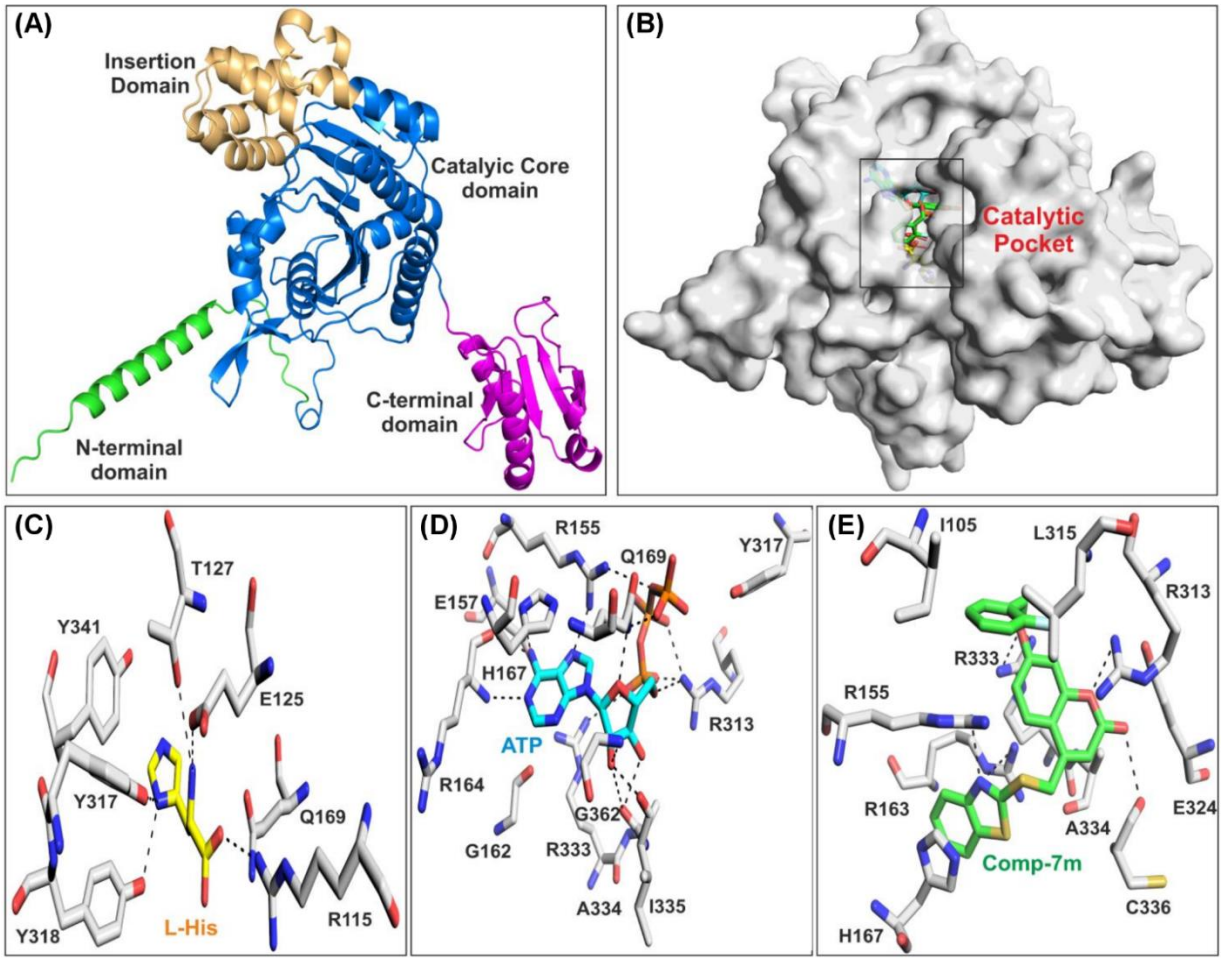

Figure 28: Structure of *Ld*HisRS and its interactions with ligands. (A) *Ld*HisRS with its domain arrangement; (B) Surface model of *Ld*HisRS displaying catalytic pocket; Hydrogen and hydrophobic interactions between *Ld*HisRS and (C) L-His, (D) ATP, and (E) Comp-7m.

5.1.7. Molecular dynamic simulation of *Ld*HisRS and its complexes

The dynamics of the apo and ligand-bound truncated protein (Pro60 to Leu379) were found to be similar. However, the apo *Ld*HisRS did not attain stabilization in the entire course of simulation, while the ligand-bound complexes subsequently achieved stability beyond 70 ns. The average RMSD was calculated as 0.22, 0.25, 0.26, and 0.26 nm for the corresponding *Ld*HisRS (Apo), *Ld*HisRS+L-His, *Ld*HisRS+ATP, and *Ld*HisRS+Comp-7m, respectively (Figure 29A). Moreover,

*Ld*HisRS, *Ld*HisRS+L-His, *Ld*HisRS+ATP, and *Ld*HisRS+Comp-7m possessed similar average Rg values viz. 1.97, 2.00, 2.01, and 1.99 nm, respectively (Figure 29B). A considerable decrement with respect to fluctuations in *Ld*HisRS-ligand complexes was observed when compared to apo form since the average RMSF values for *Ld*HisRS, *Ld*HisRS+L-His, *Ld*HisRS+ATP, and *Ld*HisRS+Comp-7m were computed to be 0.128, 0.107, 0.11, and 0.11 nm (Figure 29C). Furthermore, after the binding of ligands, a significant decrease in fluctuations was observed in the residues of the active site (Figure 29D). In order to compute the binding energy of Comp-7m and ATP for *Ld*HisRS, MM/PBSA analysis was performed (Table 14). Even though the SASA and Van der Waals energies were similar for *Ld*HisRS-Comp+7m and *Ld*HisRS+ATP, their corresponding binding energies were -71.49±10.3 and -10.47±1.2 kJ/mol, depicting greater binding affinity of Comp-7m towards *Ld*HisRS.

Table 14: MM/PBSA analysis of *Ld*HisRS with ATP versus Comp-7m

Energy (kJ/mol)	***Ld*HisRS+ATP**	***Ld*HisRS+Comp-7m**
Van der Waals	-109.57	-110.53
Electrostatic	-148.25	-26.72
Polar Solvation	260.82	79.29
SASA	-13.46	-13.53
Binding	-10.47	-71.49

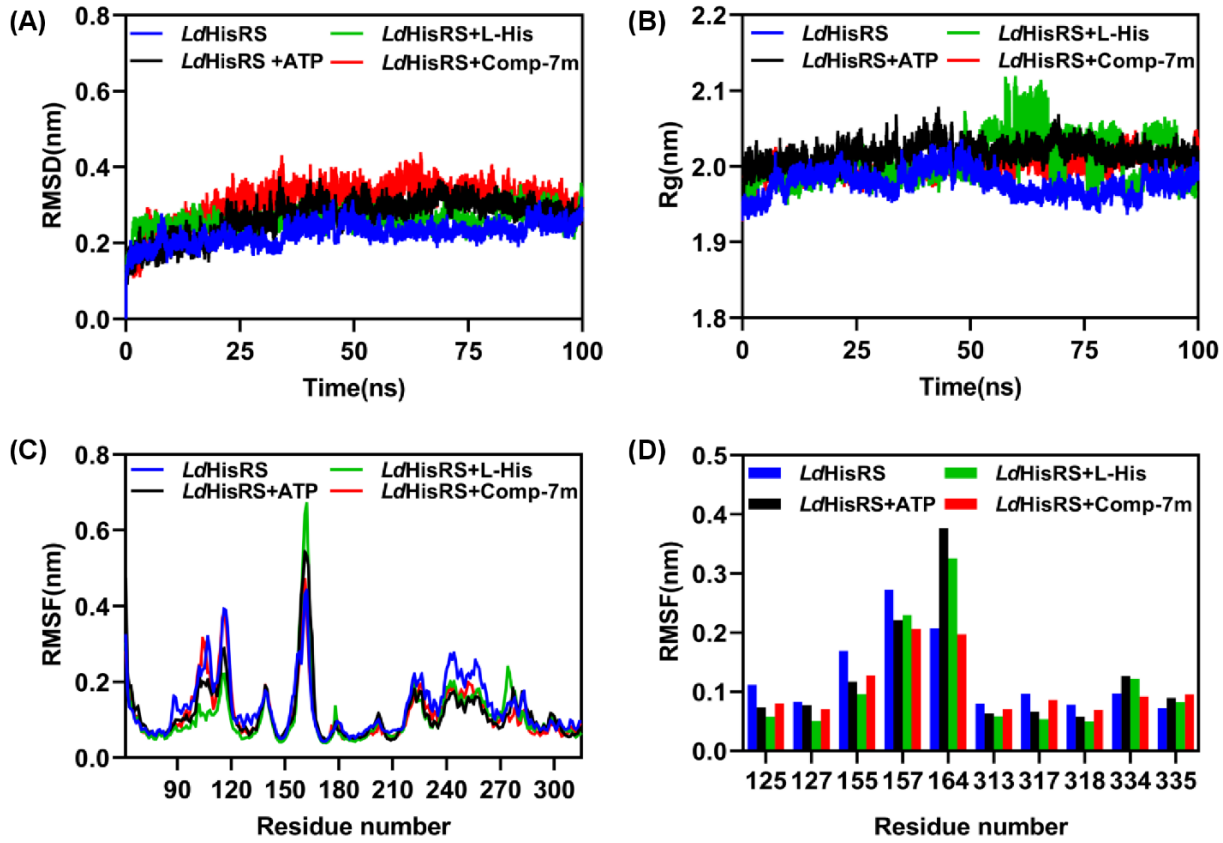

Figure 29: MD simulation analyses of *Ld*HisRS and its complexes. (A) RMSD, (B) Rg, and (C) RMSF plots of *Ld*HisRS and its ligand-bound complexes; (D) Reductions in fluctuations at the catalytic pocket upon ligand binding.

5.1.8. Mutation of key ATP-binding residues enhances thermostability of *Ld*HisRS

To ascertain that point-mutations of Glu157 and Arg164 enhance thermostability of *Ld*HisRS (WT), we validated our results through CD spectroscopy wherein we subjected the WT, E157A, and R164A to MDS at 328 K. The mutant forms obtained better stability than WT after 50 ns and their average RMSD values were calculated to be 0.31 and 0.29 nm, respectively over 0.34 nm of WT (Figure 30A). Although the corresponding average Rg of WT, E157A, and Arg164A were calculated to be 2.00, 2.02, and 2.019 nm indicating minimal change in the cumulative compactness of mutant forms (Figure 30B), the overall flexibilities of E157A and R164A were comparable as their average RMSF was 0.14 and 0.138 nm, respectively in contrast to 0.141 nm for WT (Figure 30C). The decrease in fluctuations is also apparent in the catalytic pocket residues (Figure 30D). Moreover, the mutants demonstrated a larger area representing the lower free energy than WT protein at 328 K, (Figure 30 E-G) indicating that E157A and R164A could remain folded

even at a higher temperature as compared to the native *Ld*HisRS.

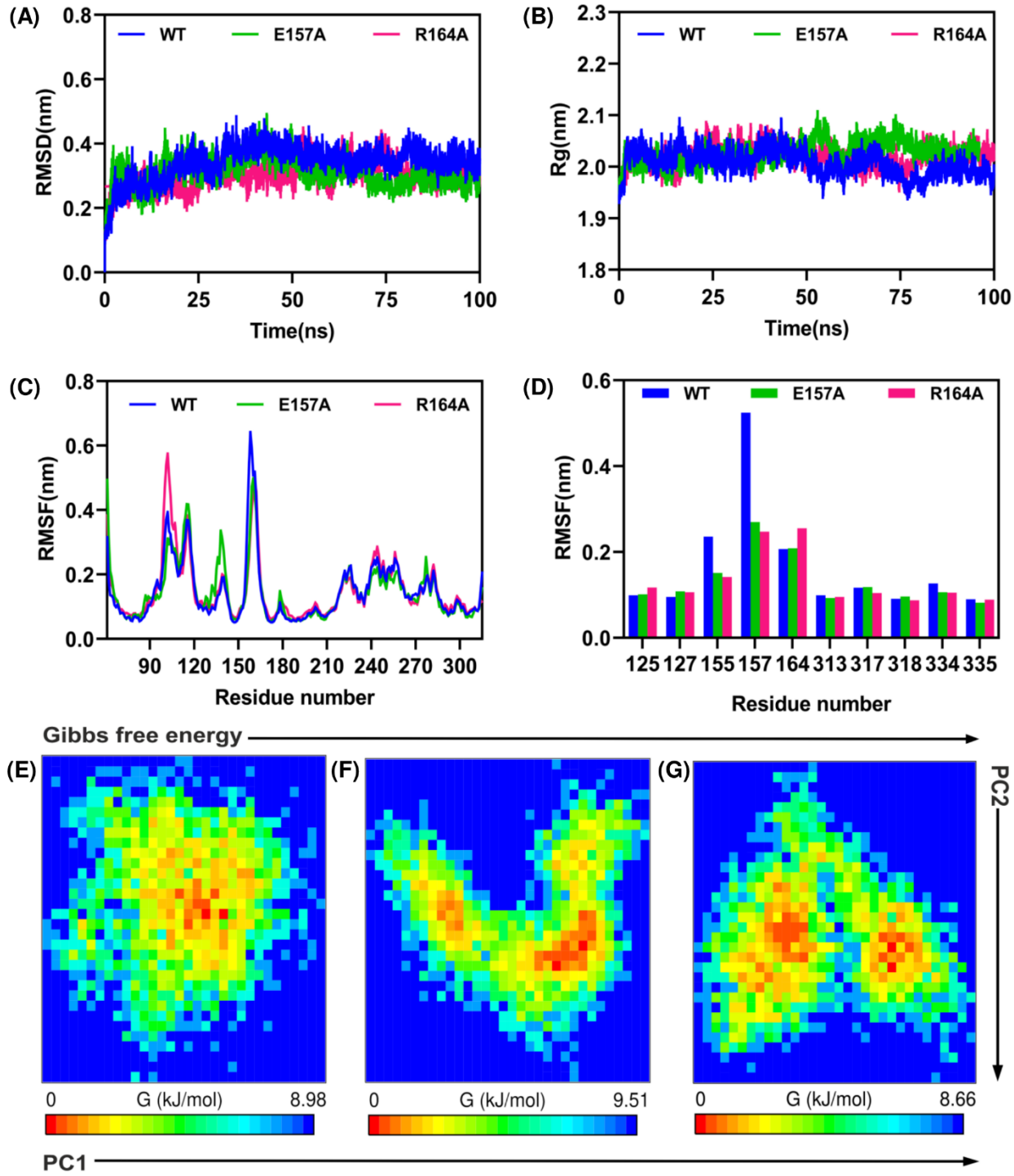

Figure 30: Comparative MDS studies of *Ld*HisRS and its mutants. (A) RMSD, (B) Rg, and (C) RMSF graphs of *Ld*HisRS and its mutants; (D) RMSF comparison for active site residues in *Ld*HisRS and its mutants after mutations; FEL diagrams of (E) WT, (F) E157A, and (G) R164A.

5.2. Discussion

As delineated for another truncated protein i.e., human apolipoprotein E4 [100], ΔIns-*Ld*ArgRS showed an increased tolerance toward chemical denaturation unlike *Ld*ArgRS. At different pH buffers, both full-length and deletion-mutant contained different secondary structural content. For instance, *Ld*ArgRS possessed comparatively fewer a-helices at extreme pH conditions compared to physiological pH as previously documented for leishmanial SerRS [51], AspRS [34], and GluRS [79]. The conversion of most of the a-helices to b-sheets for ΔIns-*Ld*ArgRS in the presence of L-Arg was intriguing as such a phenomenon is associated with the aggregation of proteins [101–104]. Moreover, as per the previous reports, the transition of a-helices to b-sheets has been previously linked to a significant increase in protein stability and energy dissipation capacity [105, 106]. It has also been demonstrated that higher b-sheet content stiffens the protein and is thus more resistant to shearing than the proteins predominantly containing a-helices [102]. Low and very high concentrations of L-Arg promote and prevent aggregation of proteins, respectively [107], and ΔIns-*Ld*ArgRS lacking the highly basic trypanosomatid-specific insertion might be undergoing aggregation at an L-Arg concentration needed for enzyme activity, while *Ld*ArgRS can tolerate such a situation. In this regard, it has been stated that trypanosomatids have to pull through a condition of L-Arg starvation since their infection activates the host defense mechanism causing the arginine milieu within macrophages to deplete [108]. Conversely, earlier studies suggest that ArgRS activation by tRNA needs a high L-Arg concentration for stabilization of the anticodon arm and formation of a proper ATP binding site [62, 109]. The modeled *Ld*ArgRS structure consisted of deviations from other ArgRSs apart from the trypanosomatid-specific insertion. The interaction between Ade20 of D-loop from $tRNA^{Arg}$ and the N-terminal of ArgRS is necessary for $tRNA^{Arg}$ binding in *T. thermophilus* [99] and *E. coli* [110], but not in *S. cerevisiae* [111]. In our study, the D-loop was present away from the protein surface, suggesting that this loop may not help in tRNA binding in *L. donovani*, like S. cerevisiae. The Rossmann fold consisting of ligand binding sites was split into two antiparallel b-strands on either side of the insertion forming a shorter b-sheet. The KMSKS motif is replaced by KKIKT, and unlike *Pyrococcus horikoshii* ArgRS [112], the first lysine residue of this motif, Lys491, interacted with the adenine of ATP, suggesting its role in ATP-PPi exchange reaction. Interactions formed between the protein and inhibitor was mostly hydrophobic owing to the non-polar nature of Comp-7j and Lys491 of the KKIKT motif also interacted hydrophobically near the first benzene ring of Comp-7j. The differential inhibition between human and leishmanial proteins is mostly because of Thr450 of

*Ld*ArgRS, which is replaced by Val408 in *Hs*ArgRS. The lone pair of oxygen in the threonine side chain forms a strong electrostatic bond with the polarized bromine [113], and the same was also observed here. Notably, these halogen-oxygen interactions are comparable with H-bonds on account of several common properties [113]. Previously, the addition of bromine to quinazoline inhibitors has been also shown to inhibit ProRS efficiently [114]. Moreover, the interaction between the threonine and halogen groups of quinoline carbaldehydes has been proven as crucial for enhanced inhibition of *Ld*MetAP1 [83]. Analyses from MDS studies of *Ld*ArgRS-ligand complexes imply that binding of tRNAArg to the trypanosomatid-specific insertion stabilizes the protein dynamics better than any other ligand. Comp-7j, however, conferred better compactness and stability than ATP or L-Arg.

The secondary structural features of *Ld*HisRS were in line with earlier findings on other HisRSs, and *Tc*HisRS has also been shown to exhibit an increase in thermal stability following ligand binding [45]. When GdHCl was present, *Ld*HisRS was prone to early denaturation, which has been shown to disrupt proteins at lower doses [115]. Also, greater thermal stability was demonstrated for *Ld*HisRS when the key residues were substituted with alanine as reported earlier [116-118]. Furthermore, a decrease in ellipticity is seen in the proteins that depict slower unfolding [119]. In this regard, we observed enhanced stability for *Ld*HisRS mutants in the MDS studies. The NTD (N-terminal domain) remained unstructured because of the lack of a template whereas other eukaryotes possess a two-helix bundle in NTD [120, 121] without which it becomes inactive [122]. Comp-7m was bound to *Ld*HisRS with hydrophobic interactions and delineated more specificity for the leishmanial enzyme than ATP which was further confirmed by MM/PBSA analysis [97]. Enriched specificity of inhibitors is caused by any small differences between human and pathogenic aaRSs which shed light on the importance of ATP-analogs and their usage as inhibitors [123, 124].

6. Summary

In summary, we report an ArgRS from *L. donovani* that performs the ATP-PPi exchange reaction in the absence of $tRNA^{Arg}$. The trypanosomatid-specific insertion helps in the binding of tRNA and is also responsible for modulating the structural as well as catalytic properties. We speculate that the presence of insertion renders an evolutionary advantage to trypanosomatids by helping them survive in lower arginine conditions and promoting aminoacylation in two ways: 1) the highly basic composition enhances the solubility of the protein, thus preventing aggregation and 2) its flexible nature helps in the easy capture of tRNA. However, the correct positioning and structure of the anticodon domain should be further confirmed through experimental studies. Most of the unique domains added to aaRSs are a result of horizontal gene transfer; hence, a detailed study with evolutionary aspect is required. Furthermore, differences in the residues of the human and leishmanial enzymes form the basis of selective inhibition by benzothiazolo-coumarin derivatives while further optimization might lead us to molecules that can function at a nanomolar scale. The deviation of *Ld*ArgRS from the ArgRSs of other organisms can be thoroughly exploited for the derivation of newer and more potent antileishmanials. Similarly, the current study examined the biophysical and biochemical characteristics of a leishmanial histidyl-tRNA synthetase (*Ld*HisRS), which was found to differ sequence-wise and structurally than *Hs*HisRS. As HisRSs are essential for other trypanosomatids' survival in the past, this enzyme could potentially be necessary for *Leishmania donovani*'s growth as well. HisRSs have also been elucidated earlier to harbor dimeric nature along with more α-helices. Furthermore, compared to monovalent ions, divalent ions are pivotal for *Ld*HisRS and our mutational study highlighted the critical function of *Leishmania*-specific ATP-binding residues. The lead molecule showed a competitive mechanism of inhibition, which is also validated by docking studies. Furthermore, improved potency and specificity can be achieved by further refining the inhibitors discussed here. Therefore, a comprehensive assessment of *Ld*HisRS structure and its inhibition by ATP-analogs as described here would be helpful in the emergence of effective inhibitors for leishmaniasis.

7. References

1) Davies CR, Kaye P, Croft SL, Sundar S. Leishmaniasis: new approaches to disease control. BMJ. 2003 Feb 15;326(7385):377-82. doi: 10.1136/bmj.326.7385.377.

2) Zijlstra EE. The immunology of post-kala-azar dermal leishmaniasis (PKDL). Parasit Vectors. 2016 Aug 23;9(1):464. doi: 10.1186/s13071-016-1721-0.

3) Sundar S, Agrawal N, Singh B. Exploiting knowledge on pharmacodynamics-pharmacokinetics for accelerated anti-leishmanial drug discovery/development. Expert Opin Drug Metab Toxicol. 2019 Jul;15(7):595-612. doi: 10.1080/17425255.2019.1629417.

4) Pérez-Victoria FJ, Sánchez-Cañete MP, Seifert K, Croft SL, Sundar S, Castanys S, Gamarro F. Mechanisms of experimental resistance of *Leishmania* to miltefosine: Implications for clinical use. Drug Resist Updat. 2006 Feb-Apr;9(1-2):26-39. doi: 10.1016/j.drup.2006.04.001.

5) Shapira M, Zinoviev A. *Leishmania* parasites act as a Trojan horse that paralyzes the translation system of host macrophages. Cell Host Microbe. 2011 Apr 21;9(4):257-9. doi: 10.1016/j.chom.2011.04.004.

6) Gazestani VH, Nikpour N, Mehta V, Najafabadi HS, Moshiri H, Jardim A, Salavati R. A Protein Complex Map of *Trypanosoma brucei*. PLoS Negl Trop Dis. 2016 Mar 18;10(3):e0004533. doi: 10.1371/journal.pntd.0004533.

7) Dmitriev SE, Vladimirov DO, Lashkevich KA. A quick guide to small-molecule inhibitors of eukaryotic protein synthesis. Biochemistry (Mosc). 2020 Nov;85(11):1389-1421. doi: 10.1134/S0006297920110097.

8) Pham JS, Dawson KL, Jackson KE, Lim EE, Pasaje CF, Turner KE, Ralph SA. Aminoacyl-tRNA synthetases as drug targets in eukaryotic parasites. Int J Parasitol Drugs Drug Resist. 2013 Nov 11;4(1):1-13. doi: 10.1016/j.ijpddr.2013.10.001.

9) Chhibber-Goel J, Joshi S, Sharma A. Aminoacyl tRNA synthetases as potential drug targets of the Panthera pathogen *Babesia*. Parasit Vectors. 2019 Oct 14;12(1):482. doi: 10.1186/s13071-019-3717-z.

10) Lukarska M, Palencia A. Aminoacyl-tRNA synthetases as drug targets. Enzymes. 2020;48:321-350. doi: 10.1016/bs.enz.2020.07.001.

11) Gill J, Sharma A. Exploration of aminoacyl-tRNA synthetases from eukaryotic parasites for drug development. J Biol Chem. 2023 Mar;299(3):102860. doi: 10.1016/j.jbc.2022.102860.

12) Cusack S. Aminoacyl-tRNA synthetases. Curr Opin Struct Biol. 1997 Dec;7(6):881-9. doi: 10.1016/s0959-440x(97)80161-3.

13) Park SG, Ewalt KL, Kim S. Functional expansion of aminoacyl-tRNA synthetases and their interacting factors: new perspectives on housekeepers. Trends Biochem Sci. 2005 Oct;30(10):569-74. doi: 10.1016/j.tibs.2005.08.004.

14) Kim S, You S, Hwang D. Aminoacyl-tRNA synthetases and tumorigenesis: more than housekeeping. Nat Rev Cancer. 2011 Sep 23;11(10):708-18. doi: 10.1038/nrc3124.

15) Antonellis A, Green ED. The role of aminoacyl-tRNA synthetases in genetic diseases. Annu Rev Genomics Hum Genet. 2008;9:87-107. doi: 10.1146/annurev.genom.9.081307.164204.

16) Eriani G, Cavarelli J, Martin F, Ador L, Rees B, Thierry JC, Gangloff J, Moras D. The class II aminoacyl-tRNA synthetases and their active site: evolutionary conservation of an ATP binding site. J Mol Evol. 1995 May;40(5):499-508. doi: 10.1007/BF00166618.

17) O'Donoghue P, Luthey-Schulten Z. On the evolution of structure in aminoacyl-tRNA synthetases. Microbiol Mol Biol Rev. 2003 Dec;67(4):550-73. doi: 10.1128/MMBR.67.4.550-573.2003.

18) de Melo Neto O P, Reis C R, Moura D M, Freire E R, Carrington M. Unique and conserved features of the protein synthesis apparatus in parasitic trypanosomatid (*Trypanosoma* and *Leishmania*) species. In Evolution of the protein synthesis machinery and its regulation; Springer, 2016; 435-475. doi: 10.1007/978-3-319-39468-8_17

19) Shikha S, Brogli R, Schneider A, Polacek N. tRNA Biology in trypanosomes. Chimia (Aarau). 2019 May 29;73(5):395-405. doi: 10.2533/chimia.2019.395.

20) Gowri VS, Ghosh I, Sharma A, Madhubala R. Unusual domain architecture of aminoacyl tRNA synthetases and their paralogs from *Leishmania major*. BMC Genomics. 2012 Nov 14;13:621. doi: 10.1186/1471-2164-13-621.

21) Nilsson D, Gunasekera K, Mani J, Osteras M, Farinelli L, Baerlocher L, Roditi I, Ochsenreiter T. Spliced leader trapping reveals widespread alternative splicing patterns in

the highly dynamic transcriptome of *Trypanosoma brucei*. PLoS Pathog. 2010 Aug 5;6(8):e1001037. doi: 10.1371/journal.ppat.1001037.

22) Agarwal V, Nair S K. Aminoacyl tRNA synthetases as targets for antibiotic development. Med Chem Comm. 2012 3.8: 887-898. DOI: 10.1039/C2MD20032E

23) Gould MK, Vu XL, Seebeck T, de Koning HP. Propidium iodide-based methods for monitoring drug action in the kinetoplastidae: comparison with the Alamar Blue assay. Anal Biochem. 2008 Nov 15;382(2):87-93. doi: 10.1016/j.ab.2008.07.036.

24) Faria J, Moraes CB, Song R, Pascoalino BS, Lee N, Siqueira-Neto JL, Cruz DJ, Parkinson T, Ioset JR, Cordeiro-da-Silva A, Freitas-Junior LH. Drug discovery for human African trypanosomiasis: identification of novel scaffolds by the newly developed HTS SYBR Green assay for *Trypanosoma brucei*. J Biomol Screen. 2015 Jan;20(1):70-81. doi: 10.1177/1087057114556236.

25) Manhas R, Tandon S, Sen SS, Tiwari N, Munde M, Madhubala R. Leishmania donovani Parasites Are Inhibited by the Benzoxaborole AN2690 Targeting Leucyl-tRNA Synthetase. Antimicrob Agents Chemother. 2018 Aug 27;62(9):e00079-18. doi: 10.1128/AAC.00079-18.

26) Tandon S, Manhas R, Tiwari N, Munde M, Vijayan R, Gourinath S, Muthuswami R, Madhubala R. Deciphering the interaction of benzoxaborole inhibitor AN2690 with connective polypeptide 1 (CP1) editing domain of *Leishmania donovani* leucyl-tRNA synthetase. J Biosci. 2020;45:63. doi: 10.1007/s12038-020-00031-8

27) Larson ET, Kim JE, Zucker FH, Kelley A, Mueller N, Napuli AJ, Verlinde CL, Fan E, Buckner FS, Van Voorhis WC, Merritt EA, Hol WG. Structure of *Leishmania major* methionyl-tRNA synthetase in complex with intermediate products methionyladenylate and pyrophosphate. Biochimie. 2011 Mar;93(3):570-82. doi: 10.1016/j.biochi.2010.11.015.

28) Torrie LS, Brand S, Robinson DA, Ko EJ, Stojanovski L, Simeons FRC, Wyllie S, Thomas J, Ellis L, Osuna-Cabello M, Epemolu O, Nühs A, Riley J, MacLean L, Manthri S, Read KD, Gilbert IH, Fairlamb AH, De Rycker M. Chemical Validation of Methionyl-tRNA Synthetase as a Druggable Target in *Leishmania donovani*. ACS Infect Dis. 2017 Oct 13;3(10):718-727. doi: 10.1021/acsinfecdis.7b00047.

29) Anand S, Madhubala R. Twin Attributes of Tyrosyl-tRNA Synthetase of *Leishmania donovani*: A housekeeping protein translation enzyme and a mimic of host chemokine. J Biol Chem. 2016 Aug 19;291(34):17754-71. doi: 10.1074/jbc.M116.727107.

30) Barros-Álvarez X, Kerchner KM, Koh CY, Turley S, Pardon E, Steyaert J, Ranade RM, Gillespie JR, Zhang Z, Verlinde CLMJ, Fan E, Buckner FS, Hol WGJ. *Leishmania donovani* tyrosyl-tRNA synthetase structure in complex with a tyrosyl adenylate analog and comparisons with human and protozoan counterparts. Biochimie. 2017 Jul;138:124-136. doi: 10.1016/j.biochi.2017.04.006.

31) Ogungbe IV, Ng JD, Setzer WN. Interactions of antiparasitic alkaloids with Leishmania protein targets: a molecular docking analysis. Future Med Chem. 2013 Oct;5(15):1777-99. doi: 10.4155/fmc.13.114.

32) Ogungbe IV, Erwin WR, Setzer WN. Antileishmanial phytochemical phenolics: molecular docking to potential protein targets. J Mol Graph Model. 2014 Mar;48:105-17. doi: 10.1016/j.jmgm.2013.12.010.

33) Kelly P, Hadi-Nezhad F, Liu DY, Lawrence TJ, Linington RG, Ibba M, Ardell DH. Targeting tRNA-synthetase interactions towards novel therapeutic discovery against eukaryotic pathogens. PLoS Negl Trop Dis. 2020 Feb 27;14(2):e0007983. doi: 10.1371/journal.pntd.0007983.

34) Panigrahi GC, Qureshi R, Jakkula P, Kumar KA, Khan N, Qureshi IA. Leishmanial aspartyl-tRNA synthetase: Biochemical, biophysical and structural insights. Int J Biol Macromol. 2020 Dec 15;165(Pt B):2869-2885. doi: 10.1016/j.ijbiomac.2020.10.140.

35) Chadha S, Mallampudi NA, Mohapatra DK, Madhubala R. Genetic validation of *Leishmania donovani* lysyl-tRNA synthetase shows that it is indispensable for parasite growth and infectivity. mSphere. 2017 Aug 30;2(4):e00340-17. doi: 10.1128/mSphereDirect.00340-17.

36) Mitra SK, Mehler AH. The arginyl transfer ribonucleic acid synthetase of *Escherichia coli*. J Biol Chem. 1967 Dec 10;242(23):5490-4. doi: 10.1016/S0021-9258(18)99385-3

37) Grant TD, Luft JR, Wolfley JR, Snell ME, Tsuruta H, Corretore S, Quartley E, Phizicky EM, Grayhack EJ, Snell EH. The structure of yeast glutaminyl-tRNA synthetase and modeling of its interaction with tRNA. J Mol Biol. 2013 Jul 24;425(14):2480-93. doi: 10.1016/j.jmb.2013.03.043.

38) Deutscher MP. Rat liver glutamyl ribonucleic acid synthetase. II. Further properties and anomalous pyrophosphate exchange. J Biol Chem. 1967 Mar 25;242(6):1132-9. doi: 10.1016/S0021-9258(18)96154-5

39) Blais SP, Kornblatt JA, Barbeau X, Bonnaure G, Lagüe P, Chênevert R, Lapointe J. tRNAGlu increases the affinity of glutamyl-tRNA synthetase for its inhibitor glutamyl-sulfamoyl-adenosine, an analogue of the aminoacylation reaction intermediate glutamyl-AMP: mechanistic and evolutionary implications. PLoS One. 2015 Apr 10;10(4):e0121043. doi: 10.1371/journal.pone.0121043.

40) Kalidas S, Cestari I, Monnerat S, Li Q, Regmi S, Hasle N, Labaied M, Parsons M, Stuart K, Phillips MA. Genetic validation of aminoacyl-tRNA synthetases as drug targets in *Trypanosoma brucei*. Eukaryot Cell. 2014 Apr;13(4):504-16. doi: 10.1128/EC.00017-14.

41) Jain V, Yogavel M, Sharma A. Dimerization of arginyl-tRNA synthetase by free heme drives its inactivation in *Plasmodium falciparum*. Structure. 2016 Sep 6;24(9):1476-87. doi: 10.1016/j.str.2016.06.018.

42) Arnez JG, Moras D. Structural and functional considerations of the aminoacylation reaction. Trends Biochem Sci. 1997 Jun;22(6):211-6. doi: 10.1016/s0968-0004(97)01052-9.

43) Koh CY, Wetzel AB, de van der Schueren WJ, Hol WG. Comparison of histidine recognition in human and trypanosomatid histidyl-tRNA synthetases. Biochimie. 2014 Nov;106:111-20. doi: 10.1016/j.biochi.2014.08.005.

44) Nasim F, Qureshi IA. Aminoacyl tRNA Synthetases: Implications of structural Biology in drug development against trypanosomatid parasites. ACS Omega. 2023 Apr 10;8(17):14884-14899. doi: 10.1021/acsomega.3c00826.

45) Merritt EA, Arakaki TL, Gillespie JR, Larson ET, Kelley A, Mueller N, Napuli AJ, Kim J, Zhang L, Verlinde CL, Fan E, Zucker F, Buckner FS, van Voorhis WC, Hol WG. Crystal structures of trypanosomal histidyl-tRNA synthetase illuminate differences between eukaryotic and prokaryotic homologs. J Mol Biol. 2010 Mar 26;397(2):481-94. doi: 10.1016/j.jmb.2010.01.051.

46) Aberg A, Yaremchuk A, Tukalo M, Rasmussen B, Cusack S. Crystal structure analysis of the activation of histidine by *Thermus thermophilus* histidyl-tRNA synthetase. Biochemistry. 1997 Mar 18;36(11):3084-94. doi: 10.1021/bi9618373.

47) Koh CY, Siddaramaiah LK, Ranade RM, Nguyen J, Jian T, Zhang Z, Gillespie JR, Buckner FS, Verlinde CL, Fan E, Hol WG. A binding hotspot in *Trypanosoma cruzi* histidyl-tRNA synthetase revealed by fragment-based crystallographic cocktail screens. Acta Crystallogr D Biol Crystallogr. 2015 Aug;71(Pt 8):1684-98. doi: 10.1107/S1399004715007683.

48) Edgar RC. MUSCLE: multiple sequence alignment with high accuracy and high throughput. Nucleic Acids Res. 2004 Mar 19;32(5):1792-7. doi: 10.1093/nar/gkh340.

49) Kumar S, Stecher G, Li M, Knyaz C, Tamura K. MEGA X: Molecular Evolutionary genetics analysis across computing platforms. Mol Biol Evol. 2018 Jun 1;35(6):1547-1549. doi: 10.1093/molbev/msy096.

50) Saitou N, Nei M. The neighbor-joining method: a new method for reconstructing phylogenetic trees. Mol Biol Evol. 1987 Jul;4(4):406-25. doi: 10.1093/oxfordjournals.molbev.a040454.

51) Narsimulu B, Qureshi R, Jakkula P, Singh P, Arifuddin M, Qureshi IA. Exploration of seryl tRNA synthetase to identify potent inhibitors against leishmanial parasites. Int J Biol Macromol. 2023 May 15;237:124118. doi: 10.1016/j.ijbiomac.2023.124118.

52) Qureshi R, Jakkula P, Sagurthi SR, Qureshi IA. Protein phosphatase 1 of *Leishmania donovani* exhibits conserved catalytic residues and pro-inflammatory response. Biochem Biophys Res Commun. 2019 Aug 27;516(3):770-776. doi: 10.1016/j.bbrc.2019.06.085.

53) Mendelsohn LD. ChemDraw 8 ultra, windows and macintosh versions. J. Chem. Inf. Comput. Sci. 2004 Sep 28; 44(6):2225-2226. doi: 10.1021/ci040123t

54) Trott O, Olson AJ. AutoDock Vina: improving the speed and accuracy of docking with a new scoring function, efficient optimization, and multithreading. J Comput Chem. 2010 Jan 30;31(2):455-61. doi: 10.1002/jcc.21334.

55) Laskowski RA, Swindells MB. LigPlot+: multiple ligand-protein interaction diagrams for drug discovery. J Chem Inf Model. 2011 Oct 24;51(10):2778-86. doi: 10.1021/ci200227u.

56) Van Der Spoel D, Lindahl E, Hess B, Groenhof G, Mark AE, Berendsen HJ. GROMACS: fast, flexible, and free. J Comput Chem. 2005 Dec;26(16):1701-18. doi: 10.1002/jcc.20291.

57) Berendsen HJC, Grigera JR, Tjerk PS. The missing term in effective pair potentials. J. Phys. Chem. C. 1987 91.24:6269-6271. doi: 10.1021/j100308a038

58) Narsimulu B, Qureshi R, Jakkula P, Are S, Qureshi IA. Biophysical and structural characterization of ribulose-5-phosphate epimerase from *Leishmania donovani*. ACS Omega. 2021 Dec 17;7(1):548-564. doi: 10.1021/acsomega.1c04967.

59) Delarue M, Poterszman A, Nikonov S, Garber M, Moras D, Thierry JC. Crystal structure of a prokaryotic aspartyl tRNA-synthetase. EMBO J. 1994 Jul 15;13(14):3219-29. doi: 10.1002/j.1460-2075.1994.tb06623.x.

60) Wolf YI, Aravind L, Grishin NV, Koonin EV. Evolution of aminoacyl-tRNA synthetases--analysis of unique domain architectures and phylogenetic trees reveals a complex history of horizontal gene transfer events. Genome Res. 1999 Aug;9(8):689-710. doi: 10.1101/gr.9.8.689

61) Frugier M, Moulinier L, Giegé R. A domain in the N-terminal extension of class IIb eukaryotic aminoacyl-tRNA synthetases is important for tRNA binding. EMBO J. 2000 May 15;19(10):2371-80. doi: 10.1093/emboj/19.10.2371.

62) Delagoutte B, Moras D, Cavarelli J. tRNA aminoacylation by arginyl-tRNA synthetase: induced conformations during substrates binding. EMBO J. 2000 Nov 1;19(21):5599-610. doi: 10.1093/emboj/19.21.5599.

63) Guth EC, Francklyn CS. Kinetic discrimination of tRNA identity by the conserved motif 2 loop of a class II aminoacyl-tRNA synthetase. Mol Cell. 2007 Feb 23;25(4):531-42. doi: 10.1016/j.molcel.2007.01.015.

64) Igloi GL. Gene organization and phylum-specific attributes of eukaryotic arginyl-tRNA synthetases. Gene Rep. Epub 2020 Jul 13;20:100778. doi: 0.1016/j.genrep.2020.100778

65) Schimmel P. Aminoacyl tRNA synthetases: general scheme of structure-function relationships in the polypeptides and recognition of transfer RNAs. Annu Rev Biochem. 1987;56:125-58. doi: 10.1146/annurev.bi.56.070187.001013.

66) Geslain R, Ribas de Pouplana L. Regulation of RNA function by aminoacylation and editing? Trends Genet. 2004 Dec;20(12):604-10. doi: 10.1016/j.tig.2004.09.012.

67) Havrylenko S, Legouis R, Negrutskii B, Mirande M. Methionyl-tRNA synthetase from Caenorhabditis elegans: a specific multidomain organization for convergent functional evolution. Protein Sci. 2010 Dec;19(12):2475-84. doi: 10.1002/pro.529.

68) Kaminska M, Shalak V, Mirande M. The appended C-domain of human methionyl-tRNA synthetase has a tRNA-sequestering function. Biochemistry. 2001 Nov 27;40(47):14309-16. doi: 10.1021/bi015670b.

69) Krovat BC, Jantsch MF. Comparative mutational analysis of the double-stranded RNA binding domains of *Xenopus laevis* RNA-binding protein A. J Biol Chem. 1996 Nov 8;271(45):28112-9. doi: 10.1074/jbc.271.45.28112.

70) Kim HS, Cha SY, Jo CH, Han A, Hwang KY. The crystal structure of arginyl-tRNA synthetase from *Homo sapiens*. FEBS Lett. 2014 Jun 27;588(14):2328-34. doi: 10.1016/j.febslet.2014.05.027.

71) Larson ET, Kim JE, Castaneda LJ, Napuli AJ, Zhang Z, Fan E, Zucker FH, Verlinde CL, Buckner FS, Van Voorhis WC, Hol WG, Merritt EA. The double-length tyrosyl-tRNA synthetase from the eukaryote *Leishmania major* forms an intrinsically asymmetric pseudo-dimer. J Mol Biol. 2011 Jun 3;409(2):159-76. doi: 10.1016/j.jmb.2011.03.026.

72) Parrot C, Moulinier L, Bernard F, Hashem Y, Dupuy D, Sissler M. Peculiarities of aminoacyl-tRNA synthetases from trypanosomatids. J Biol Chem. 2021 Aug;297(2):100913. doi: 10.1016/j.jbc.2021.100913.

73) Guth E, Connolly SH, Bovee M, Francklyn CS. A substrate-assisted concerted mechanism for aminoacylation by a class II aminoacyl-tRNA synthetase. Biochemistry. 2005 Mar 15;44(10):3785-94. doi: 10.1021/bi047923h.

74) Guth E, Farris M, Bovee M, Francklyn CS. Asymmetric amino acid activation by class II histidyl-tRNA synthetase from *Escherichia coli*. J Biol Chem. 2009 Jul 31;284(31):20753-62. doi: 10.1074/jbc.M109.021311.

75) Blocquel D, Sun L, Matuszek Z, Li S, Weber T, Kuhle B, Kooi G, Wei N, Baets J, Pan T, Schimmel P, Yang XL. CMT disease severity correlates with mutation-induced open conformation of histidyl-tRNA synthetase, not aminoacylation loss, in patient cells. Proc Natl Acad Sci U S A. 2019 Sep 24;116(39):19440-19448. doi: 10.1073/pnas.1908288116.

76) Moen SO, Edwards TE, Dranow DM, Clifton MC, Sankaran B, Van Voorhis WC, Sharma A, Manoil C, Staker BL, Myler PJ, Lorimer DD. Ligand co-crystallization of aminoacyl-tRNA synthetases from infectious disease organisms. Sci Rep. 2017 Mar 16;7(1):223. doi: 10.1038/s41598-017-00367-6.

77) Arnez JG, Augustine JG, Moras D, Francklyn CS. The first step of aminoacylation at the atomic level in histidyl-tRNA synthetase. Proc Natl Acad Sci U S A. 1997 Jul 8;94(14):7144-9. doi: 10.1073/pnas.94.14.7144.

78) Are S, Gatreddi S, Jakkula P, Qureshi IA. Structural attributes and substrate specificity of pyridoxal kinase from *Leishmania donovani.* Int J Biol Macromol. 2020 Jun 1;152:812-827. doi: 10.1016/j.ijbiomac.2020.02.257.

79) Narsimulu B, Jakkula P, Qureshi R, Nasim F, Qureshi IA. Inhibition and structural insights of leishmanial glutamyl-tRNA synthetase for designing potent therapeutics. Int J Biol Macromol. 2024 Jan;254(Pt 2):127756. doi: 10.1016/j.ijbiomac.2023.127756.

80) Parfait R, Grosjean H. Arginyl-transfer ribonucleic-acid synthetase from *Bacillus stearothermophilus*. Purification, properties and mechanism of action. Eur J Biochem. 1972 Oct;30(2):242-9. doi: 10.1111/j.1432-1033.1972.tb02092.x.

81) Nazario M, Evans JA. Physical and kinetic studies of arginyl transfer ribonucleic acid ligase of *Neurospora*. A sequential ordered mechanism. J Biol Chem. 1974 Aug 10;249(15):4934-6. doi: 10.1016/S0021-9258(19)42411-3

82) Baragaña B, Forte B, Choi R, Nakazawa Hewitt S, Bueren-Calabuig JA, Pisco JP, Peet C, Dranow DM, Robinson DA, Jansen C, Norcross NR, Vinayak S, Anderson M, Brooks CF, Cooper CA, Damerow S, Delves M, Dowers K, Duffy J, Edwards TE, Hallyburton I, Horst BG, Hulverson MA, Ferguson L, Jiménez-Díaz MB, Jumani RS, Lorimer DD, Love MS, Maher S, Matthews H, McNamara CW, Miller P, O'Neill S, Ojo KK, Osuna-Cabello M, Pinto E, Post J, Riley J, Rottmann M, Sanz LM, Scullion P, Sharma A, Shepherd SM, Shishikura Y, Simeons FRC, Stebbins EE, Stojanovski L, Straschil U, Tamaki FK, Tamjar J, Torrie LS, Vantaux A, Witkowski B, Wittlin S, Yogavel M, Zuccotto F, Angulo-Barturen I, Sinden R, Baum J, Gamo FJ, Mäser P, Kyle DE, Winzeler EA, Myler PJ, Wyatt PG, Floyd D, Matthews D, Sharma A, Striepen B, Huston CD, Gray DW, Fairlamb AH, Pisliakov AV, Walpole C, Read KD, Van Voorhis WC, Gilbert IH. Lysyl-tRNA synthetase as a drug target in malaria and cryptosporidiosis. Proc Natl Acad Sci U S A. 2019 Apr 2;116(14):7015-7020. doi: 10.1073/pnas.1814685116.

83) Bhat SY, Jagruthi P, Srinivas A, Arifuddin M, Qureshi IA. Synthesis and characterization of quinoline-carbaldehyde derivatives as novel inhibitors for leishmanial methionine

aminopeptidase 1. Eur J Med Chem. 2020 Jan 15;186:111860. doi: 10.1016/j.ejmech.2019.111860.

84) Bhat SY, Bhandari S, Thacker PS, Arifuddin M, Qureshi IA. Development of quinoline-based hybrid as inhibitor of methionine aminopeptidase 1 from *Leishmania donovani*. Chem Biol Drug Des. 2021 Feb;97(2):315-324. doi: 10.1111/cbdd.13783.

85) Goldberger RF, Kovach JS. Regulation of histidine biosynthesis in *Salmonella typhimurium*. Curr Top Cell Regul. 1972;5:285-308. doi: 10.1016/b978-0-12-152805-8.50014-9.

86) Chen CC, Somberg EW. Purification and characterization of histidyl-transfer RNA synthetase from *Neurospora crassa*. Biochim Biophys Acta. 1980 Jun 13;613(2):514-25. doi: 10.1016/0005-2744(80)90107-2.

87) Di Natale P, Cimino F, De Lorenzo F. The pyrophosphate exchange reaction of histidyl-tRNA synthetase from *Salmonella typhimurium*: reaction parameters and inhibition by transfer ribonucleic acid. FEBS Lett. 1974 Sep 15;46(1):175-9. doi: 10.1016/0014-5793(74)80362-5.

88) De Lorenzo F, Ames BN. Histidine regulation in *Salmonella typhimurium*. VII. Purification and general properties of the histidyl transfer ribonucleic acid synthetase. J Biol Chem. 1970 Apr 10;245(7):1710-6. doi: 10.1016/S0021-9258(19)77150-6

89) Freist W, Verhey JF, Rühlmann A, Gauss DH, Arnez JG. Histidyl-tRNA synthetase. Biol Chem. 1999 Jun;380(6):623-46. doi: 10.1515/BC.1999.079.

90) Ador L, Jaeger S, Geslain R, Martin F, Cavarelli J, Eriani G. Mutation and evolution of the magnesium-binding site of a class II aminoacyl-tRNA synthetase. Biochemistry. 2004 Jun 8;43(22):7028-37. doi: 10.1021/bi049617+.

91) Kane SM, Vugrincic C, Finbloom DS, Smith DW. Purification and some properties of the histidyl-tRNA synthetase from the cytosol of rabbit reticulocytes. Biochemistry. 1978 Apr 18;17(8):1509-14. doi: 10.1021/bi00601a024.

92) Kalousek F, Konigsberg WH. Purification and characterization of histidyl transfer ribonucleic acid synthetase of *Escherichia coli*. Biochemistry. 1974 Feb 26;13(5):999-1006. doi: 10.1021/bi00702a026.

93) Boguslawski G, Vodkin MH, Finkelstein DB, Fink GR. Histidyl-tRNAs and histidyl-tRNA synthetases in wild type and cytoplasmic petite mutants of *Saccharomyces cerevisiae*. Biochemistry. 1974 Oct 22;13(22):4659-67. doi: 10.1021/bi00719a030.

94) Cavarelli J, Eriani G, Rees B, Ruff M, Boeglin M, Mitschler A, Martin F, Gangloff J, Thierry JC, Moras D. The active site of yeast aspartyl-tRNA synthetase: structural and functional aspects of the aminoacylation reaction. EMBO J. 1994 Jan 15;13(2):327-37. doi: 10.1002/j.1460-2075.1994.tb06265.x.

95) Nasim F, Kumar MS, Alvala M, Qureshi IA. Unraveling the peculiarities and development of novel inhibitors of leishmanial arginyl-tRNA synthetase. FEBS J. 2024 Mar 25. doi: 10.1111/febs.17122.

96) Khan S, Sharma A, Belrhali H, Yogavel M, Sharma A. Structural basis of malaria parasite lysyl-tRNA synthetase inhibition by cladosporin. J Struct Funct Genomics. 2014 Jun;15(2):63-71. doi: 10.1007/s10969-014-9182-1.

97) Fang P, Han H, Wang J, Chen K, Chen X, Guo M. Structural Basis for Specific Inhibition of tRNA Synthetase by an ATP Competitive Inhibitor. Chem Biol. 2015 Jun 18;22(6):734-44. doi: 10.1016/j.chembiol.2015.05.007.

98) Bhat SY, Qureshi IA. Mutations of key substrate binding residues of leishmanial peptidase T alter its functional and structural dynamics. Biochim Biophys Acta Gen Subj. 2020 Jan;1864(1):129465. doi: 10.1016/j.bbagen.2019.129465.

99) Shimada A, Nureki O, Goto M, Takahashi S, Yokoyama S. Structural and mutational studies of the recognition of the arginine tRNA-specific major identity element, A20, by arginyl-tRNA synthetase. Proc Natl Acad Sci U S A. 2001 Nov 20;98(24):13537-42. doi: 10.1073/pnas.231267998.

100) Chroni A, Pyrpassopoulos S, Thanassoulas A, Nounesis G, Zannis VI, Stratikos E. Biophysical analysis of progressive C-terminal truncations of human apolipoprotein E4: insights into secondary structure and unfolding properties. Biochemistry. 2008 Sep 2;47(35):9071-80. doi: 10.1021/bi800469r.

101) Pan KM, Baldwin M, Nguyen J, Gasset M, Serban A, Groth D, Mehlhorn I, Huang Z, Fletterick RJ, Cohen FE, et al. Conversion of alpha-helices into beta-sheets features in the formation of the scrapie prion proteins. Proc Natl Acad Sci U S A. 1993 Dec 1;90(23):10962-6. doi: 10.1073/pnas.90.23.10962.

102) Litvinov RI, Faizullin DA, Zuev YF, Weisel JW. The α-helix to β-sheet transition in stretched and compressed hydrated fibrin clots. Biophys J. 2012 Sep 5;103(5):1020-7. doi: 10.1016/j.bpj.2012.07.046.

103) Abidi M, Iram A, Furkan M, Naeem A. Secondary structural alterations in glucoamylase as an influence of protein aggregation. Int J Biol Macromol. 2017 May;98:459-468. doi: 10.1016/j.ijbiomac.2017.01.086.

104) Szczesny-Malysiak E, Dybas J, Blat A, Bulat K, Kus K, Kaczmarska M, Wajda A, Malek K, Chlopicki S, Marzec KM. Irreversible alterations in the hemoglobin structure affect oxygen binding in human packed red blood cells. Biochim Biophys Acta Mol Cell Res. 2020 Nov;1867(11):118803. doi: 10.1016/j.bbamcr.2020.118803.

105) Vijayakumar S, Vishveshwara S, Ravishanker G, Beveridge DL. Differential stability of beta-sheets and alpha-helices in beta-lactamase: a high temperature molecular dynamics study of unfolding intermediates. Biophys J. 1993 Dec;65(6):2304-12. doi: 10.1016/S0006-3495(93)81288-8.

106) Qin Z, Buehler MJ. Molecular dynamics simulation of the α-helix to β-sheet transition in coiled protein filaments: evidence for a critical filament length scale. Phys Rev Lett. 2010 May 14;104(19):198304. doi: 10.1103/PhysRevLett.104.198304.

107) Smirnova E, Safenkova I, Stein-Margolina B, Shubin V, Gurvits B. L-arginine induces protein aggregation and transformation of supramolecular structures of the aggregates. Amino Acids. 2013 Oct;45(4):845-55. doi: 10.1007/s00726-013-1528-7.

108) Goldman-Pinkovich A, Kannan S, Nitzan-Koren R, Puri M, Pawar H, Bar-Avraham Y, McDonald J, Sur A, Zhang WW, Matlashewski G, Madhubala R, Michaeli S, Myler PJ, Zilberstein D. Sensing Host Arginine Is Essential for *Leishmania* Parasites' Intracellular Development. mBio. 2020 Oct 13;11(5):e02023-20. doi: 10.1128/mBio.02023-20.

109) Cavarelli J, Delagoutte B, Eriani G, Gangloff J, Moras D. L-arginine recognition by yeast arginyl-tRNA synthetase. EMBO J. 1998 Sep 15;17(18):5438-48. doi: 10.1093/emboj/17.18.5438.

110) Schulman LH, Pelka H. The anticodon contains a major element of the identity of arginine transfer RNAs. Science. 1989 Dec 22;246(4937):1595-7. doi: 10.1126/science.2688091.

111) Geslain R, Bey G, Cavarelli J, Eriani G. Limited set of amino acid residues in a class Ia aminoacyl-tRNA synthetase is crucial for tRNA binding. Biochemistry. 2003 Dec 30;42(51):15092-101. doi: 10.1021/bi035581u.

112) Konno M, Sumida T, Uchikawa E, Mori Y, Yanagisawa T, Sekine S, Yokoyama S. Modeling of tRNA-assisted mechanism of Arg activation based on a structure of Arg-tRNA synthetase, tRNA, and an ATP analog (ANP). FEBS J. 2009 Sep;276(17):4763-79. doi: 10.1111/j.1742-4658.2009.07178.x.

113) Auffinger P, Hays FA, Westhof E, Ho PS. Halogen bonds in biological molecules. Proc Natl Acad Sci U S A. 2004 Nov 30;101(48):16789-94. doi: 10.1073/pnas.0407607101.

114) Jain V, Yogavel M, Kikuchi H, Oshima Y, Hariguchi N, Matsumoto M, Goel P, Touquet B, Jumani RS, Tacchini-Cottier F, Harlos K, Huston CD, Hakimi MA, Sharma A. Targeting Prolyl-tRNA Synthetase to Accelerate Drug Discovery against Malaria, Leishmaniasis, Toxoplasmosis, Cryptosporidiosis, and Coccidiosis. Structure. 2017 Oct 3;25(10):1495-1505.e6. doi: 10.1016/j.str.2017.07.015.

115) Ahmad B, Ahmed MZ, Haq SK, Khan RH. Guanidine hydrochloride denaturation of human serum albumin originates by local unfolding of some stable loops in domain III. Biochim Biophys Acta. 2005 Jun 15;1750(1):93-102. doi: 10.1016/j.bbapap.2005.04.001.

116) Scopes DA, Bautista JM, Naylor CE, Adams MJ, Mason PJ. Amino acid substitutions at the dimer interface of human glucose-6-phosphate dehydrogenase that increase thermostability and reduce the stabilising effect of NADP. Eur J Biochem. 1998 Jan 15;251(1-2):382-8. doi: 10.1046/j.1432-1327.1998.2510382.x.

117) Chan CH, Yu TH, Wong KB. Stabilizing salt-bridge enhances protein thermostability by reducing the heat capacity change of unfolding. PLoS One. 2011;6(6):e21624. doi: 10.1371/journal.pone.0021624.

118) Sharma R, Sastry GN. Deciphering the Dynamics of Non-Covalent Interactions Affecting Thermal Stability of a Protein: Molecular Dynamics Study on Point Mutant of *Thermus thermophilus* Isopropylmalate Dehydrogenase. PLoS One. 2015 Dec 11;10(12):e0144294. doi: 10.1371/journal.pone.0144294.

119) Milla ME, Brown BM, Sauer RT. Protein stability effects of a complete set of alanine substitutions in Arc repressor. Nat Struct Biol. 1994 Aug;1(8):518-23. doi: 10.1038/nsb0894-518.

120) Cahuzac B, Berthonneau E, Birlirakis N, Guittet E, Mirande M. A recurrent RNA-binding domain is appended to eukaryotic aminoacyl-tRNA synthetases. EMBO J. 2000 Feb 1;19(3):445-52. doi: 10.1093/emboj/19.3.445.

121) Shiba K. Intron positions delineate the evolutionary path of a pervasively appended peptide in five human aminoacyl-tRNA synthetases. J Mol Evol. 2002 Dec;55(6):727-33. doi: 10.1007/s00239-002-2368-3.

122) Raben N, Nichols R, Dohlman J, McPhie P, Sridhar V, Hyde C, Leff R, Plotz P. A motif in human histidyl-tRNA synthetase which is shared among several aminoacyl-tRNA synthetases is a coiled-coil that is essential for enzymatic activity and contains the major autoantigenic epitope. J Biol Chem. 1994 Sep 30;269(39):24277-83. doi: 10.1016/S0021-9258(19)51078-X

123) Nakama T, Nureki O, Yokoyama S. Structural basis for the recognition of isoleucyl-adenylate and an antibiotic, mupirocin, by isoleucyl-tRNA synthetase. J Biol Chem. 2001 Dec 14;276(50):47387-93. doi: 10.1074/jbc.M109089200.

124) Hoepfner D, McNamara CW, Lim CS, Studer C, Riedl R, Aust T, McCormack SL, Plouffe DM, Meister S, Schuierer S, Plikat U, Hartmann N, Staedtler F, Cotesta S, Schmitt EK, Petersen F, Supek F, Glynne RJ, Tallarico JA, Porter JA, Fishman MC, Bodenreider C, Diagana TT, Movva NR, Winzeler EA. Selective and specific inhibition of the *Plasmodium falciparum* lysyl-tRNA synthetase by the fungal secondary metabolite cladosporin. Cell Host Microbe. 2012 Jun 14;11(6):654-63. doi: 10.1016/j.chom.2012.04.015.

8. Publications

The FEBS Journal

FEBS PRESS science publishing by scientists

Unraveling the peculiarities and development of novel inhibitors of leishmanial arginyl-tRNA synthetase

Fouzia Nasim[1], Muppidi Shravan Kumar[2], Mallika Alvala[2] and Insaf Ahmed Qureshi[1]

1 Department of Biotechnology & Bioinformatics, School of Life Sciences, University of Hyderabad, Hyderabad, India
2 Department of Medicinal Chemistry, National Institute of Pharmaceutical Education and Research, Hyderabad, India

Keywords
arginyl-tRNA synthetase; benzothiazolo-coumarin derivatives; novel insertion; potent inhibitors; tRNA-binding domain

Correspondence
I. A. Qureshi, Department of Biotechnology & Bioinformatics, School of Life Sciences, University of Hyderabad, Hyderabad 500046, India
Tel: +91 40 23134588
E-mail: insaf@uohyd.ac.in

(Received 17 December 2023, revised 22 February 2024, accepted 11 March 2024)

doi:10.1111/febs.17122

Aminoacylation by tRNA synthetase is a crucial part of protein synthesis and is widely recognized as a therapeutic target for drug development. Unlike the arginyl-tRNA synthetases (ArgRSs) reported previously, here, we report an ArgRS of *Leishmania donovani* (*Ld*ArgRS) that can follow the canonical two-step aminoacylation process. Since a previously uncharacterized insertion region is present within its catalytic domain, we implemented the splicing by overlap extension PCR (SOE–PCR) method to create a deletion mutant (ΔIns-*Ld*ArgRS) devoid of this region to investigate its function. Notably, the purified *Ld*ArgRS and ΔIns-*Ld*ArgRS exhibited different oligomeric states along with variations in their enzymatic activity. The full-length protein showed better catalytic efficiency than ΔIns-*Ld*ArgRS, and the insertion region was identified as the tRNA binding domain. In addition, a benzothiazolo-coumarin derivative (Comp-7j) possessing high pharmacokinetic properties was recognized as a competitive and more specific inhibitor of *Ld*ArgRS than its human counterpart. Removal of the insertion region altered the mode of inhibition for ΔIns--*Ld*ArgRS and caused a reduction in the inhibitor's binding affinity. Both purified proteins depicted variances in the secondary structural content upon ligand binding and thus, thermostability. Apart from the trypanosomatid-specific insertion and Rossmann fold motif, *Ld*ArgRS revealed typical structural characteristics of ArgRSs, and Comp-7j was found to bind within the ATP binding pocket. Furthermore, the placement of $tRNA^{Arg}$ near the insertion region enhanced the stability and compactness of *Ld*ArgRS compared to other ligands. This study thus reports a unique ArgRS with respect to catalytic as well as structural properties, which can be considered a plausible drug target for the derivation of novel anti-leishmanial agents.

Abbreviations
aa, amino acids; aaRSs, aminoacyl-tRNA synthetases; ADME, absorption, distribution, metabolism, and excretion; ANS, 8-anilinonapthalene-1-sulfonic acid; ArgRS, arginyl-tRNA synthetase; ATP, adenosine triphosphate; CCD, catalytic core domain; DMEM, Dulbecco's modified eagle medium; DMSO, dimethyl sulfoxide; DTT, dithiothreitol; EDTA, ethylenediaminetetraacetic acid; EMSA, electrophoretic mobility shift assay; FBS, fetal bovine serum; GAD, GatB-AaRs-for-Asp domain; GatB, B-subunit of archaeal Glu-tRNAGln amidotransferases; GdHCl, guanidine hydrochloride; HIGH, histidine-isoleucine-glycine-histidine; IPTG, isopropyl β-D-1-thiogalactopyranoside; KMSKS, lysine-methionine-serine-lysine-serine; L-Arg, L-arginine; L-Can, L-canavanine; MST, microscale thermophoresis; MTT, 3-(4,5-dimethyl-2-thiazolyl)-2,5-diphenyltetrazolium bromide; ORF, open reading frame; PCR, polymerase chain reaction; PMSF, phenylmethylsulfonyl fluoride; PPi, inorganic phosphate; Rg, radius of gyration; RMSD, root mean square deviation; RMSF, root mean square fluctuation; SDS–PAGE, sodium dodecyl sulfate-polyacrylamide gel electrophoresis; SOE–PCR, splicing by overlap extension PCR; TBE, tris-borate-acetic acid; WHO, World Health Organization; ytRNA, yeast total tRNA.

ACS OMEGA

http://pubs.acs.org/journal/acsodf

Review

Aminoacyl tRNA Synthetases: Implications of Structural Biology in Drug Development against Trypanosomatid Parasites

Fouzia Nasim and Insaf Ahmed Qureshi*

Cite This: *ACS Omega* 2023, 8, 14884−14899

Read Online

ABSTRACT: The ensemble of aminoacyl tRNA synthetases is regarded as a key component of the protein translation machinery. With the progressive increase in structure-based studies on tRNA synthetase-ligand complexes, the detailed picture of these enzymes is becoming clear. Having known their critical role in deciphering the genetic code in a living system, they have always been chosen as one of the important targets for development of antimicrobial drugs. Later on, the role of aminoacyl tRNA synthetases (aaRSs) on the survivability of trypanosomatids has also been validated. It became evident through several gene knockout studies that targeting even one of these enzymes affected parasitic growth drastically. Such successful studies have inspired researchers to search for inhibitors that could specifically target trypanosomal aaRSs, and their never-ending efforts have provided fruitful results. Taking all such studies into consideration, these macromolecules of prime importance deserve further investigation for the development of drugs that cure spectrum of infections caused by trypanosomatids. In this review, we have compiled advancements of over a decade that have taken place in the pursuit of devising drugs by using trypanosomatid aaRSs as a major target of interest. Several of these inhibitors work on an exemplary low concentration range without posing any threat to the mammalian cells which is a very critical aspect of the drug discovery process. Advancements have been made in terms of using structural biology as an important tool to analyze the architecture of the trypanosomatids aaRSs and concoction of inhibitors with augmented specificities toward their targets. Some of the inhibitors that have been tested on other parasites successfully but their efficacy has so far not been validated against these trypanosomatids have also been appended.

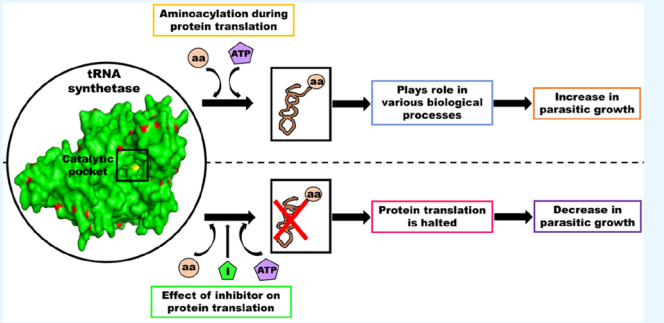

1. INTRODUCTION

The order Trypanosomatida comprises singly flagellated intracellular parasites that are classified under the phylum Euglenozona and class Kinetoplastea. The corkscrew-like motion present in some of its members forms the basis of its nomenclature (trypano: borer, soma: body), and they can either have a monoxenous or dixenous lifecycle. In the monoxenous mode, only one host is needed to complete their lifecycle, while in the dixenous mode, two hosts are involved. Although most of the trypanosomatids are known to follow monoxenous lifestyle by infecting insects, e.g., *Leptomonas* sp., the dixenous forms have also been reported. For instance, *Phytomonas* sp. get transmitted from phytophagous insects to plants,[1] and *Leishmania* sp. spread by hematophagous insects such as sand flies to vertebrates.[2] When it comes to humans, there are three majorly known diseases caused by trypanosomatids, viz. leishmaniasis, known to be caused by *Leishmania* sp., African trypanosomiasis, caused by *Trypanosoma brucei gambiense* and *Trypanosoma brucei rhodesiense*, and American trypanosomiasis which is caused by *Trypanosoma cruzi*. Each of these parasites is transmitted by distinct insect vectors. The female sandflies of the genus *Lutzomyia* and *Phlebotomus* of subfamily Phlebotominae are primary hosts of *Leishmania* sp., the tsetse flies are carriers of *Trypanosoma brucei*, and *Trypanosoma cruzi* is transmitted by triatomine bugs. Thus, these parasites can attack healthy hosts in diverse ways. In leishmaniasis, the infective stage (promastigotes) of *Leishmania* sp. is injected into the secondary hosts by sandflies which are phagocytosed by macrophages and other mononuclear phagocytic cells. Later on, these promastigotes transform into amastigotes and spread infection to other mononuclear cells. On the other hand, metacyclic trypomastigotes causing African trypanosomiasis are injected into skin tissue of its mammalian host by tsetse flies. The parasites at first enter the lymphatic system and then pass into the bloodstream where they get converted to bloodstream trypomastigotes which can be further carried to other sites of the body. Then upon breaching the blood brain barrier, they enter the central nervous system.[3]

Received: February 8, 2023
Accepted: March 29, 2023
Published: April 10, 2023

Chapter 22

Role of structural biology methods in drug discovery

Fouzia Nasim and Insaf Ahmed Qureshi

Department of Biotechnology and Bioinformatics, School of Life Sciences, University of Hyderabad, Hyderabad, Telangana, India

1 Introduction

Drug discovery involves the identification of novel candidates as probable medication against a specific disease and validation of their potency before proceeding for clinical trials. From being discovered serendipitously to designing inhibitors strategically against their corresponding targets, the discovery of drugs has traversed a long way. Designing drugs by understanding the architecture of their respective targets has become possible due to the application of various structural biology methods. Since it is the branch of science that deals with the three-dimensional (3D) structure acquired by macromolecules in a particular environment, the change of conformations in different conditions can provide information about their tentative functions, which is subsequently used in the lead optimization process. Some of the early structure-based drugs were successfully developed in the late 1970s, following which there has been no turning back, and our expertise to implement structural biology methods in drug discovery and development has improved significantly. For instance, hemoglobin structure-mediated synthesis of ligands was executed to tackle sickle cell anemia.[1] As of November 2020, there are 20,000 prescription drugs approved by the Food and Drug Administration (FDA) and available in the market. Some of them are categorized under the caption of "New Molecular Entities or NMEs" that usually contain active moieties previously not approved by the FDA, although they might be closely related to those already approved. In the journey of identification of such novel moieties, this field of science has been playing a pivotal role for decades and has become the backbone of drug discovery. A report exclusively presents a list of more than 40 drugs designed based on structure-guided methods and have entered the clinical trials.[2] In the current era of science and technology, sophisticated methods, such as highly specialized cryogenic electron microscopy (cryo-EM), high-throughput crystallization screens and robots, powerful synchrotron beamlines, supercomputers, etc., have accelerated the process of protein structure determination by many folds that resulted in scaling up of the new drugs. The use of computer-aided screening of lead compounds and molecular dynamics (MD) simulations have further substantially reduced the time for the development of target-specific drugs that can be investigated through in vitro and in vivo analyses. The macromolecular structures determined by researchers are deposited in the Protein Data Bank (PDB), a repository of atomic coordinates and such other relevant information. Currently, the PDB harbors structures of more than 49,000 human proteins that have been successfully studied to understand their corresponding roles in the etiology of diseases.[3] Time and again, these macromolecular structures have been retrieved to evaluate target druggability, compute affinities of the target-directed inhibitors, augment their specificities, etc. Although the entire process of finding plausible lead compounds till their acceptance in clinical trials is very lengthy and cumbersome, the involvement of structural biology has paved the way to generate effective, potent, and selective drugs, making itself an integral part of this industry (Fig. 1). This chapter discusses the exemplary roles played by structural biology in the drug discovery process.

2 Structural biology aided selection of drug targets

A drug target could be any protein molecule that is either associated with a pathophysiological disorder or is indispensable for a pathogen's survival, such as a receptor, ion channel, enzyme, or a protein fold with an important role in a biological cascade. It could be a protein with either reported physiological and pathological roles or unknown functions. The selection of a drug target is usually preceded by identifying functional domains within the protein of interest using tools that employ multiple sequence alignments and Hidden Markov Models (HMM). Once the functional domains of the protein are defined using such tools, it is necessary to figure out the percentage identity or degree of conservation to that of its human counterpart. As reported previously, a serious failure of drugs in delivering the required efficacy during the clinical trials

Advances in Protein Molecular and Structural Biology Methods. https://doi.org/10.1016/B978-0-323-90264-9.00022-2

Infection, Genetics and Evolution 93 (2021) 104928

Contents lists available at ScienceDirect

Infection, Genetics and Evolution

journal homepage: www.elsevier.com/locate/meegid

Research paper

Comparative genome analysis of *Corynebacterium* species: The underestimated pathogens with high virulence potential

Fouzia Nasim, Arijit Dey, Insaf Ahmed Qureshi *

Department of Biotechnology and Bioinformatics, School of Life Sciences, University of Hyderabad, Hyderabad 500 046, Telangana, India

ARTICLE INFO

Keywords:
Corynebacterium
Diphtheroids
Multidrug resistance
Genome
Virulence
Evolution

ABSTRACT

Non-diphtherial *Corynebacterium* species or diphtheroids were previously considered as the mere contaminants of clinical samples. Of late, they have been reckoned as the formidable infection causing agents of various diseases. While the scientific database is filled with articles that document whole genome analysis of individual isolates, a comprehensive comparative genomic analysis of diphtheroids alongside *Corynebacterium diphtheriae* is expected to enable us in understanding their genomic as well as evolutionary divergence. Here, we have analysed the whole genome sequences of forty strains that were selected from a range of eleven *Corynebacterium* species (pathogenic and non-pathogenic). A statistical analysis of the pan and core genomes revealed that even though the core genome is saturated, the pan genome is yet open rendering scope for newer gene families to be accumulated in the course of evolution that might further change the pathogenic behavior of these species. Every strain had bacteriophage components integrated in its genome and some of them were intact and consisted of toxins. The presence of diversified genomic islands was observed across the dataset and most of them consisted of genes for virulence and multidrug resistance. Moreover, the phylogenetic analysis showed that a diphtheroid is the last common ancestor of all the *Corynebacterium* species. The current study is a compilation of genomic features of pathogenic as well as non-pathogenic *Corynebacterium* species which provides insights into their virulence potential in the times to come.

1. Introduction

The genus *Corynebacterium* represents a group of Gram positive, aerobic as well as anaerobic, non-acid fast pleomorphic bacteria. So far, 130 whole genome sequences of genus *Corynebacterium* have been submitted to the NCBI database. *Corynebacterium* species are ubiquitous in nature, inhabiting from the layers of soil to the skin of mammals. Diphtheroids are distinct from *C. diphtheriae* in terms of both pathogenicity as well as their capacity to get stained uniformly (Chandran et al., 2016) and are the usual residents of human nasopharyngeal microbiota. In the former times, presence of diphtheroids was considered as contamination of clinical samples. Of late, their role has been traced to the aetiology of several infectious diseases in both immunocompetent and immunocompromised hosts. Total 31 species have been associated with pathogenicity in numerous animals and birds like *C. pseudotuberculosis* (caseous lymphadenitis in sheep and goats), *C. amycolatum* (mastitis in cattle), *C. auriscanis* (otitis in dog) etc., whereas species associated with human pathogenicity are *Arcanobacterium haemolyticum* or *Corynebacterium haemolyticum*, *C. jeikeium*, *C. diphtheriae*, *C. ulcerans* etc. Under specific conditions, these coryneform bacteria can cause infections that majorly outbreak in the hospitals and thus are called as nosocomial pathogens (Bernard, 2012). In a survey, it was discovered that of the 762 isolates, 18% were found to cause true infection while 82% were mere contaminants. Most of the clinically significant diphtheroids were isolated from wounds, blood, urine as well as cerebrospinal fluid samples and ophthalmologic cultures (Leal Jr. et al., 2016). Hospital wastes such as catheter tips, sputum, tracheotomy secretions are a good site to isolate *C. pseudotuberculosis, C. renale, C. ulcerans, C. striatum. C. minutissimum* and *C. haemolyticum.* The development of infection could be seen within 48 h if the conditions are favored clinically. The fact that many but not all of the diphtheroids possess multidrug resistant genes is a major cause of concern among researchers and needs to be addressed immediately. Diphtheroid isolates have demonstrated a high degree of resistance towards antibiotics such as ampicillin, ciprofloxacin, gentamicin, erythromycin, penicillin and tetracycline. Although they were highly sensitive to a few antibiotics such as vancomycin, linezolids and chloramphenicol, administration of vancomycin was not suitable due to its reported association with nephrotoxicity in the patients. It is also noteworthy that the

* Corresponding author.
E-mail address: insaf@uohyd.ac.in (I.A. Qureshi).

https://doi.org/10.1016/j.meegid.2021.104928
Received 31 January 2021; Received in revised form 16 May 2021; Accepted 17 May 2021
Available online 20 May 2021

International Journal of Biological Macromolecules 254 (2024) 127756

Contents lists available at ScienceDirect

International Journal of Biological Macromolecules

journal homepage: www.elsevier.com/locate/ijbiomac

Inhibition and structural insights of leishmanial glutamyl-tRNA synthetase for designing potent therapeutics

Bandigi Narsimulu [a,1], Pranay Jakkula [a,1], Rahila Qureshi [b], Fouzia Nasim [a], Insaf Ahmed Qureshi [a,*]

[a] Department of Biotechnology & Bioinformatics, School of Life Sciences, University of Hyderabad, Prof. C.R. Rao Road, Hyderabad 500046, India
[b] Centre for DNA Fingerprinting and Diagnostics, Hyderabad 500039, India

ARTICLE INFO

Keywords:
Leishmaniasis
Glutamyl-tRNA synthetase
Salicylate
Drug discovery

ABSTRACT

Aminoacyl-tRNA synthetases (aaRSs), essential components of the protein synthesizing machinery, have been often chosen for devising therapeutics against parasitic diseases. Due to their relevance in drug development, the current study was designed to explore functional and structural aspects of *Leishmania donovani* glutamyl-tRNA synthetase (*Ld*GluRS). Hence, *Ld*GluRS was cloned into an expression vector and purified to homogeneity using chromatographic techniques. Purified protein showed maximum enzymatic activity at physiological pH, with more binding capacity towards its cofactor (Adenosine triphosphate, 0.06 ± 0.01 mM) than the cognate substrate (L-glutamate, 9.5 ± 0.5 mM). Remarkably, salicylate inhibited *Ld*GluRS competitively with respect to L-glutamate and exhibited druglikeness with negligible effect on human macrophages. The protein possessed more α-helices (43 %) than β-sheets (12 %), whereas reductions in thermal stability and cofactor-binding affinity, along with variation in mode of inhibition after mutation signified the role of histidine (H60) as a catalytic residue. *Ld*GluRS could also generate a pro-inflammatory milieu in human macrophages by upregulating cytokines. The docking study demonstrated the placement of salicylate into *Ld*GluRS substrate-binding site, and the complex was found to be stable during molecular dynamics (MD) simulation. Altogether, our study highlights the understanding of molecular inhibition and structural features of glutamyl-tRNA synthetase from kinetoplastid parasites.

1. Introduction

Leishmaniasis, caused by parasites belonging to the genus *Leishmania*, is a neglected tropical disease that infects millions of people worldwide [1]. Of the several forms, visceral leishmaniasis or kala azar is highly fatal as it affects visceral organs of the body and is also characterized by a wide range of clinical symptoms that include prolonged fever, hypergammaglobulinemia, hepatosplenomegaly, and pancytopenia [2]. Due to the absence of proper vaccines, chemotherapy is the only treatment available for this disease. However, drugs such as pentavalent antimonials, amphotericin B, and miltefosine besides being expensive pose side effects such as toxicity and the need for long-term administration [3]. Also, an increase in the development of resistance by the parasite to available therapeutics necessitates the identification of newer drug targets for treating leishmaniasis.

Aminoacyl-tRNA synthetases are responsible for the ligation of amino acids to their cognate tRNAs that can further take part in protein synthesis. Apart from their role in protein synthesis, aaRSs are also associated with non-canonical functions such as signal transduction, RNA splicing, transcription, angiogenesis, apoptosis *etc*. [4], and are also known for their roles in immune regulation and diseases [5,6]. The twenty aaRSs have been categorized into two classes considering structural dissimilarities in their catalytic cores [7]. The class-I enzymes have a characteristic Rossmann fold, HIGH (His-Ile-Gly-His) and KMSKS (Lys-Met-Ser-Lys-Ser) motifs at their catalytic pocket for ligand binding, whereas the class-II enzymes have antiparallel β-sheets that are

Abbreviations: aaRS, aminoacyl-tRNA synthetase; GluRS, glutamyl-tRNA synthetase; CD, circular dichroism; ORF, open reading frame; ATP, adenosine triphosphate; L-Glu, L-glutamate; tRNA, transfer ribonucleic acid; DTT, dithiothreitol; PPase, inorganic pyrophosphatase; Pi, inorganic phosphate; PPi, inorganic pyrophosphate; KI, potassium iodide; MTT, 3-(4,5-dimethyl-thiazol-2-yl)-2,5-diphenyltetrazolium bromide; PDB, protein data bank.

* Corresponding author at: Department of Biotechnology & Bioinformatics, School of Life Sciences, University of Hyderabad, Hyderabad 500046, India.
E-mail address: insaf@uohyd.ac.in (I.A. Qureshi).

[1] These authors contributed equally to this article.

https://doi.org/10.1016/j.ijbiomac.2023.127756
Received 12 July 2023; Received in revised form 8 October 2023; Accepted 27 October 2023
Available online 29 October 2023

This certificate is awarded to

Ms

Fouzia Nasim

for an **ORAL PRESENTATION** titled

Biochemical and biophysical characterization of leishmanial histidyl tRNA synthetase

THE 6TH INTERNATIONAL CONFERENCE ON

MOLECULAR DIAGNOSTICS & BIOMARKER DISCOVERY

BUILDING RESILIENCE IN BIOMEDICAL RESEARCH

11th – 13th October 2022
On-line (WEBEX Events)

Organised by
Institute for Research in Molecular Medicine (INFORMM)

Co-organised by
Ministry of Higher Education (MoHE) Malaysia

Dr Tye Gee Jun
Conference Chair

Assoc. Prof. Dr Aziah Ismail
Director of INFORMM

12th India-Japan Science and Technology Conclave

INTERNATIONAL CONFERENCE ON FRONTIER AREAS OF SCIENCE AND TECHNOLOGY

(ICFAST-2022)

CERTIFICATE OF PARTICIPATION

This is to certify that Fouzia Nasim from University of Hyderabad. participated/presented in 12th India-Japan Science and Technology Conclave : **International Conference on Frontier Areas of Science and Technology (ICFAST - 2022)** held at University of Hyderabad, Hyderabad 500 046, INDIA during September 09-10, 2022

Head of IPPD JSPS, JAPAN	Chairman ICFAST - 2022	Convener ICFAST - 2022

CHAITANYA BHARATHI
INSTITUTE OF TECHNOLOGY (A)
Kokapet (Village), Gandipet, Hyderabad, Telangana-500075. www.cbit.ac.in

ISO Certified 9001:2015

COMMITTED TO RESEARCH, INNOVATION AND EDUCATION 43 years

SUDHEE 2022

(Ignite Innate Innovations)

23 - 24 March

MERIT CERTIFICATE

This is to certify that Mr. / Ms. Fouzia Nasim of University of Hyderabad has won ~~Best~~ I Paper / ~~Poster~~ / ~~Project-Exhibitor~~ Award for Targeting Leishmania t-RNA Synthatase of Novel therapeutics during **"Sudhee 2022"** on 23 - 24 March 2022 at **Chaitanya Bharathi Institute of Technology (A)**, Hyderabad - 500 075, Telangana, India.

Prof. D. Krishna Reddy
Chairman, Sudhee 2022

Prof. P. Ravinder Reddy
Principal, CBIT (A)

Targeting aminoacyl-tRNA synthetases for the development of novel therapeutics against leishmaniasis

by Fouzia Nasim

Targeting aminoacyl-tRNA synthetases for the development of novel therapeutics against leishmaniasis

ORIGINALITY REPORT

16%	16%	14%	2%
SIMILARITY INDEX	INTERNET SOURCES	PUBLICATIONS	STUDENT PAPERS

PRIMARY SOURCES

1	www.ncbi.nlm.nih.gov Internet Source	12%
2	mafiadoc.com Internet Source	1%
3	Submitted to University of Hyderabad, Hyderabad Student Paper	<1%
4	patents.google.com Internet Source	<1%
5	www2.mdpi.com Internet Source	<1%
6	academic.oup.com Internet Source	<1%
7	digitalassets.lib.berkeley.edu Internet Source	<1%
8	www.frontiersin.org Internet Source	<1%
	journals.plos.org	

9	Internet Source	<1 %
10	rcastoragev2.blob.core.windows.net Internet Source	<1 %
11	www.nature.com Internet Source	<1 %
12	deepblue.lib.umich.edu Internet Source	<1 %
13	www.mdpi.com Internet Source	<1 %
14	www.biotechnologyconsultinggroup.com Internet Source	<1 %
15	www.biorxiv.org Internet Source	<1 %
16	docksci.com Internet Source	<1 %
17	etheses.whiterose.ac.uk Internet Source	<1 %
18	oaktrust.library.tamu.edu Internet Source	<1 %
19	Saha, Piyali, Bipasha Barua, Sanchari Bhattacharyya, M. M. Balamurali, William R. Schief, David Baker, and Raghavan Varadarajan. "Design and Characterization of	<1 %

Stabilized Derivatives of Human CD4D12 and CD4D1", Biochemistry, 2011.
Publication

20	etheses.bham.ac.uk Internet Source	<1 %
21	escholarship.mcgill.ca Internet Source	<1 %
22	hdl.handle.net Internet Source	<1 %
23	opus4.kobv.de Internet Source	<1 %
24	Samayaditya Singh, Insaf Ahmed Qureshi. "Identification of potent inhibitors against chorismate synthase of Toxoplasma gondii using molecular dynamics simulations", Journal of Molecular Graphics and Modelling, 2022 Publication	<1 %
25	Submitted to University of New Haven Student Paper	<1 %
26	epub.uni-regensburg.de Internet Source	<1 %
27	Sourour Addad, Jean-Yves Exposito, Clément Faye, Sylvie Ricard-Blum, Claire Lethias. "Isolation, Characterization and Biological	<1 %

Evaluation of Jellyfish Collagen for Use in Biomedical Applications", Marine Drugs, 2011
Publication

28	d.docksci.com Internet Source	<1 %

Exclude quotes	On	Exclude matches	< 14 words
Exclude bibliography	On		

University of Hyderabad
Hyderabad-500 046, India

PLAGIARISM FREE CERTIFICATE

This is to certify that the similarity index of this thesis as checked by the Library of the University of Hyderabad is 16%. Out of this, 12% similarity has been found to be identified from the candidate's own publication (Fouzia Nasim) available on www.ncbi.nlm.nih.gov. The details of student's publication are as follows:

Publication	Similarity
Nasim F, Qureshi IA. Aminoacyl tRNA synthetases: implications of structural biology in drug development against trypanosomatid parasites. ACS Omega. 2023 Apr 10; 8(17):14884-14899. https://www.ncbi.nlm.nih.gov/pmc/articles/PMC10157851/	12%

About 4% similarity was identified from external sources in the present thesis which is according to prescribed regulations of the University. All the publications related to this thesis have been appended at the end of the thesis. Hence, the present thesis may be considered plagiarism-free.

(Dr. Insaf Ahmed Qureshi)

Dr. INSAF A. QURESHI
Associate Professor
Dept. of Biotechnology & Bioinformatics
School of Life Sciences
University of Hyderabad
Hyderabad-500 046, India.